Investigating the Interplay of Mitochondrial Dynamics and Proteostasis during Neuronal Ischemia/Reperfusion Injury using Integrated Imaging and Modeling Approaches

by

Garrett M. Fogo

A dissertation submitted in partial fulfillment
of the requirements of the degree of
Doctor of Philosophy
(Neuroscience)
in The University of Michigan
2024

Doctoral Committee:

Associate Professor Thomas H. Sanderson, Co-Chair
Professor Audrey Seasholtz, Co-Chair
Professor Anuska V. Andjelkovic
Professor David A. Antonetti
Professor Richard Mortensen

Garrett Fogo

gfogo@umich.edu

ORCID iD: 0000-0001-5292-3702

DEDICATION

To my friends, family, and labmates

ACKNOWLEDGEMENTS

None of this would be possible without my advisor Dr. Thomas Sanderson. I do not know what my graduate training would have looked like without the intellectual and scientific freedom that was granted to me. Thank you for listening to all my crazy ideas and even letting me do some of them. I am grateful for the advice, patience, and friendship.

Thank you to all of my labmates (past and present) and collaborators. All the Sanderson Lab members have been and continue to be fantastic. The beginning of my graduate career was molded by what I learned from Dr. Anthony Anzell, who blazed the trail for much of this work. Thank you to Katlynn Emaus and Francisco Torres Torres for your help and companionship, even despite my difficult nature. Thank you to Sarita Raghunayakula, Erin Gruley, and Gary Shangguan for being the backbone of the Sanderson Lab. Nothing would ever get accomplished without the work you all do behind the scenes. Dr. Joseph Wider has been like a second mentor to me, also listening to my crazy ideas, thank you.

I have had the absolute privilege to work with an amazing thesis committee: Drs. Audrey Seaholtz, Anuska Andjelkovic, David Antonetti, Richard Mortensen. Thank you for trusting me and allowing me to change my project almost every meeting. Your advice, feedback, and support have greatly improved this dissertation and my growth as a scientist.

The Neuroscience Graduate Program is really just one big family. The maternal figures of the family Dr. Carol Elias, Dr. Audrey Seasholtz, Valerie Smith, Rachel Harbach, and Vicky Martin provide a tremendous environment for training and living. I am so proud to be part of the NGP family.

Thank you also to my undergraduate advisor Dr. Andrew Gall at Hope College. Nothing I have accomplished would have been possible without you taking a chance on a shy Freshman student. Your other students and I will never know how lucky we are to work with and learn from you.

Of course, a final thank you to my family. My first mentors were my parents, Matt and Sue. Their unconditional support will never get that the thanks it deserves.

TABLE OF CONTENTS

LIST OF FIGURES

ABSTRACT

Cerebral ischemia/reperfusion (I/R) injuries, including stroke and cardiac arrest can lead to irreversible neuronal damage and neurological complications. Mitochondrial damage and dysfunction are critical components of both ischemia and reperfusion-induced injury. Protecting and restoring mitochondrial function during reperfusion is a promising therapeutic strategy for limiting potentiation of neuronal damage. Mitochondria are highly dynamic organelles that exist in size and shape ranging from small punctate to large sprawling networks. These morphologies are dictated by the mechanisms of mitochondrial dynamics and quality control. Mitochondrial dynamics, consisting of fission and fusion, generate the complex architecture of mitochondrial networks. Recycling of old and damaged mitochondrial components is mediated by the quality control pathways of intramitochondrial proteostasis and mitophagy, the autophagic degradation of mitochondria. These pathways collectively work to remodel the mitochondrial proteome. The processes of mitochondrial dynamics and quality control have been demonstrated to be active in neurons during I/R injury.

The aim of my thesis was to characterize the patterns and interactions of mitochondrial dynamics and proteostasis during the temporal window of acute reperfusion. In a primary neuron model of *in vitro* I/R injury, I imaged mitochondrial fission and fusion patterns, along with changes in mitochondrial proteostasis. Mitochondrial dynamics were analyzed by a novel machine learning-based morphological classification pipeline with single mitochondrion resolution. Proteostasis was evaluated using the fluorescent reporter MitoTimer, which allows for visualization of new and aged proteins. Combining these imaging techniques, I detailed the temporal patterns and partial mechanisms of mitochondrial dynamics and protein turnover. I found that mitochondrial fission is highly active during the ischemic-like phase of injury, whereas fusion is active during early reoxygenation. However, secondary fragmentation events and fusion inhibition were found during the latter stages of reoxygenation. At the same time as changes in dynamics occurred during reoxygenation, protein turnover via LonP1 proteolysis and Parkin-

dependent mitophagy were increased to clear older/oxidized proteins. Additionally, I found that fission (Drp1) and fusion (Opa1) machinery alter mitochondrial protein turnover during physiological and pathological states. Utilizing live cell recordings of mitochondrial dynamics, I identified distinct properties of individual mitochondria performing either fission or fusion. Finally, I summarized my data into an agent-based model of mitochondrial dynamics for predictive *in silico* experimentation. Together, my findings and computational tools greatly enhance our understanding of mitochondrial homeostatic mechanisms in response to I/R injury in neurons.

Chapter I. Introduction

Cerebral ischemia/reperfusion (I/R) injuries, including stroke and cardiac arrest, are leading causes of death and disability (1-3). The mammalian brain requires oxygen, glucose, and other metabolites supplied through cerebral blood flow for proper metabolism and function (4-7). During ischemia, blood flow to the brain is disrupted, leading to an eventual state of energy deprivation. Cerebral ischemia induces neuronal damage, glial cell activation, and endothelial cell dysfunction (8-12). This is considered the primary injury of the pathology. Upon reperfusion, blood flow is restored, along with the supply of oxygen and glucose to the cerebral tissue. Prompt reperfusion is the best clinical practice to limit ischemic injury (13-15). Paradoxically, reperfusion induces a secondary wave of cerebral damage despite return of essential blood and oxygen (16). Secondary injury represents a "treatable" component of the overall injury caused by I/R due to the difficulty of predicting ischemia onset and urgency required for re-establishing blood flow. Increasing our understanding of the mechanisms driving I/R pathophysiology would greatly enhance our ability to treat and limit reperfusion injury.

1.1 Mitochondria in Ischemia/Reperfusion (I/R) Injury

Mitochondria are the primary energy producers of mammalian cells. Mitochondria additionally play multiple roles in the day-to-day operations of the cell, performing critical functions of metabolism, nuclear signaling, organelle-organelle communication, and programmed cell death (17-18). Dysregulation of normal mitochondrial function is a hallmark of cerebral I/R injury. Neuronal mitochondria heavily favor oxidative phosphorylation, with glucose metabolism aid from neighboring astrocytes (19-21). The lack of oxygen and glucose during ischemia disrupts mitochondrial oxidative phosphorylation and endangers neuronal ATP supplies. During oxidative phosphorylation, oxygen is a key substrate for the final electron acceptor cytochrome c oxidase (22,23). The mechanism of electron transport during oxidative phosphorylation drives protons across the inner mitochondrial membrane, establishing a proton gradient. This gradient produces a proton motive force that is then utilized by ATP synthase for ultimate ATP production (24-25).

This proton motive force makes up a majority of the electrochemical gradient that controls the electron transport chain and respiration, called the mitochondrial membrane potential (25). During ischemia, the mitochondrial membrane potential depolarizes due to reduced proton pumping by the complexes of the electron transport chain (28,29). Additionally, ischemic mitochondria act as a Ca^{2+} sink for the cell (30,31). While generally an activator of oxidative phosphorylation, mitochondrial Ca^{2+} during ischemia cannot drive respiration forward due to oxygen scarcity (32-34). However, Ca^{2+} can act to dephosphorylate cytochrome c oxidase as a primer for future electron transport activity (35-36). Primed cytochrome c oxidase can proceed again upon reperfusion. The Ca^{2+}-dependent increase in electron transport chain activity reestablishes the mitochondrial membrane potential, but can also cause hyperpolarization of the mitochondrial membrane potential and drive the production of reactive oxygen species (ROS) (34,37-39). Prolonged hyperpolarization and ROS production can be detrimental to mitochondrial structure and function (40,41). Given the important roles of mitochondria in energy production, stress signaling, and programmed cell death, mitochondrial dysfunction is a critical lynchpin in the pathophysiology of cerebral I/R injury.

1.2 Mitochondrial Dynamics

The energy production capacity and overall health of a cell are dependent on the maintenance of mitochondrial homeostasis. The mitochondrial life cycle is dictated by several physiological mechanisms, including both mitochondrial dynamics and quality control (42). Mitochondria are dynamic agents that constantly undergo fission and fusion to maintain mitochondrial architecture (Fig. 1-1) (43). Fission acts to segment mitochondria for the isolation and removal of damaged proteins, mitochondrial DNA (mtDNA) mutations, and dysfunctional components (44,45). In contrast, fusion constructs and stabilizes mitochondrial networks to promote efficient energy production and mitochondrial matrix equilibrium (46,47). Together, fission and fusion dynamics coordinate the form of the mitochondrial network to protect and preserve efficient function and homeostasis (48).

Mitochondrial Fission

Division of the mitochondrial network via mitochondrial fission is executed by the GTPase dynamin-related protein 1 (Drp1) (49-50). Normally residing in the cytosol, Drp1 translocates to the mitochondrial outer membrane upon activation by post-translational modifications (47,51-53).

On the surface of mitochondria, Drp1 can bind to four identified receptors: Fis1, Mff, MiD49, and MiD51 (54-55). While interactions between Drp1 and all four receptors are capable of executing fission, Mff and Fis1 are the best characterized receptors for physiological and stress-induced fission, respectively (54,56,57). Drp1 oligomers bound to fission receptors form constrictive rings around mitochondria to begin hydrolysis and scission (59-61). ER tubules and actin filaments cooperate with fission machinery to complete ultimate membrane division (62-64). The activation of Drp1-mediated fission is regulated by calcium transients, ROS, electron transport chain integrity, and mitochondrial membrane potential, although it is experimentally difficult to determine the singular causality of each of these variables (65-69). Mitochondrial fission reciprocally mediates numerous aspects of mitochondrial function. Fission is important for isolation and clearance of dysfunctional mitochondrial components (44,50). Overactive mitochondrial fission and a fragmented mitochondrial network can lead to increased ROS production, dysregulated metabolism, and disruption of energy homeostasis (70-74). It is therefore imperative to keep a balanced level of mitochondrial fission to maintain cellular homeostasis.

Mitochondrial Fusion

Mitochondrial fusion is driven by separate machineries at the inner and outer mitochondrial membranes. On the outer membrane, the GTPases mitofusin 1 and 2 (Mfn1 and Mfn2) unfold and adopt a stalk-like structure upon GTP binding. Mfn1/2 monomers then dimerize with counterpart Mfn1/2 monomers on adjacent mitochondria. Mfn1/2 GTP hydrolysis brings the membranes of the mitochondria close together. The outer membrane then destabilizes for formation of a hemifusion diaphragm, allowing fusion to occur (42,75,76). At the inner membrane, optic atrophy 1 (Opa1) mediates both inner membrane fusion and cristae dynamics. During fusion, Opa1 oligomers create membrane protrusions with limited stability on adjacent membranes. Lipid mixing between the two protruding membranes forms a fusion pore that can be driven to full fusion by Opa1 GTPase activity (75,77). Opa1-mediated membrane fusion requires a balance of short (S-Opa1) and long (L-Opa1) Opa1 isoforms (78,79). The Opa1 assemblies acting during inner membrane fusion are composed of equal parts L-Opa1 and S-Opa1 (75). Imbalance of Opa1 isoforms can lead to incomplete or inefficient fusion (80). Similar to fission, mitochondrial fusion has bidirectional relationships with mitochondrial factors, including ROS, Ca^{2+}, and bioenergetics (68,74,81). Mitochondrial fusion is the primary mechanism of equilibration across the

mitochondrial network of a cell, as few other mechanisms exist for distribution and dispersal of mitochondrial proteins, DNA, and metabolites (82,83).

Mitochondrial Dynamics in Cerebral I/R

Mitochondrial dynamics are known to be highly active during cerebral I/R injury and can modulate injury progression and severity (42,84). *In vitro* and *in vivo* studies have demonstrated primary mitochondrial fission during ischemic states in neurons and the brain (85-89). This initial wave of fragmentation is generally attributed to ROS production at the onset of ischemia and broad mitochondrial depolarization throughout the ischemic phase (28). The onset of reperfusion generates a large ROS burst during the initial moments of reoxygenation (34,90). Despite this ROS burst, mitochondrial fission slows or halts during early reperfusion, with variable onset of mitochondrial fusion (85,86,89). Intriguingly, mitochondrial fusion slows during the latter stages of reperfusion, bringing forth a secondary wave of mitochondrial fission (85,86,91). This time is additionally associated with bioenergetic failure, high ROS production, mitochondrial permeability transition, and programmed cell death (42,85,93,94). Critically, modulation of mitochondrial dynamics can improve outcomes after neuronal I/R injury (95-99). Increasing our understanding of the mechanisms and timing of mitochondrial dynamics in I/R will greatly aid the development of therapeutics targeting mitochondria.

1.3 Mitochondrial Quality Control

In addition to their own genome and encoded-proteins, mammalian mitochondria contain > 1000 proteins that are nuclear-encoded (100). Given their large proteome and critical functions, mitochondria require fine-tuned maintenance of structural and functional components to ensure cellular health (101,102). Maintenance of the mitochondrial proteome, and resultant mitochondrial homeostasis, is mediated by both mitophagy and intramitochondrial proteostasis (101,103). Defects in these mitochondrial quality control pathways are linked to neurological diseases (e.g. Parkinson's Disease, amyotrophic lateral sclerosis) and injuries (e.g. stroke, traumatic brain injury) (42,104-106). Mitochondrial quality control mechanisms collectively remodel and adapt mitochondria and their essential components.

PINK1/Parkin Mitophagy

Mitophagy, the autophagic degradation of mitochondria, includes engulfment of whole organelles as well as selective removal of mitochondrial components via mitochondrial derived

vesicles (107,108). The best characterized form of mitophagy in neurons is the stress-responsive PINK1-Parkin pathway (Fig. 1-2) (42,107,109). The kinase PINK1 is continually imported into mitochondria under basal conditions where it is quickly degraded by intramitochondrial proteases (110). When mitochondria become depolarized, PINK1 import is halted, leading to accumulation of PINK1 on the outside of mitochondria (111,112). At the mitochondrial surface, PINK1 phosphorylates ubiquitin chains to recruit the cytosol-resident E3 ubiquitin ligase Parkin, along with other autophagy receptors (113,114,115). Similar to ubiquitin, PINK1 phosphorylates Parkin at Ser65 on its ubiquitin-like-domain to activate Parkin activity (116-118). Parkin activation leads to ubiquitination of key mitochondrial outer membrane proteins, generating more ubiquitin substrates for PINK1 kinase activity (119-121). Phosphorylation of Parkin-constructed ubiquitin chains stabilizes Parkin translocation and creates a feedforward loop between PINK1 and Parkin (116,122). The K-linkage of Parkin synthesized ubiquitin chains determines the ultimate fate of the ubiquitinated protein, although the majority of Parkin activity is associated with initialization of macro-autophagy (123-125). K63-linked ubiquitin chains and ubiquitin monomers phosphorylated by PINK1 at Ser65 recruit autophagy receptors to mitochondria, namely Optineurin, p62, and NDP52 (115,126-129). Autophagy receptors then recruit LC3-expressing phagophores to mitochondria for engulfment, with conditional necessity of phosphorylation by the kinase TBK1 (125,128,130). Sequestration of mitochondria by the phagophore leads to maturation into an autophagosome that will eventually fuse with the lysosome for breakdown of the mitochondrial components. The PINK1/Parkin pathway has been extensively studied in neurons due to PINK1 and Parkin mutations causing autosomal Parkinson's Disease (131). While the extent of basal PINK1/Parkin mitophagy in neurons is debated (132-134), overwhelming evidence in many disease/injury models suggest its critical role in clearing damaged and dysfunctional mitochondria (42,108,109).

Intramitochondrial Proteases

Mitophagy has long been the focal point of research into mitochondrial quality control and its relation to injury and disease. However, mitochondria also have the ability to remodel their proteome from within via intramitochondrial proteostasis. Mitochondria are home to their own diverse set of proteases and peptidases that work within the organelle to process, cleave, and degrade their own proteins and protein complexes (Fig. 1-3) (103,135). These mitochondrial proteases serve in distinct roles, often dictated by the compartment in which they reside. Proteases

localized to the intermembrane space and inner mitochondrial membrane serve to regulate functions related to protein import and protein complex assembly (136-140). In contrast, matrix-localized proteases play a larger role in protein maintenance and degradation. The two dominant matrix proteases, LonP1 and CLPP, are critical for the degradation of oxidized/misfolded proteins and turnover of damaged components of the electron transport chain (141-144). Aside from mitochondrial maintenance, mitochondrial proteases additionally act as initiators of critical cell signaling pathways. The intermembrane protease Oma1 mediates an unfolded protein response (UPR)-like pathway through cleavage and release of DELE1, which traffics back towards the nucleus to activate integrated stress response components (145,146). The soluble proteases PARL and LonP1 drive PINK1 degradation, a key process for limiting mitophagy of healthy mitochondria (110,147). The serine protease Omi (also known as HtrA2) is a critical mediator of apoptosis, with apoptosis-inhibiting proteins as its putative substrates (148-150). Collectively, mitochondrial proteases mediate numerous aspects of mitochondrial and cellular homeostasis, while also activating and modulating key stress pathways.

Mitochondrial Quality Control in Cerebral I/R

Due to mitophagy's role in clearing damaged and dysfunctional mitochondria, its prevalence in I/R injury is not surprising. In both cell culture and small animal models of neuronal I/R injury, autophagy and mitophagy machinery is upregulated, along with mitophagic flux (82,151-153). Despite extensive study, it is still unclear as to the timing of mitophagy with reports of induction during both the ischemic and reperfusion phases of injury (82,154-156). Also debated is the association between mitophagy and outcomes after neuronal I/R injury. Conflicting reports in similar models present mitophagy as either neuroprotective or an overactive mechanism potentiating mitochondrial dysfunction. Zhang et al. (153) report that in both *in vitro* and *in vivo* models of I/R injury that autophagy inhibition (pharmacological and genetic) during reperfusion exacerbates neuronal injury. Similarly, enhancing mitophagy has been demonstrated to be a viable neuroprotective strategy (157-159). These findings have made enhancing mitophagy during reperfusion an attractive mechanism for potential therapeutics (160-163). However, other studies demonstrate that excessive mitophagy can exacerbate neuronal damage in cell culture and animal models of cerebral I/R injury (156,164-166). Mitophagy is an energetically-expensive process that requires coordination between multiple organelles, which can be even further complicated in neurons, which require retrograde transport of axonal/synaptic mitochondria back to the soma for

autophagic degradation during I/R injury (167). Further work is required to disentangle the beneficial versus detrimental effects of mitophagy in I/R, however, much of the variability may be related to injury severity, neuronal cell types, and/or energy availability.

Much less is known about the role of mitochondrial proteases during neuronal I/R injury. Mitochondrial proteases are nuclear-encoded, which therefore delays any changes in their abundance in mitochondria (103). This complicates our study of mitochondrial proteases during acute injuries, as few protease-specific activity assays exist, making expression and protein levels the default methodology. Nevertheless, several studies have examined protease levels during neuronal and cerebral I/R injury. The proteases LonP1 and Omi/HtrA2 have been shown to increase during the later stages of reperfusion (169-171), while the PINK1-degrading protease PARL decreases with injury (172). The inner membrane proteases Oma1 and Yme1L are responsible for cleaving the fusion protein Opa1 into its short isoforms. The balance of Opa1 isoforms can therefore be used as a surrogate for Oma1 and Yme1L activity. Opa1 cleavage is increased during I/R injury, but the protein levels of Oma1 and Yme1L remain stable (173,174). These findings highlight the need for examining mitochondrial protease activity, in addition to protease expression, to truly understand their role in I/R injury. In non-neuronal cells, mitochondrial proteases degrade misfolded and oxidized mitochondrial proteins, including essential components of the electron transport chain, in models of hypoxia and mitochondrial dysfunction (143,175-178). Extensive work is needed to increase our understanding of how intramitochondrial proteostasis contributes to I/R injury, as greater than 60% of mitochondrial protein turnover is regulated by autophagy-independent mechanisms (132).

1.4 Interplay Between Dynamics and QC Pathways

Mitochondrial dynamics and quality control systems display coordinated activity to maintain mitochondrial homeostasis (179,180). Among the best characterized relationships is that of mitochondrial fission and mitophagy. At the basic level, the relationship seems natural, as phagophore elongation and autophagosome formation is at some point limited by size, and therefore cannot sequester mitochondria over an unknown threshold. Beyond size, fission is critical for the isolation of dysfunctional mitochondrial segments/components (44). In certain contexts of injury, mitochondrial fission precedes and increases mitophagy, although this relationship is potentially only correlative as both fission and mitophagy are triggered by

mitochondrial depolarization and dysfunction (181-184). Loss of the fission regulator Drp1 decreases mitophagic flux and halts Parkin-independent mitophagy (185,186). Reciprocally, loss of the mitophagy initiator PINK1 increases mitochondrial fission (185). Burman et al. (187) proposed a more nuanced model in which Drp1-mediated mitochondrial fission acts a protector of healthy mitochondria by severing dysfunction segments, allowing for PINK1/Parkin mitophagy to proceed only on fission-produced dysfunctional mitochondria. Fission thereby regulates the specificity of PINK1/Parkin-mediated mitophagy for dysfunctional mitochondria (187). Aside from PINK1/Parkin mitophagy, Drp1 is required for the biogenesis of mitochondrial-derived vesicles, which act to selectively remove mitochondrial proteins and mitochondrial DNA-containing nucleoids (108,134,188). The relationships between fission and mitochondrial proteases have not been described, although loss of the fission receptor Fis1 impairs overall mitochondrial proteostasis in *Drosophila* muscle (189).

A bidirectional relationship between mitochondrial fusion and mitophagy has additionally been demonstrated (179). As a part of the phospho-ubiquitin cascade that occurs during PINK1/Parkin mitophagy, the outer membrane fusion protein Mfn2 becomes ubiquitinated (124,190). Ubiquitination of Mfn2 can lead to both selective degradation of Mfn1/2 complexes, as well as increased autophagy receptor recruitment for mitophagy initiation (124,190). Therefore, Mfn1/2-mediated fusion is inhibited and mitophagy is increased. Similarly, Mfn2 inhibition and knockout decreases general autophagy and mitophagy, and Mfn1 overexpression increases mitophagy, further strengthening this relationship (151,191,192). These effects may be specific to Mfn1/2 rather than fusion, as overexpression of the inner membrane fusion protein Opa1 leads to decreased mitochondrial sequestration in autophagosomes (184). Many outstanding questions remain as to the relationships between mitochondrial fusion and mitochondrial quality control pathways that prompt further investigation.

1.5 Overview of Thesis

Secondary injury and mitochondrial dysfunction have been described during acute times after reperfusion, presenting a therapeutic window for mitochondrial intervention and neuroprotection. The aim of my thesis was to evaluate the patterns and mechanisms of mitochondrial dynamics and proteostasis during the therapeutic window of neuronal I/R injury. Utilizing a primary neuron model of oxygen-glucose deprivation and reoxygenation (OGD/R), I

applied novel imaging techniques and analyses to quantify mitochondrial dynamics and proteostasis throughout I/R injury (Chapters II & III). Further, I examined the interplay between dynamics, mitophagy, and proteostasis (Chapters III & IV). Finally, I synthesized these techniques and findings into a computational agent-based model of mitochondrial dynamics that simulates observed patterns from neuron OGD/R experiments (Chapter V). I went on to demonstrate the potential utility of this model for therapeutic trial design and execution. These findings provide novel insights into the roles of mitochondrial dynamics and protein turnover in neuronal I/R injury with high temporal resolution. The data and predictive model produced in this thesis will critically inform future research into and trials of mitochondria-targeting neuroprotective strategies in cerebral I/R injury.

1.6 Figures

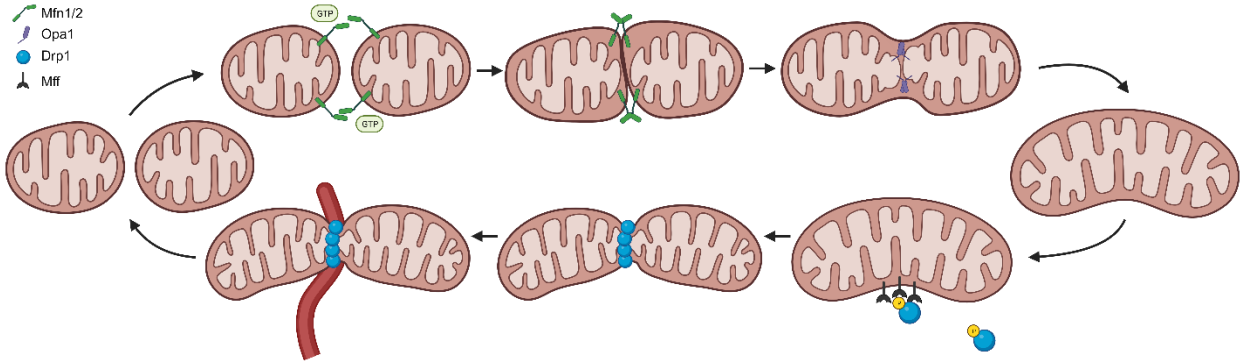

Figure 1-1. Mitochondrial fission and fusion

Mitochondrial fusion (upper row) begins with GTP-activated unfolding of Mfn1/2 monomers on adjacent mitochondria. Dimerization of Mfn1/2 bring two mitochondria closer together to being outer membrane fusion. Inner mitochondrial membrane fusion is driven by Opa1, which creates protrusions in the inner membrane to begin matrix fusing. Mitochondrial fission (lower row) is activated by post-translational modification of Drp1 and accumulation of Drp1 receptors (Mff, Fis1, MiD49, MiD51) on the outer mitochondrial membrane. Drp1 forms an oligomeric ring around the site of fission. ER tubules come in close association with the fission site to complete division.

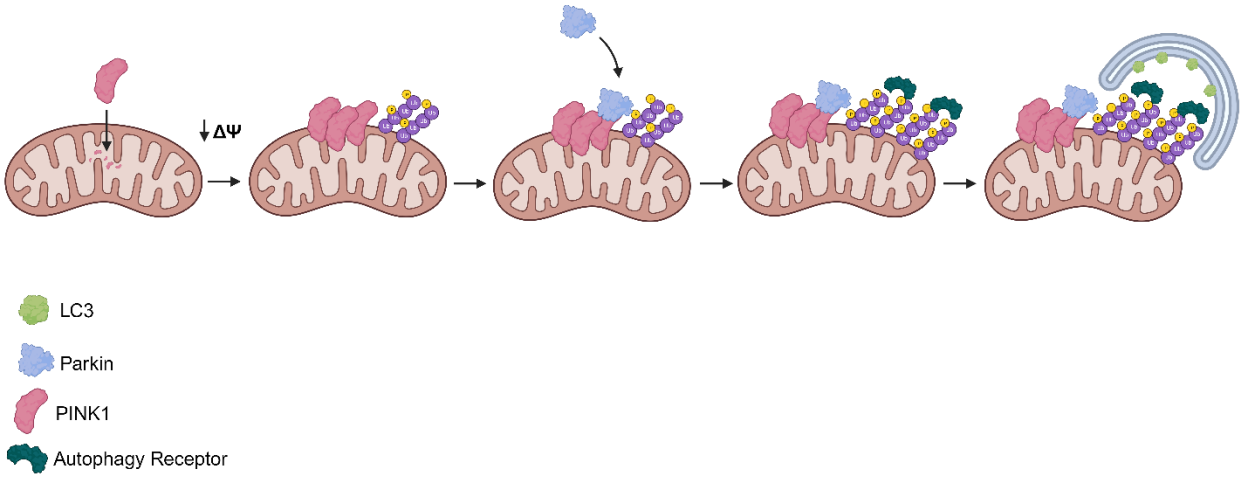

Figure 1-2. PINK1/Parkin mitophagy

PINK1 is continually imported to mitochondria where it is quickly degraded by intramitochondrial proteases. Import of PINK1 is dependent on mitochondrial membrane potential (ΔΨ), thus ΔΨ depolarization leads to halted import and accumulation of PINK1. On the outer mitochondrial membrane, PINK1 phosphorylates ubiquitin monomers and chains to recruit Parkin. The E3 ubiquitin ligase Parkin is additionally phosphorylated by PINK1 and generates more ubiquitin chains on the outside of mitochondria. The phosphor-ubiquitin chains recruit autophagy receptors (e.g. OPTN) to mitochondria and eventually bind to LC3 on phagophores to initiate macro-autophagy.

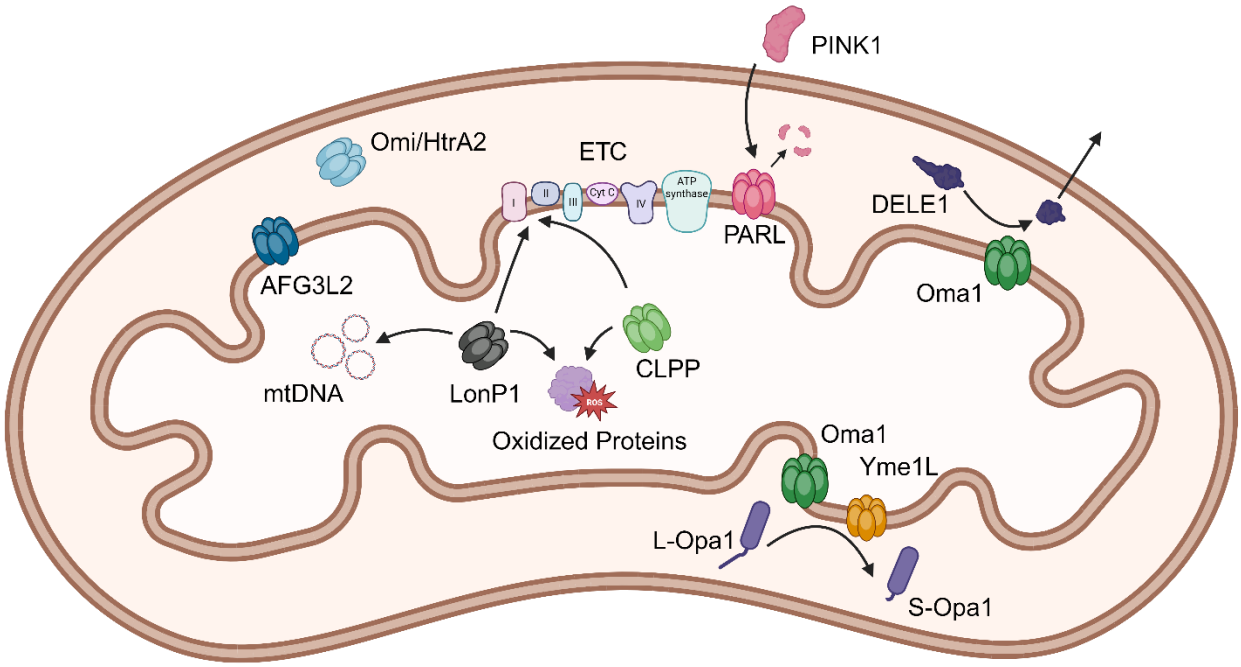

Figure 1-3. Intramitochondrial proteases

Mitochondria have their own unique set of proteases and peptidases that exert different critical functions. Embedded in the inner mitochondrial membrane, Oma1 and Yme1L cleave the fusion protein Opa1 for balanced Opa1 isoform distribution. Oma1 additionally cleaves DELE1 to initiate stress signaling to the cytosol. PARL is the predominant protease for PINK1 degradation, a critical step in limiting mitophagy induction. In the matrix, LonP1 and CLPP degrade oxidized and damaged proteins, including components of the electron transport chain (ETC). LonP1 is additionally responsible for maintaining mitochondria nucleoids that contain mitochondrial DNA (mtDNA) and key transcriptional machinery.

Chapter II. Machine Learning-based Classification of Mitochondrial Morphology in Primary Neurons and Brain [1]

2.1 Introduction

Mitochondria are highly dynamic organelles that exist in a network that is constantly elongating and dividing. Under normal conditions the mitochondrial network is in an equilibrium state of long, interconnected networks and short punctate mitochondria, and maintaining this balanced state is critical for mitochondrial homeostasis, cell stability, and cell survival (179,193,194).

Mitochondrial fission (division) and fusion (elongation) events give rise to distinct morphologies. The ever-changing state of mitochondrial morphology is regulated by a family of dynamin-like GTPases, which consist of the fission protein dynamin-related protein 1 (Drp1) as well as the fusion proteins mitofusin (Mfn) 1&2 and optic atrophy 1 (Opa1). Fission of mitochondria plays an important role in segregating unhealthy mitochondria that contain dysfunctional proteins, destabilized membranes, and mutated or damaged mitochondrial DNA (mtDNA) (183,195-198). Alternatively, fusion aids in the equilibration of matrix metabolites, intact mtDNA, and membrane components such as electron transport complexes (195,199-201).

Dramatic alterations in mitochondrial network architecture have been observed in cell cycle progression, cellular differentiation, oxidative stress, metabolic perturbation, and induction of programmed cell death pathways (17,42,193,202-206). Despite the effort to study the phenotypic heterogeneity of mitochondria under these various conditions, investigations have been limited by their measures of mitochondrial morphology, often resorting to manual classification of simple morphologic states, e.g. fused versus fragmented. Studies typically utilize a qualitative or

[1]This chapter contains excerpts of the published manuscripts: "Fogo GM, Anzell AR, Maheras KJ, Raghunayakula S, Wider JM, Emaus KJ, Bryson TD, *et al.* (2021). Machine learning-based classification of mitochondrial morphology in primary neurons and brain. *Sci Rep.* 11(1), 5133."
"Anzell AR, Fogo GM, Gurm Z, Raghunayakula S, Wider JM, Maheras KJ, Emaus KJ, et al. (2021). Mitochondrial fission and mitophagy are independent mechanisms regulating ischemia/reperfusion injury in primary neurons. *Cell Death Dis*. 12(5), 475." Anthony Anzell and I co-led the analysis of mitochondrial morphology in OGD/R. I performed all remaining experiments.

semi-quantitative approach by developing a scoring system of fission/fusion profiles or binning mitochondria based on length (85,158,207,208), both of which lack, on a large-scale, sampling size, and an accurate and precise assessment of physiologically relevant mitochondrial morphologies. To overcome this, recent studies have shifted to utilizing computational image analysis, commonly referred to as image cytometry, which limits observer and selection bias in morphological evaluations and demonstrates high throughput capabilities (209-212).

Computational image analysis of mitochondrial morphology using machine learning techniques offers the advantages of generating accurate classification and quantitation of different morphologies with fast and efficient large-scale application. Although this method provides robust and accurate analysis of mitochondrial morphology, the availability and expertise required to utilize machine learning software presents a barrier for investigators. Here, we developed a semi-automated image analysis pipeline, that utilizes open-source software for the quantitation of mitochondrial morphology for both in vitro and in vivo applications. Utilizing mouse primary cortical neurons, our pipeline demonstrates a highly specific and sensitive method of efficiently classifying mitochondrial morphology that can be extended to 3D in vivo applications through immuno-labeling of brain sections as well as serial block-face scanning electron microscopy (SBF-SEM) data.

2.2 Results

2.2.1 Identification of distinct mitochondrial morphologies

Mouse primary cortical neurons were cultured on glass coverslips and immuno-labeled with antibodies targeting ATP synthase on the inner mitochondrial membrane and TOM20 on the outer mitochondrial membrane. Fluorescent microscopy revealed four distinct mitochondrial morphologies: network, unbranched, swollen, and punctate that represent frequent mitochondrial size and shape parameters in neurons (85,89) (Fig. 2-1A). Networks were defined as long sprawling mitochondrial objects ($\sim \geq 5$ μm^2) with one or more branching points. Mitochondria were considered unbranched if they were of intermediate size ($\sim$ 1–4 μm^2), uniform thickness, and did not include a branching point. Punctate objects were defined as small compact objects ($\sim \leq 1$ μm^2). Swollen mitochondria were identified as intermediate sized objects ($\sim$ 1–4 μm^2) with high circularity and roundness.

To validate the independence of these observed morphologies, ATP synthase and TOM20 signals were merged, processed together, and mitochondrial objects were segmented and analyzed using a semi-automated image processing workflow in FIJI (213) (Fig. 2-2). Each mitochondrial object was classified using 32 size and shape descriptors and a principal component analysis (PCA) was applied to evaluate phenotypic differences (Fig. 2-1B). Mitochondrial objects aggregated at discrete quadrants of the PCA plot (Fig. 2-1B), further validating that mitochondrial segregate into distinct morphological phenotypes. Comparisons across individual variables, namely roundness (Round) and interfacial density (Intfc D), also demonstrated the independence of each morphology (Fig. 2-1C).

2.2.2 Machine learning prediction of morphology

Mitochondrial objects (1091 total) were segmented, measured, and hand-classified for the development of a morphological classification model. This hand-classified data set was split into the machine learning train and test sets (80% and 20%, respectively). The training set was used to develop a random forest classification model using the R caret package (214,215). In this model, a mitochondrial object is classified through 500 parallel decision trees, in which each tree provides an output vote. Each object is assigned a predicted morphology at the conclusion of all decision trees based on the morphology with the majority of votes. The model accuracy over 25 training repetitions was 94.6%. For verification of model accuracy, the test set of mitochondrial objects was run through the completed decision tree model. Test accuracy was 95.4% on the 217 hand-classified objects in the test set (Fig. 2-1D). The R functions implemented for model training and evaluation are available on a GitHub repository (https://github.com/sanderson-lab/mitomorphology).

2.2.3 Physiological relevance of morphological phenotypes

To assess physiological relevance, the in vitro machine learning classification workflow was applied to microscopy imaging data of primary neurons after genetic and pharmacological disruption of mechanisms critical for regulating mitochondrial dynamics. The morphologic state of mitochondria in each image is quantified as the percentage of mitochondrial area classified into each morphological phenotype.

The dynamin-like GTPase Opa1 is critical for the remodeling of mitochondrial architecture, namely for its role in mitochondrial inner membrane fusion (195,206,216,217). Disruption of Opa1 prevents mitochondrial fusion, and, based on previous studies using qualitative or semi-quantitative analyses (85,158,207,208), this would be predicted to shift the mitochondrial network toward mitochondrial fragmentation. Primary neurons with conditional knockout (cKO) of Opa1 (Fig. 2-3A) were generated using primary cells from Opa1 floxed mice exposed to either lentiviral-Cre (LV- EF1α -Cre) or an empty vector lentivirus (LV- EF1α -empty) as a control (Fig. 2-3C,D). Opa1 cKO produced a fragmented state, with a decrease in mitochondrial networked area ($p = .0175$) and increases in swollen ($p = .0015$) and punctate area ($p = .0002$; Fig. 2-3B). These changes in morphology are indicative of impaired mitochondrial fusion and increased cellular stress (42,85,206,217,218). These results suggest the formation of mitochondrial networks is at least partially dependent on Opa1-mediated fusion, as many others have shown (217-220).

To produce small punctate mitochondria, the GTPase Drp1 will excise and divide mitochondria (203,221,222). Drp1 cKO was utilized to disrupt mitochondrial fission and shift the mitochondrial network toward a fused network (Fig. 2-4C,D). Drp1 cKO alone did not have any significant effects on the distribution of morphological phenotypes without cellular stressors (42,203,206,223) (Fig. 2-4A). However, when cultures are subjected to 18 h glucose deprivation (GD) as a stressor (Fig. 2-4A), $Drp1^{flx/flx}$ cells show a significant decrease in mitochondrial networked area ($p = .0003$) with concomitant increases in swollen ($p < .0001$) and punctate area ($p < .0001$) (Fig. 2-4B). Drp1 cKO partially rescued normal mitochondrial morphology resulting in significantly lower percent area of punctate mitochondria ($p = .0116$; Fig. 2-4B), demonstrating that the GD-induced punctate phenotype is related to Drp1-mediated mitochondrial fission.

A major contributor to mitochondrial dysfunction and the induction of cell death is the formation and activity of the mitochondrial permeability transition pore (mPTP) (42,224-226). Ca2+-induced mitochondrial swelling through the opening of mPTP is a hallmark of cell death in pathological conditions, such as ischemia/reperfusion injury (42,85,226-230). To assess the reliability of the swollen phenotype and the relevance of this phenotype to pathological mPTP opening and Ca2+ influx, cells were exposed to pharmacological modulation of swelling (Fig. 2-5A). Glutamate and activation of its N-Methyl-D-aspartate (NMDA) receptor are known stimulators of mitochondrial swelling and transient mPTP opening (231,232). Cells treated with

100 μM glutamate and 10 μM co-agonist glycine caused an increase in swollen ($p < .0001$) and punctate mitochondrial area ($p = .0002$), along with a subsequent decrease in networked ($p = .0025$) and unbranched area ($p = .0118$; Fig. 2-5B). To determine the dependence of this observation on Ca2+ handling and mPTP activity, cells were pre-treated and co-incubated with glutamate and the mitochondrial calcium uniporter (MCU) inhibitor Ru360 and mPTP inhibitor cyclosporin A (CsA) (224,233-237). Treatment with the inhibitors alone decreased unbranched area ($p = .0004$) and increased networked area ($p = .0449$; Fig. 2-5B), potentially due to the interconnected relationship between Ca2+ and Drp1 during remodeling of mitochondria (51,194,195,238). Furthermore, Ru360 and CsA administration reduced glutamate-induced mitochondrial swelling and fragmentation (Fig. 2-5B), suggesting the swollen morphological phenotype is associated with mPTP opening and mitochondrial Ca2+ homeostasis.

2.2.4 Workflow application to 3D resolution

A critical limitation of standard morphological analyses of mitochondria, including the in vitro classification model, is the lack of 3D resolution. Cells and organelles have complex three-dimensional architecture and morphology, and inclusion of this 3D resolution can add important details to mitochondrial morphologic analysis. To address this concern, morphological classification workflow was expanded from 2D resolution in cell culture to 3D resolution in tissue histology. Mouse brain tissue sections immuno-labeled for ATP synthase were imaged using fluorescent confocal microscopy of the CA1 hippocampus. Mitochondrial objects were segmented in individual images over a z-series of 50 slices (5 μm total) and stitched together for 3D reconstruction in FIJI using the MorphoLibJ Connected Components Labeling plugin (239) (Fig. 2-6A–D). Mitochondrial objects were then measured using 8 size and 3D shape descriptors (Fig. 2-6B). Through inspection of 3D renderings, mitochondrial objects were hand-classified by morphology (Fig. 2-6A). Identical to the method described for cell culture, a random forest model was constructed and evaluated using 170 hand-classified mitochondrial objects. Model training with 8 size and 3D descriptors had an accuracy of 76.6%, while the test set was classified with 84.9% accuracy. An expanded descriptor set can be implemented, similar to the primary neuron model, to increase accuracy to meet the needs of each experimental objective.

The same methodology of 3D object measurement, rendering, and classification was applied to serial block-face scanning electron microscopy (SBF-SEM) images of rat brain sections

from the CA1 hippocampus (Fig. 2-6E–H). Mitochondrial objects in individual images were segmented in an automated manner using trainable Weka segmentation (240) (Fig. 2-7). SBF-SEM sections were analyzed in z-series stacks of 100 slices each (7 μm total). A random forest model was trained and tested on 231 hand-classified mitochondrial objects. The accuracy for training and testing was 74.7% and 86.4%, respectively. Our confocal and SBF-SEM imaging results serve as primary evidence that this analytical pipeline can be scaled to 3D resolution with versatility and reliability.

2.2.5 Mitochondrial morphology during primary neuron OGD/R

We next sought to determine the temporal pattern of mitochondrial dynamics in a primary neuron model of I/R injury, oxygen-glucose deprivation and reoxygenation (OGD/R). We utilized our machine learning classification workflow to quantify mitochondrial dynamics during OGD/R and the relative contributions of Drp1. We quantified both mitochondrial objects and sum area of mitochondria in each morphologic state between conditions LV-empty (negative control) and LV-Cre (i.e. Drp1 cKO) in $Drp1^{flx/flx}$ neurons. Morphological classification in lentiviral-control neurons revealed significant reductions in networks and unbranched mitochondrial objects in cells subjected to OGD/R vs control (Fig. 2-8). Drp1 cKO mitigated the OGD/R-associated reduction in unbranched mitochondria (Fig. 2-8), and a similar group trend was observed for network objects ($F = 4.526$, $p = 0.0516$; Fig. 2-8). In agreement with the mitochondrial object counts, the area of mitochondrial networks as a percent of total mitochondrial mass was significantly reduced at early reoxygenation time points (Fig. 2-8). Moreover, this reduction in mitochondrial area was attenuated in Drp1 cKO neurons, thereby implicating Drp1 in mitochondrial network fragmentation during OGD/R (Fig. 2-8). Although the number of unbranched mitochondria decreased during OGD/R, the area of unbranched mitochondria was not reduced following reoxygenation. Drp1 cKO inhibited the decrease in number of unbranched mitochondrial objects, and the area occupied by unbranched objects remained comparable in cells subjected to OGD/R vs control (Fig. 2-8). This suggests that unbranched mitochondria remain a stable percentage of the total mitochondrial pool but increase in size to compensate for the decrease in object number. Interestingly, mitochondrial area in the unbranched state was significantly lower in Drp1 cKO neurons compared to lentiviral control. These data suggest that Drp1 is essential for maintaining unbranched mitochondrial size, and Drp1 cKO results in shorter unbranched mitochondria without disrupting the number of mitochondria under control conditions (Fig. 2-8).

Interestingly, there was no increase in the number of punctate objects in lentiviral-control neurons in response to OGD/R; however, there was a significant increase in the total area of mitochondria in a punctate state, an increase that was attenuated with Drp1KO (Fig. 2-8). These data suggest that punctate mitochondria are larger during OGD/R, and that Drp1 activity may induce a rapid transition from punctate mitochondria to a swollen mitochondrial phenotype. Most notably, both the number and the total area of mitochondria in a swollen state increased significantly in control neurons throughout OGD/R, and these increases were attenuated by Drp1 cKO (Fig. 2-8).

2.3 Discussion

Mitochondrial morphology is a representative snapshot of the underlying processes of mitochondrial dynamics and quality control. Emerging evidence suggests that the paradigm of mitochondria as effectors of injury extends beyond the integrity of the organelle to encompass the balance between fission and fusion phenotypes and the interface with processes responsible for cell death. Analyses of these morphologic alterations have traditionally been performed using qualitative approaches or simple quantitative measurements (85,158,207,208). However, recent advances in imaging techniques and the availability of computational resources make more advanced analysis of morphology feasible. Several groups have developed software and codes/macros for the unbiased measurement and classification of mitochondrial morphology (209-212). To further these efforts, we developed a machine-learning based classification pipeline for the identification of distinct physiological and pathological morphologies using free and open-source software with 2D and 3D capabilities.

Utilizing software and plugins freely and readily available to investigators in the biomedical sciences, we designed a workflow for high throughput image processing, segmentation, and analysis that is customizable to various biological models (213,214,239,240). Starting in cell culture, we identified morphological phenotypes that we hypothesized to be indicative of physiological and pathological mechanisms of mitochondrial dynamics. Using a combination of size and geometric descriptors, we verified the distinct nature of these phenotypes and our ability to classify them by visual observation. Through the application of machine learning in the R caret package, we developed a classification model with high sensitivity and specificity for these morphological phenotypes (214). Implementation of machine learning classification and

semi-automated image processing removes opportunity for bias and inconsistency in morphological analysis, thereby increasing the rigor and reproducibility of these procedures (209,241). Furthermore, we have demonstrated the utility and versatility of our pipeline through 3D analysis in confocal and SBF-SEM imaging. The applications of our workflow in 3D serves as proof-of-concept that high throughput analyses of mitochondrial morphology can be accomplished with high sensitivity in larger biological models. This technique has the potential to be a significant advancement to standard morphological analysis of mitochondria in cell culture, intact tissue samples, and tissue in vivo live imaging.

Mitochondrial analyses in cell culture models have traditionally been performed with 2D resolution, as many cell types grow in a monolayer in vitro. Imaging and analyzing in 2D reduces the need for advanced imaging techniques and high computational power. However, cells and their organelles exist in 3D and therefore 2D analyses may not provide precise results. To address this limitation, we utilized our 2D workflow as a foundation for the construction of an adaptable 3D analysis methodology. Additionally, a critical limitation of the analyses performed in this study is the lack of cell type specificity. The mitochondrial labeling strategies implemented were not specific to neurons. It is therefore likely that mitochondria from surrounding glial cells and other cells of neurovascular unit were included. The methodologies we have developed have tremendous utility for future studies with research questions relating to specific cell types. Our workflows are easily adaptable for cell type specific mitochondrial labeling strategies, namely genetically encoded fluorescent reporters targeted to mitochondria.

Although our workflow will require evaluation and confirmation in other cell types, tissues, and disease models, we believe our approach has the potential to be customizable for an investigator's biological model of interest and research question. This versatility is a great asset, but also presents its own limitations. As is always the case with machine learning, a classification model is only as good as its training data. Development of a reliable and sensitive model is dependent on consistent and accurate hand-classification of the train/test set and useful input variables. Inappropriate selection of input variables or inconsistent hand-classification can lead to faulty models. Additionally, with high throughput image analysis, it is critical to verify objects of interest are not lost or altered in processing and segmentation. As an example, during analysis of 3D mitochondrial objects, we observed a "ballooning" effect in which binary objects after

segmentation were enlarged compared to the mitochondrial signal in the original images. This effect was reduced through the implementation of a morphological erosion step during binary image processing (239). A limitation specific to automated SBF-SEM analysis is segmentation based on pixel intensity. We trained a Weka segmentation model for the automated extraction of mitochondrial objects from SBF-SEM images. This technique greatly improved our sampling ability and analysis efficiency. However, application of this method generated a "survivor"-like bias, where mitochondria with severe cristae dysfunction were unintentionally discarded during segmentation, leading to a likely underestimation of swollen mitochondria. It is important to note that application of our proposed pipeline is also possible without automated segmentation. Therefore, possible biases introduced during automated processing and segmentation can be avoided by implementing the classification protocol without batched image segmentation.

Our results in primary neuron OGD/R demonstrate a multi-phasic pattern of mitochondrial dynamics in neuronal I/R injury, as others have demonstrated (85,86,89,91). The initial OGD (i.e. ischemic) phase presents mitochondrial fragmentation to the punctate morphology, an effect that is dependent on Drp1. Interestingly, Drp1-dependent fission appears to be required for mitochondrial swelling, as swollen mitochondria formation did not increase in Drp1 cKO neurons. The onset of reoxygenation slowed mitochondrial fragmentation and produced marginal rebuilding of the mitochondrial network. After 2h reoxygenation, the rebuilding halted, and punctate mitochondria began to form again. This secondary fragmentation event has also been observed in other studies of neuronal I/R injury. Together, our results demonstrate a quantitative timeline of mitochondrial dynamics during acute reoxygenation after neuronal OGD and illustrate the key role that Drp1 plays in producing punctate and swollen mitochondria.

There is an increasing need to bridge the fields of computer science, mathematics, and artificial intelligence with the biomedical sciences. Detailed analysis with computational and imaging techniques will greatly advance our understanding of complex biological processes and increase reproducibility in research. Here we describe a semi-automated machine learning-based workflow for the 2D and 3D analysis of mitochondrial morphology using free and open-source software. Our method of morphological classification offers much needed versatility, such that investigators can apply the technique to their biological model and imaging technique of interest.

The application of this quantitative method will greatly increase the efficiency and reproducibility of assessing mitochondrial morphology throughout the field.

2.4 Materials and Methods

Animals

All procedures were performed in accordance with institutional and ARRIVE guidelines and approved by the University of Michigan and Wayne State University Institutional Animal Care and Use Committees (IACUC). Mice were maintained on a 12 h light/dark cycle with standard rodent chow and water available ad libitum. Wild-type (WT) mice (C57BL/6Crl) were purchased from Charles River Laboratories (Wilmington, MA). Drp1 floxed (Drp1flx/flx) mice (Dnm1ltm1.1Hise) were generously provided by Hiromi Sesaki, Johns Hopkins University, Baltimore, MD (242). Opa1 floxed (Opa1flx/flx) mice were generously provided by Luca Scorrano, University of Padua, Italy (243). All mouse models were backcrossed to C57BL/6Crl background. Sprague Dawley rats were obtained from Envigo (Indianapolis, IN).

Primary neuron culture

Postnatal day 0–2 (P0–P2) mouse pups were sacrificed by decapitation. Cerebral cortices were dissected and minced prior to incubation in enzyme digestion solution (1 × hibernate complete medium, 0.06 mg/mL l-cysteine (Sigma, 778672), 1.4 × 10−2 N NaOH (Sigma, 43617), 10 ng/mL APV (2-Amino-5-phosphonopentanoic acid, Sigma, A-5282), with 50 uL Papain (Worthington, LS 03126)) for 30 min at 37 °C. Following digestion, tissue was washed with DPBS and dissociated in complete Hibernate-A medium. Cells were seeded onto 0.1% PEI-coated glass coverslips at a density of 160,000 cells/cm^2. After 30 min, complete media change was performed with neurobasal complete medium (1 × Neurobasal Plus medium (Gibco, A3582901), 1% B27 Plus (Gibco, A3653401), 0.5 mM Glutamax Supplement (Gibco, 35050061), and 1 Penicillin/Streptomycin Solution (Gibco, SV30010)). Cells were incubated at 37 °C in 5% CO2 for 14 days. Half-media changes were performed every 3–4 days with neurobasal complete medium.

Lentiviral transduction

Lentiviral infection was performed 7 days prior to experimentation, on day-in-vitro 7 (DIV7). Lentiviral plasmids and lentivirus were generated by the vector core at the University of Michigan: Lenti-EF1α-Cre-VSVG, Lenti-EF1α-VSVG. Viruses were prepared in Neurobasal

Medium (Gibco, 21103049). For cKO experiments, an empty vector lentivirus (Lenti-EF1α-VSVG) was administered to floxed cells to serve as controls.

Pharmacological treatment

For glucose deprivation, cells were incubated in EBSS no glucose medium ((0.20 g/L CaCl2 (Spectrum, CA138500GM), 0.4 g/L KCl (Fisher Chemical, P217-500), 0.097 g/L MgSO4 (Fisher Chemical, M65-500), 6.8 g/L NaCl (Fisher Chemical, S2711), 2.2 g/L NaHCO3 (Acros Organics, AC447102500), 0.14 g/L NaH2PO4-H2O (Fisher Chemical, S369-500), and 0.01 g/L Phenol red (Fisher Chemical, P74-10)) for 18 h at 37 °C. For glutamate treatment, cells were incubated in 100 μM glutamate (Sigma, G8415) and 10 μM glycine (Sigma-Aldrich, G5417) in EBSS for 30 min at 37 °C. Prior to glutamate treatment, cells were pre-treated with 1 μM Cyclosporin-A (CsA, Sigma-Aldrich, SML1018) and 10 μM Ru360 (Calbiochem, 557440) for 60 min. Following pre-treatment, cells were incubated with CsA and Ru360 concurrently with glutamate treatment for 30 min.

Oxygen-glucose deprivation and reoxygenation (OGD/R)

OGD was achieved utilizing an O_2 Control InVitro Glove Box (Coy Lab Products). The hypoxic chamber was maintained at 0.1% O_2 and 5% CO_2. OGD media, composed of 0.20 g/l $CaCl_2$ (Spectrum, CA138500GM), 0.4 g/l KCl (Fisher Chemical, P217-500), 0.097 g/l $MgSO_4$ (Fisher Chemical, M65-500), 6.8 g/l NaCl (Fisher Chemical, S2711), 2.2 $NaHCO_3$ (Acros Organics, AC447102500), 0.14 g/l NaH_2PO_4-H_2O (Fisher Chemical, S369-500, and 0.01 g/l Phenol red (Fisher Chemical, P74-10), was bubbled with 95% N_2/5% CO_2 inside of the of the hypoxic chamber for 60 min. Cells were transferred into the hypoxic chamber, washed 2× with OGD media, and then incubated with OGD media inside the hypoxic chamber for 150 min. After OGD, cells were removed from the hypoxic chamber, media was replaced with Neurobasal medium without antioxidants (complete neurobasal medium with B27-AO (Gibco, 10889038)), and incubated at 37 °C in 5% CO_2 for 6 h.

Cryostat sectioning

Mice were anesthetized with isoflurane then transcardially perfused with 10 mL of 1 × PBS, followed by 10 mL of 4% PFA in 1 × PBS. Brains were post-fixed overnight in 4% PFA at 4 °C, then cryoprotected in 25% sucrose in 1 × PBS. Brains were cut into 20 μm sections using

a cryostat (CM1860, Leica Microsystems), set at − 22 °C, cold mounted onto slides (Superfrost, Thermo Fisher Scientific), and stored at − 20 °C until staining.

Western blot

Cells were scraped in homogenization-A buffer, sonicated, and protein concentration was measured using the Bradford Plus Assay Reagent (ThermoFisher, PI23236). Polyacrylamide gels (10% 29:1 polyacrylamide/bisacrylamide (Fisher BioReagents, BP1408-1), 375 mM Tris pH 8.8 (Fisher BioReagents, BP152-1), 0.1% sodium dodecyl sulfate (SDS, Sigma, L3771), 0.1% ammonium persulfate (APS, Sigma, #A3678), and 0.1% TEMED (GE Healthcare, # 45-000-226)) were loaded with 10 μg of whole cell lysates and transferred to nitrocellulose membranes. Membranes were incubated with primary antibodies (1:1000 Mouse Anti-Dlp1/Drp1 in 2% milk (Clone 8, BD Transduction Laboratories, BD6111112); 1:1000 Mouse Anti-Opa1 in 2% BSA (BD Transduction Laboratories, BD612607); 1:10,000 Rabbit Anti-GAPDH in 2% BSA (14C10, Cell Signaling, 2118)) at 4 °C overnight. Membranes were then washed with Tris-Buffered Saline and 0.1% Tween (TBST, Fisher Scientific, BP337500) and incubated in secondary antibodies for 60 min at room temperature. Membranes were then washed 3 × with TBST for 5 min. The membranes were incubated in SuperSignal West Pico Plus Chemiluminescent Substrate (ThermoFisher, 34577), imaged utilizing a BioRad ChemiDoc XRS and imager, and finally quantified by densitometry using ImageJ.

Immunofluorescence

Cultured cells were fixed with 4% paraformaldehyde (ThermoFisher, 50980487) for 15 min at 37 °C. Coverslips were incubated in blocking solution (5% goat serum (Sigma, G9023) and 0.3% Triton-X100 (Acros Organics, 215682500) in PBS) for 60 min. Coverslips were then incubated in primary antibody solution (1:1000 Mouse Anti-ATPB (Abcam, ab14730), 1:200 Rabbit Anti-TOM20 (ProteinTech, 11802–1-AP), 1:1000 Chicken Anti-MAP2 (Abcam, ab5392), 1% BSA (Sigma, A9647) and 0.3% Triton-X100 in PBS) at 4 °C overnight. After primary incubation, coverslips were washed 3 × in PBS and incubated in secondary antibody solution (1:200 Anti-Mouse Alexa Fluor 488 (Invitrogen, A11029), 1:200 Anti-Rabbit Alexa Fluor 546 (Invitrogen, A10040), 1:200 Anti-Chicken Alexa Fluor 647 (Invitrogen, A21449), 1% BSA (Sigma, A9647) and 0.3% Triton-X100 in PBS) for 60 min. Following secondary incubation,

coverslips were washed 3 × with PBS and mounted on glass slides using Fluoroshield with DAPI (Sigma, F6057).

Tissue sections were permeabilized with 1% triton in 1 × PBS for 10 min and then 3% peroxide for 10 min. Sections were blocked using 2% goat serum/TBSGBA (Tris buffered saline, gelatin, bovine serum, azide) for 1 h. Primary antibody (1:100 Mouse Anti-ATPB, Abcam, ab14730) in blocking solution was incubated overnight at room temperature. Sections were washed with 1 × PBS, incubated with secondary antibody (1:100 Anti-Mouse Alexa Fluor 488 (Invitrogen, A11029) and DAPI (Sigma) for 3 h at room temperature and mounted with ProLong Glass mountant (Thermo Fisher Scientific).

Fluorescent microscopy

Cell culture Each coverslip was imaged using a Zeiss Axio Observer Z1 inverted microscope with LED illumination. For each coverslip, 8–10 image z-stacks (0.24 µm slices) were acquired at 63 × with oil immersion. Z-stacks were then deconvolved using the Zeiss Zen Pro regularized inverse filter method. Following, z-stacks were processed using Zeiss Zen Pro extended depth of focus wavelets method. Images were exported in TIFF format for post-processing.

Tissue sections Images were acquired on a Leica TCS SP8 Dmi8 STED Inverted Confocal microscope (Leica Wetzler, Germany) using Leica Application Suite X (LASX). Z-series of 5 µm were collected beginning at the top of the tissue section inward using the following parameters: 400 Hz, z step size:0.1 um, 2048 × 2048. After acquisition, image stacks were deconvolved with Huygens Professional version 19.04 (Scientific Volume Imaging, The Netherlands, http://svi.nl) using CMLE algorithm, with SNR:20 and 40 iterations. Z stacks were exported in TIFF format for post-processing.

Electron microscopy

Brains were fixed with 2.5% glutaraldehyde then embedded and stained with osmium tetroxide and imaged on a scanning block face scanning electron microscope19. Block-face scans of the sample are taken, followed by removal of a 70 nm section and subsequent SEM image the next z-plane. This process is repeated on average 400 to 500 times, generating z-stacks of SEM data at 70 nm intervals.

Image processing and segmentation

Immunofluorescence post-processing was performed in FIJI (213). Images collected from in vitro experiments were imported as merged images of ATP synthase and TOM20 signal. Z series of mouse cerebral tissue were unstacked and imported into FIJI as individual images of ATP synthase signal. The following steps were performed using FIJI's batch processing feature. Background noise was removed using a rolling ball radius of 10 pixels. Images were filtered via Unsharp Mask with a radius of 1 pixel and mask weight of 0.60. Enhancement of local contrast was performed using Contrast Limited Adaptive Histogram Equalization (CLAHE) with 256 histogram bins (244). A median filter was then applied to each image with a radius of 2 pixels. Mitochondria were segmented using Trainable Weka Segmentation (240). The segmentation classifier model was trained using hand identified mitochondria from processed images, positive for ATP Synthase and/or TOM20 signal. Segmentation output images were converted to 8-bit binary images and the known scale was set. For the identification of mitochondrial objects in 2D, the FIJI Particle Analyzer plug-in was run with a minimum object size of 0.30 um. Measurements from identified objects were then expanded using the Extended Geometric Descriptions macro (245).

Electron microscopy Images were imported into FIJI software and 5 × compressed via bilinear interpolation. Mitochondrial objects were segmented from downsized images using Trainable Weka Segmentation (240). Output images were converted to 8-bit binary.

3D object mapping and measurement

Segmented binary images from tissue immunofluorescence and electron microscopy were morphologically eroded using MorphoLibJ Morphological Filters plug-in (239). Individual images were then re-assembled into z stacks and 3D objects were identified using the MorphoLibJ Connected Components Labeling plug-in at a connectivity setting of 655. Resulting connected objects were measured with the 3D ROI Manager (246).

Machine learning classification

Machine learning-based classification of mitochondrial objects was performed in R computing language using the R Caret package (214,215). Rstudio software (Boston, MA) was used for all R computation. The following procedures were utilized for the development of all classification models described. The measurements of classified mitochondrial objects, along with

their classification, were imported into Rstudio as the train/test set. This data set was then split into the training (80%) and test (20%) sets using the createDataPartition function. A random forest algorithm ("rf") was trained by the training set with 25 repetitions. The test set was then run through the model for the assessment of accuracy. Confusion matrices and principal component analyses were produced to assess the performance of the models.

After model construction, data from in vitro experiments was imported into Rstudio and run through the trained model using the predict function. Predicted morphological phenotypes for each mitochondrial object were then exported along with the original measurements as a csv file. Data was then compiled and organized in Microsoft Excel (Redmond, WA) to compute the percent mitochondrial area belonging to each morphology in a given image/condition. R functions written for model training and morphological predictions are available in our GitHub repository (https://github.com/sanderson-lab/mitomorphology).

Statistical analysis

Statistical analyses were performed in GraphPad Prism 8 (GraphPad Software, San Diego, CA). For comparisons of two discrete groups, one-way ANOVAs were performed, followed by post-hoc t-tests. For comparisons of more than two groups, two-way ANOVAs were performed with post-hoc comparisons made by Tukey's test corrected for multiple comparisons. Tests with $p < .05$ were considered statistically significant. The number of biological replicates is indicated by n, unless otherwise noted.

2.5 Figures

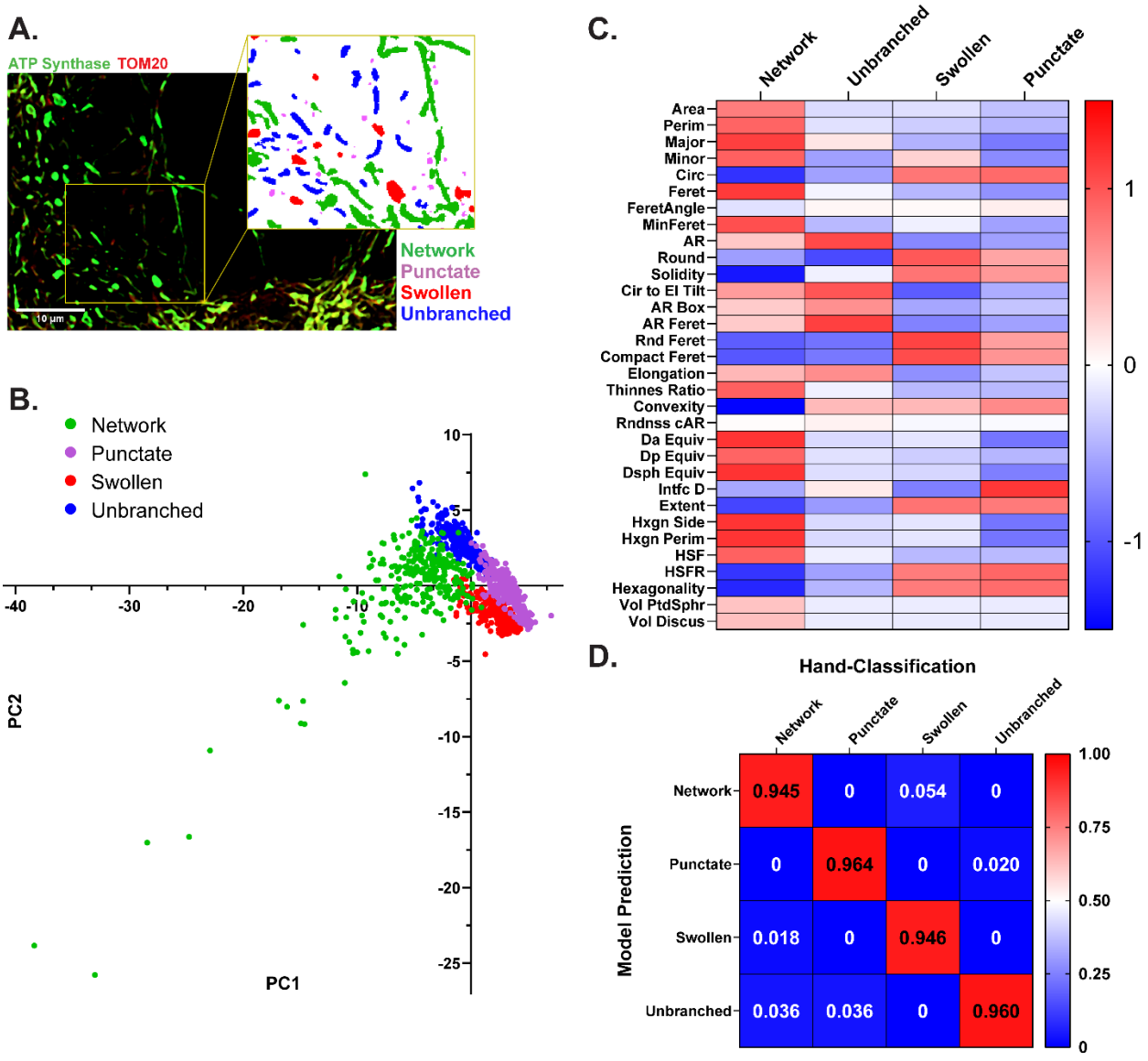

Figure 2-1. Identification of distinct mitochondrial morphologies in primary neurons

(A) Representative immunofluorescent image of mitochondria labeled for ATP synthase (green) and TOM20 (red). Insert: mitochondrial objects segmented and color coded by classified morphology. (B) Principal component analysis (PCA) of hand-classified mitochondrial objects in the training and test sets combined. Individual objects are color coded by morphology (n = 1091 mitochondrial objects). (C) Heatmap displaying the scaled 32 size and shape measurements by morphology. (D) Confusion matrix displaying the results of model evaluation using the hand-classified test set (217 objects).

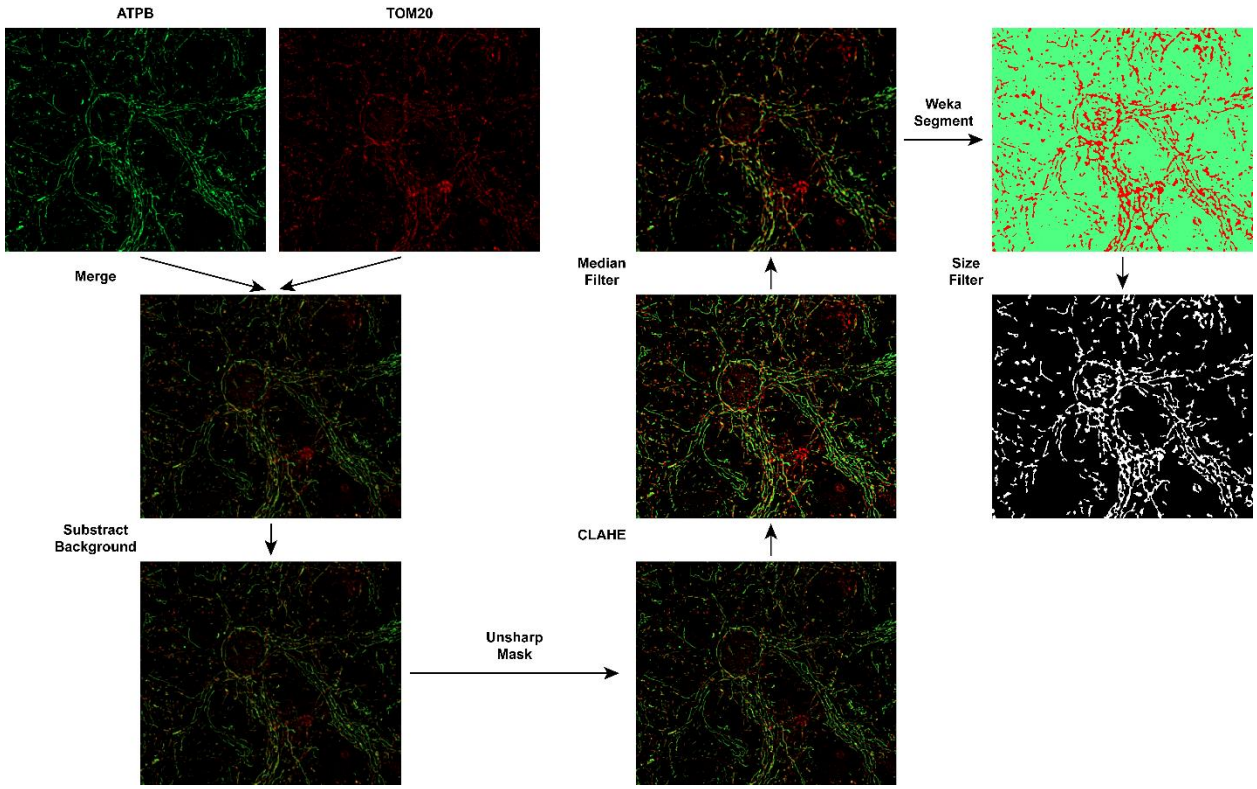

Figure 2-2. Processing workflow for the segmentation of mitochondrial objects

Representative ATPB and TOM20 immunofluorescent images were run through the batch processing workflow and images are shown at each processing step. The brightness and contrast of raw ATB and TOM20 images were enhanced for the readability of this figure.

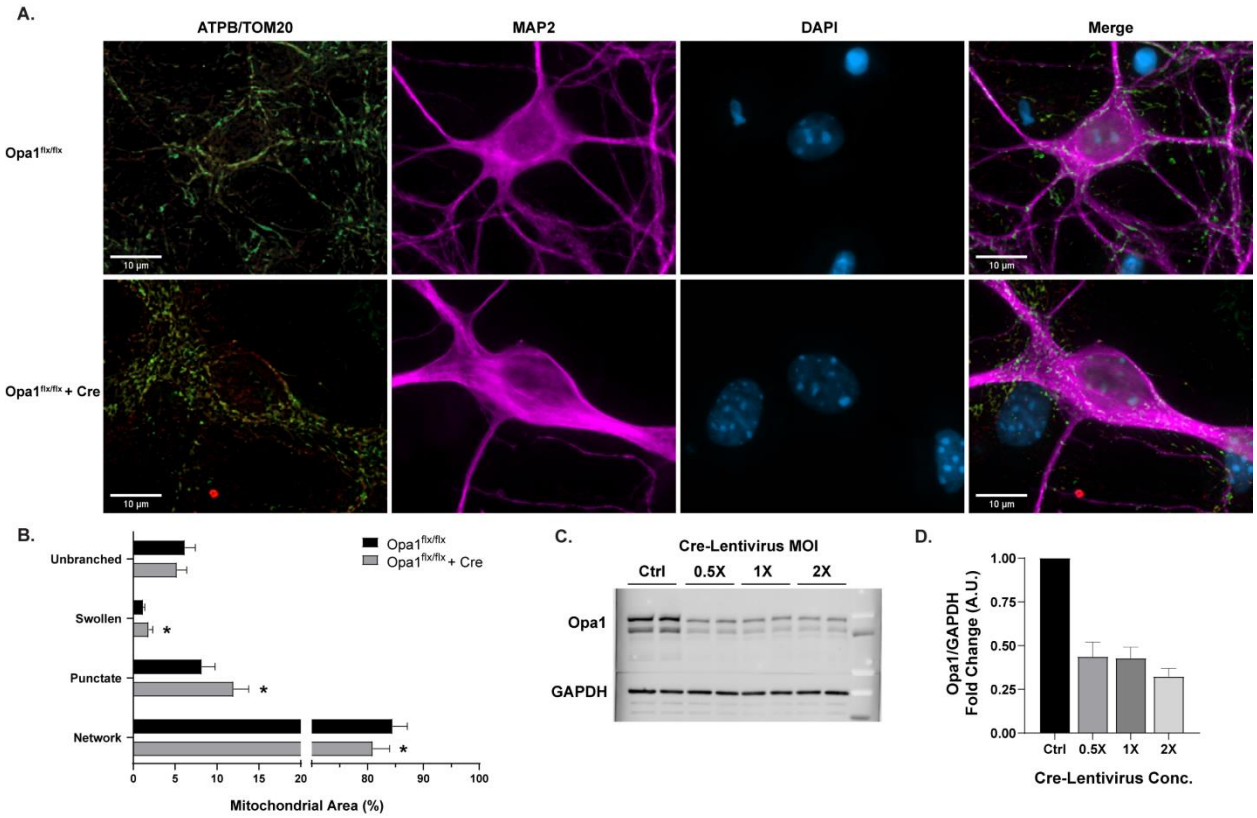

Figure 2-3. Morphological analysis of mitochondria in Opa1 conditional knockout

(A) Representative images of primary Opa1$^{flx/flx}$ neurons (top) and Opa1$^{flx/flx}$ neurons with Cre (bottom). Panels (from left to right): ATP synthase (green) and TOM20 (red) merged, MAP2 (magenta), DAPI (blue), all channels merged. Scale bars = 10 µm. (B) Percentage of mitochondrial area per morphology in Opa1$^{flx/flx}$ cells (black) and Opa1flx/flx cells with Cre (gray). Mean ± SD (n = 9 per group). * indicates $p < .05$. (C) Representative Western blot displaying Opa1 and GAPDH protein levels across Cre-Lentivirus concentrations. (D) Western blot quantification of Opa1 protein levels after Cre-Lentivirus treatment (n = 3). For all Opa1 cKO experiments, 1 × MOI Cre-Lentivirus was used.

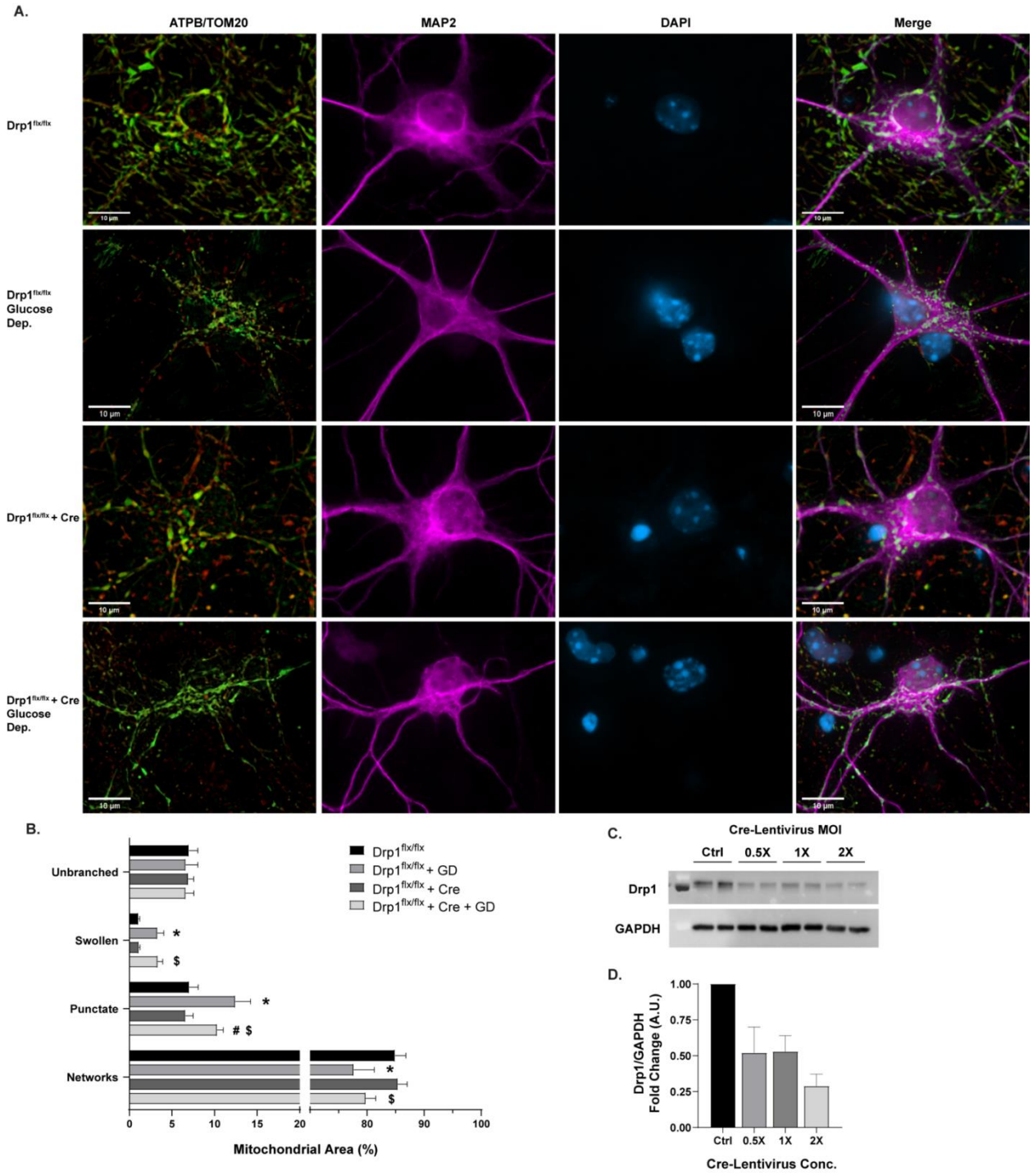

Figure 2-4. Morphological analysis of mitochondria in Drp1 conditional knockout (cKO) and glucose deprivation (GD)

(A) Representative images of primary Drp1$^{flx/flx}$ neurons. Rows (top to bottom): control Drp1$^{flx/flx}$, Drp1$^{flx/flx}$ after 18 hr GD, Drp1$^{flx/flx}$ with Cre, Drp1$^{flx/flx}$ with Cre after 18 hr GD. Untreated control groups are shown on rows 1 and 3, 18 h GD groups are shown on rows 2 and 4. Panels (from left to right): ATP synthase (green) and TOM20 (red) merged, MAP2 (magenta),

DAPI (blue), all channels merged. Scale bars = 10 μm. (B) Percentage of mitochondrial area per morphology in Drp1 cKO and GD experiments. Mean ± SD (n = 5–8 per group). * indicates $p < .05$ versus $Drp1^{flx/flx}$. # indicates $p < .05$ versus $Drp1^{flx/flx}$ + GD. $ indicates $p < .05$ versus $Drp1^{flx/flx}$ + Cre. (C) Representative Western blot displaying Opa1 and GAPDH protein levels across Cre-Lentivirus concentrations. (D) Western blot quantification of Drp1 protein levels after Cre-Lentivirus treatment (n = 3–4). For all Drp1 cKO experiments, 2 × MOI Cre-Lentivirus was used.

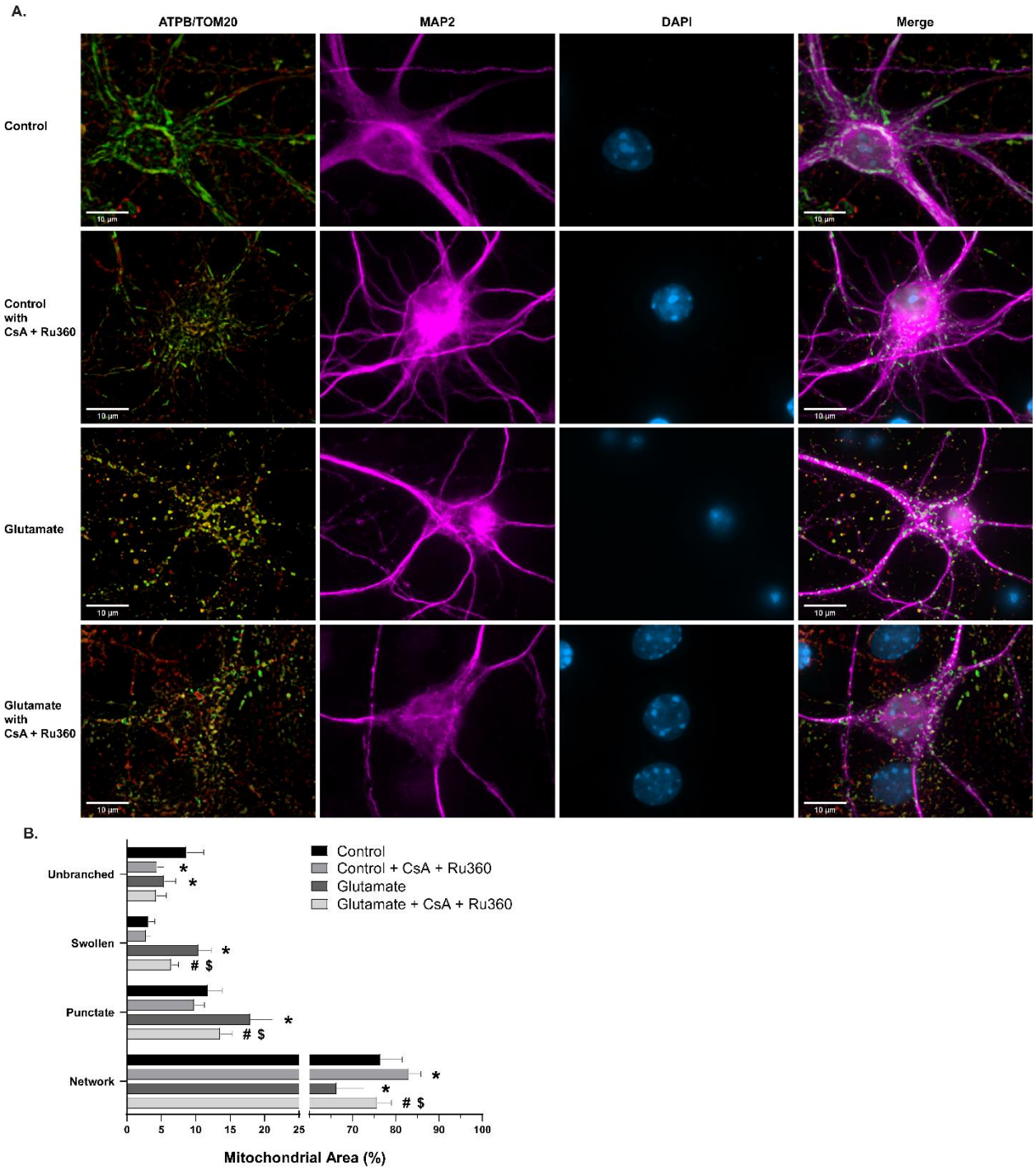

Figure 2-5. Morphological analysis of mitochondria in glutamate and cyclosporin A (CsA) + Ru360 experiments

(A) Representative images of primary cortical neurons. Rows (top to bottom): vehicle-treated control group, control cells treated with CsA + Ru360 only, vehicle-treated group with 30 min 100 µm glutamate exposure, glutamate challenged group pre-treated and co-incubated with CsA + Ru360 Panels (from left to right): ATP synthase (green) and TOM20 (red) merged, MAP2

(magenta), DAPI (blue), all channels merged. Scale bars = 10 µm. (B) Percentage of mitochondrial area per morphology in glutamate and CsA + Ru360 experiments. Mean ± SD (n = 6–8 per group). * indicates $p < .05$ versus Control. # indicates $p < .05$ versus Control + CsA + Ru360. $ indicates $p < .05$ versus Glutamate.

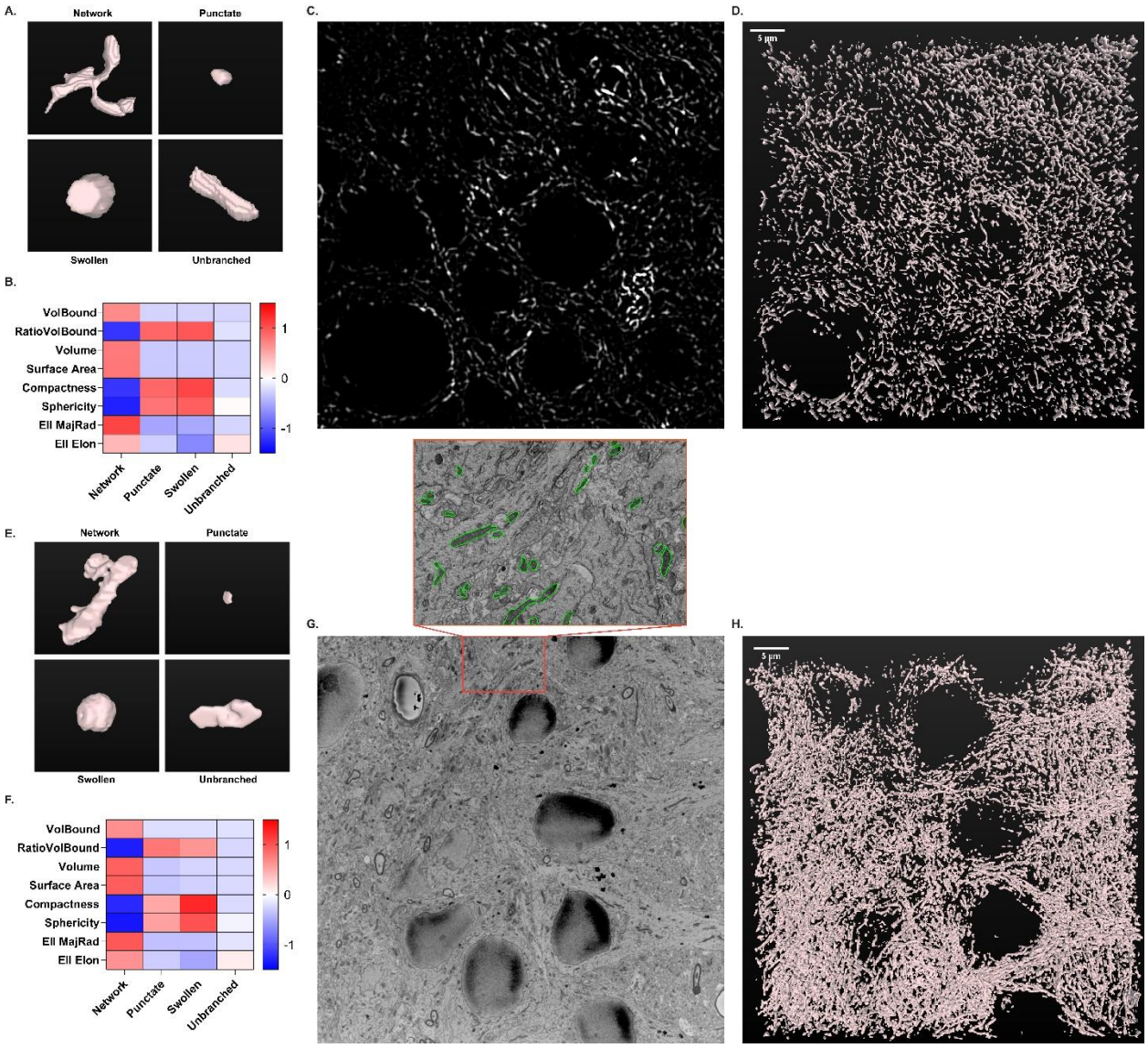

Figure 2-6. 3D morphological classification of mitochondria using confocal and electron microscopy

(A) Representative 3D renderings of individual mitochondrial objects from mouse brain tissue immuno-labeled for ATP synthase and imaged using confocal microscopy. (B) Heatmap displaying the scaled 8 size and shape measurements by morphology for confocal microscopy. (C) Representative confocal image of ATP synthase immunofluorescence from mouse hippocampus. (D) 3D rendering of mitochondria from the full z-series (50 slices, 5 µm) of the image shown in (C), acquired via confocal microscopy. (E) Representative 3D renderings of individual mitochondrial objects from rat brain tissue acquired via serial block-face scanning electron microscopy (SBF-SEM). (F) Heatmap displaying the scaled 8 size and shape measurements by morphology for SBF-SEM. (G) Representative single-plane image from SBF-SEM z-series. Insert: Enlarged area of representative image with mitochondria traced (green).

(H) 3D rendering of mitochondria from the full z-series (100 slices, 7 μm) of the image shown in (G), acquired via SBF-SEM.

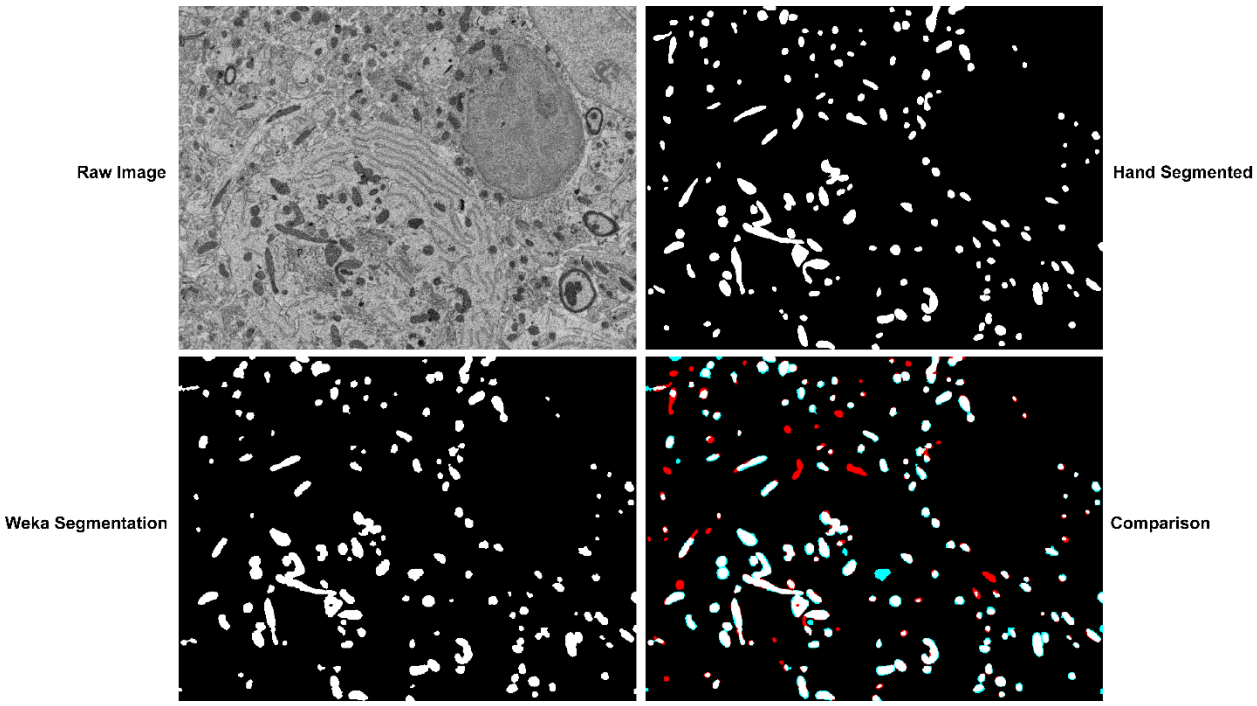

Figure 2-7. Machine learning-based automated segmentation of SBF-SEM images

The trainable Weka segmentation plug-in was utilized to segment mitochondria from SBF-SEM images in an automated manner in FIJI. Upper Left: representative raw SBF-SEM image; Upper Right: mitochondrial objects hand segmented by an experienced reviewer; Lower Left: mitochondrial objects segmented via automated Weka segmentation; Lower right: comparison of hand segmented and Weka segmented binary object maps, false positive signal is shown in blue, false negative signal is shown in red. Weka segmentation was performed using a random forest machine learning model (100 decision tree, 8 random features per tree) with a training error of 0.525%. Similarity between hand segmented and Weka segmented object maps was quantified by Jaccard Index (0.575 ± 0.067) and Dice Coefficient (0.7277 ± 0.055) for a set of randomly selected SBF-SEM images (n=9).

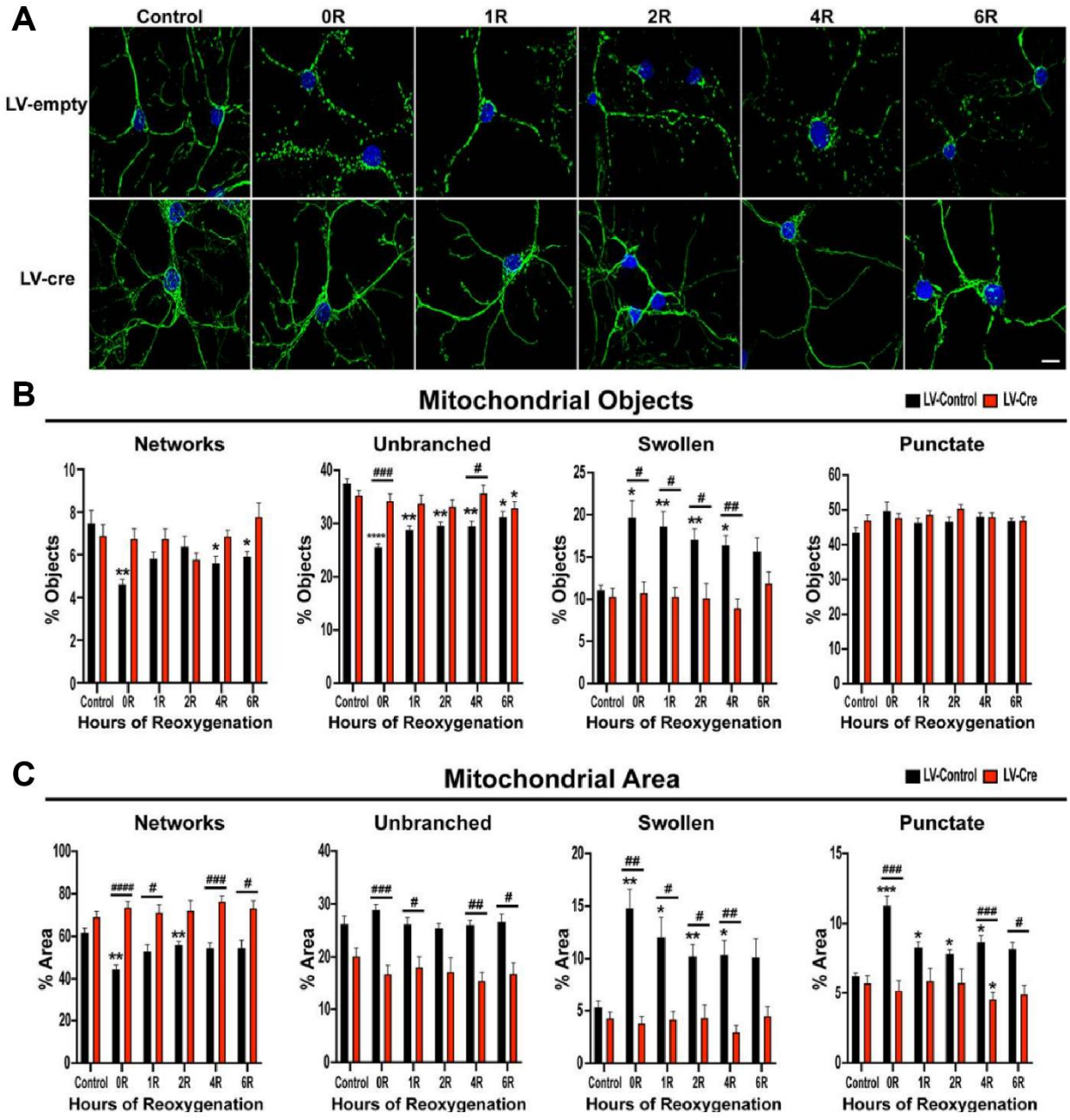

Figure 2-8. Mitochondrial morphology during OGD/R

(A) Representative images of Drp1$^{flx/flx}$ primary cortical neurons infected with either LV-EF1a-empty or LV-EF1a-Cre, and subjected to OGD/R. (B) Individual comparisons of percent mitochondrial objects for each morphology over OGD/R. (C) Individual comparisons of percent mitochondrial area for each morphology over OGD/R. Two-way ANOVA was used to detect differences across time and between conditions. Multiple comparisons across time were assessed by comparing the means of each time point with the mean of the control and were calculated using Dunnett's post-hoc analysis. Multiple comparisons between conditions were computed using Sidak's post-hoc analysis. *$p < 0.05$; **$p < 0.01$; ***$p < 0.001$; ****$p < 0.0001$ across time,

#p < 0.05; ##p < 0.01; ###p < 0.001; ####p < 0.0001 between condition, n = 8 biological replicates per group. Scale bar = 10 μm.

Chapter III: Mitochondrial Dynamics and Quality Control Regulate Proteostasis in Neuronal Ischemia-Reperfusion Injury [2]

3.1 Introduction

Mitochondria are highly dynamic organelles that produce vital energy to ensure continued cellular homeostasis (42). Aside from energy producing functions, mitochondria contain their own proteome, genome, and molecular machinery. Additionally, mitochondria drive and contribute to a varying list of essential cellular functions including redox homeostasis, Ca^{2+} buffering, amino acid metabolism, and stress signaling (17,34,247). For these reasons maintaining mitochondrial function is critical for cell survival. This is especially true for post-mitotic cells and tissues, such as neurons and cardiomyocytes, where mitochondrial proteins can persist and function for extended periods of time (days to months) (248,249). The dynamic nature and oxidative environment of the mitochondria make it a susceptible target for injury and stress (42,250,251). It is therefore imperative to understand the factors that contribute to mitochondrial dysfunction and its consequences.

Cerebral ischemia/reperfusion (I/R) injuries, including stroke and cardiac arrest, continue to be leading causes of death and disability (2,252). Return of normal blood flow and oxygenation during reperfusion constitutes a secondary phase of cellular stress despite returning oxygen and other nutrients (16,253). A primary component of reperfusion stress is mitochondrial dysfunction. During the ischemic/hypoxic phase, mitochondria are deprived of oxygen and therefore oxidative phosphorylation is halted at the terminal electron acceptor cytochrome *c* oxidase (COX) (34,254). Several factors including energy deprivation and calcium flux are responsible for priming COX and other enzymes for increased activity when oxygen becomes available (254-257). Upon reperfusion, oxygen returns and oxidative phosphorylation continues on at an elevated rate, whilst also increasing reactive oxygen species (ROS) production. An oxidative burst of ROS production

[2] This chapter is composed of the submitted manuscript: "Fogo GM, Raghunayakula S, Emaus KJ, Torres Torres FJ, Shangguan G, Wider JM, Hüttemann M, Sanderson TH. Mitochondrial dynamics and quality control regulate proteostasis in neuronal ischemia-reperfusion. *Submitted*". I performed all detailed experiments.

occurs rapidly upon reperfusion (34,90,258,259). This mechanism, among other insults related to prolonged hypoxia, has detrimental consequences for mitochondrial protein stability and functionality. Protein oxidation, lipid peroxidation, and protein complex instability are critical factors that contribute to loss of efficient energy production and stress signaling from mitochondria (260-264). Due to the necessity of mitochondrial function to cell survival, mitochondrial dysfunction has been recognized as a leading therapeutic target for limiting secondary injury in cerebral I/R insults (265,266).

Maintenance of the mitochondrial proteome, and resultant mitochondrial homeostasis, is mediated by both mitophagy and intramitochondrial proteostasis (42,103). Mitophagy, the autophagic degradation of mitochondria, includes engulfment of whole organelles as well as selective removal of mitochondrial components via mitochondrial derived vesicles (107,108). The best characterized form of mitophagy in neurons is the stress-responsive PINK1-Parkin pathway (42,107). Briefly, in dysfunctional mitochondria with low mitochondrial membrane potential, import of the kinase PINK1 to mitochondria is halted, leading to phosphorylation and recruitment of downstream mitophagy outside the mitochondria, including Parkin. Parkin activation by phosphorylation leads to poly-ubiquitination of the mitochondria and recruitment of phagophores for eventual degradation. Mitophagy has long been the focal point of research into mitochondrial quality control and its relation to injury and disease. However, mitochondria also have the ability to remodel their proteome from within via intramitochondrial proteostasis. Mitochondria are home to their own diverse set of proteases and peptidases that work within the organelle to process, cleave, and degrade their own proteins and protein complexes (103,135). These mitochondrial proteases serve in distinct roles, often dictated by the compartment in which they reside. Proteases localized to the intermembrane space and inner mitochondrial membrane serve to regulate functions related to protein import and protein complex assembly (136-140). In contrast, matrix-localized proteases play a larger role in protein maintenance and degradation. The two dominant matrix proteases, LonP1 and CLPP, are critical for the degradation of oxidized/misfolded proteins and turnover of damaged components of the electron transport chain (141-144). Despite its importance, the intramitochondrial proteostatic response to I/R injury is not well understood.

In this study, we aimed to characterize the temporal pattern of mitochondrial protein turnover and investigate the mechanisms that are initiated in response to *in vitro* I/R injury in

primary neurons. We hypothesized that mitochondria activate critical proteostatic mechanisms in response to injury, likely mediated by the matrix proteases LonP1 and CLPP. Utilizing the fluorescent MitoTimer reporter, we assessed protein turnover throughout oxygen-glucose deprivation and reoxygenation (OGD/R, an *in vitro* model of I/R injury) (267). Our findings highlight an important time point during reoxygenation in which LonP1-dependent proteolytic activity is upregulated. Intriguingly, protein turnover is additionally influenced by perturbations in mitochondrial dynamics and mitophagy. These results demonstrate the involvement of intramitochondrial and mitophagic protein turnover in neuronal I/R injury and present a possible therapeutic target to rescue mitochondrial homeostasis.

3.2 Results

3.2.1 Reoxygenation induces a peak in MitoTimer protein turnover

To evaluate the temporal pattern of mitochondrial protein turnover, we conditionally expressed the fluorescent probe MitoTimer in mouse primary cortical neurons exposed to oxygen-glucose deprivation and subsequent reoxygenation (OGD/R). MitoTimer is a designer fluorescent probe used to track protein dynamics in the mitochondrial matrix (267). When newly synthesized, MitoTimer is trafficked to the mitochondrial matrix and fluoresces green. Over time, the protein converts from green to red fluorescence (Fig. 3-1A). This “aging” process is sensitive to environmental factors such as temperature and oxidation. The ratio of red/green MitoTimer signal is an indicator of protein age within mitochondria. Therefore, we visually tracked the abundance of green (new) MitoTimer and red (old) MitoTimer fluorescence, as well as the red/green ratio, over time in OGD/R. For neuron-specific expression of MitoTimer, Cre recombinase under the control of the human synapsin promoter (AAV8-hSyn-Cre) was virally transduced to neurons isolated from conditional MitoTimer mice (268) (Fig. 3-1B-D). At basal culture conditions, MitoTimer presented heterogeneous populations of mitochondria within single neurons and displayed differences between individual neurons (Fig. 3-1E).

Mouse primary cortical neurons were exposed to 90 min of OGD and up to 6 hr of reoxygenation at day-in-vitro (DIV)14, 7 days following viral transduction (Fig. 3-2A). Cells were fixed at the conclusion of OGD (0hR) or at varying points of reoxygenation (1, 2, 4, 6hR). MitoTimer green and red signals were imaged at each time point and mitochondrial protein turnover was assessed by the MitoTimer red/green ratio. Variance in MitoTimer ratios between

cells and individual mitochondria were high at control conditions, with highly filamentous mitochondrial morphology (Fig. 3-2B). As expected, OGD induced widespread mitochondrial fragmentation, however, MitoTimer ratios remained relatively unchanged (Fig. 3-2B,C). Predominating evidence in the field suggests that the first moments of reoxygenation are the epicenter of reactive oxygen species (ROS) production (34,258), therefore we expected dramatic shifts in protein dynamics at this time. Surprisingly, baseline levels of MitoTimer ratio persisted through early reoxygenation (1hR). In fact, a decrease in the MitoTimer ratio was observed at 2hR (Fig. 3-2B,C). Although the MitoTimer green fluorescence intensity consistently increased with reoxygenation, we observed a decrease in MitoTimer red intensity at the corresponding 2hR. This pattern suggests that mitochondrial protein is continually being synthesized and imported to mitochondria throughout early reoxygenation, and this is contrasted with an increase in the turnover of older (red) MitoTimer proteins. The later stages of reoxygenation present variable trajectories of MitoTimer protein dynamics, wherein cells either continue to import new protein or slow both import and proteostasis. These findings define a temporal pattern of intramitochondrial protein dynamics and identify a novel critical event in the mitochondrial response to injury.

3.2.2 LonP1 activity, but not expression, is increased during reoxygenation

The selective elimination of old (red), but not new (green), MitoTimer protein observed at 2hR suggested that altered intramitochondrial proteostasis may be responsible, rather than large scale mitophagic turnover of whole organelles. MitoTimer was designed to be targeted to the mitochondrial matrix, and has previously been shown to be sensitive to degradation by matrix proteases (269). We first assessed protein expression levels of critical mitochondrial proteases localized to the mitochondrial matrix (LonP1, CLPP) and inner membrane (AFG3L2, Oma1, Yme1L) throughout the OGD/R paradigm. Interestingly, we did not observe any changes in protease protein levels by Western blot (Fig. 3-3).

Protein expression and activity are not always correlated, especially during acute responses to stress; we therefore assayed mitochondrial protease activity. Crude mitochondrial isolation by differential centrifugation was performed in primary neurons at control conditions and at 2 hr reoxygenation. Protease activity was evaluated by FITC-casein proteolysis assay, in which mitochondrial lysates were fit to a standard activity curve of increasing amounts of TPCK Trypsin. We found that mitochondrial protease activity was indeed increased at 2hR and this increase was

ameliorated in the presence of CDDO-Me (Fig. 3-4A), a specific inhibitor for the matrix protease LonP1 (270,271). This finding suggests that an increase in activity, but not protein levels, of LonP1 is responsible for the proteostatic response at 2hR, corroborating previous findings that LonP1 can degrade MitoTimer protein (269). Interestingly, Western blot analysis of other known LonP1 substrates, TFAM and NDUFS1, did not demonstrate changes in levels corresponding to increased LonP1 activity at 2hR (Fig. 3-5). Similarly, there were no significant changes in any electron transport chain complexes (Fig. 3-5). Therefore, we performed the MitoTimer analysis with CDDO-Me treatment during reoxygenation to confirm LonP1 is responsible for the observed effects. CDDO-Me (0.5μM) treatment at the onset of reoxygenation inhibited the reduction in red MitoTimer fluorescence at 2hR (Fig. 3-4B, C). Together, these results identify that LonP1 activity is necessary for increased mitochondrial protein turnover during reoxygenation.

3.2.3 Parkin mediates basal and injury-induced protein turnover

To probe the influence of mitophagy on mitochondrial protein turnover, we analyzed MitoTimer protein dynamics in neurons lacking Parkin, an ubiquitin ligase crucial for classical mitophagy (42). Primary neurons were isolated from MitoTimer/Parkin KO (Parkin$^{-/-}$) mice and exposed to the same OGD/R paradigm described above. Parkin KO neurons displayed high MitoTimer fluorescence ratios with elevated levels of red MitoTimer and decreased green MitoTimer fluorescence, compared to WT cells (Fig. 3-6A,B). The MitoTimer ratio remained unchanged compared to control throughout reoxygenation as both green and red fluorescence increased over time (Fig. 3-6B). We did not observe a decrease in the red/green ratio or amount of red MitoTimer at 2hR (Fig. 3-6A, B). These results identify mitophagy, in addition to proteolysis, as a critical mediator of mitochondrial protein turnover at both basal and stress conditions.

3.2.4 Mitochondrial dynamics proteins Opa1 and Drp1 differentially effect protein turnover

Mitochondria are highly dynamic organelles that balance the forces of fusion and fission to maintain homeostasis and ensure proper energy production. The processes of fusion and fission are heavily intertwined with other critical mitochondrial pathways including mitophagy, organelle-to-organelle contact sites, and oxidative phosphorylation (42,47,272). We therefore hypothesized that mitochondrial dynamics could influence intramitochondrial proteostasis. To assess the effects of fission inhibition on protein turnover, we expressed MitoTimer in neurons with conditional knockout (cKO) of the key fission protein Drp1 (Fig. 3-7A) (242). Drp1 cKO cells presented with

large round hyperfused mitochondria at baseline conditions with similar MitoTimer ratios to wild-type (WT) controls (Fig. 3-7B,C). Upon injury, Drp1 cKO cells did not increase protein turnover at 2hR, but rather the MitoTimer red/green ratio gradually increased over time in OGD/R (Fig. 3-7B,C) due to the increase of red MitoTimer signal (Fig. 3-8). The striking divergence of Drp1 cKO cells from the WT pattern suggests that maintenance of fission is important for mitochondrial protein turnover.

The process of mitochondrial fusion is regulated by Mfn1/2 at the outer membrane and Opa1 at the inner membrane (42,47,243). To perturb mitochondrial fusion, we generated neuron-specific conditional knockouts of Opa1 (Fig. 3-7D). Contrary to Drp1 cKO, Opa1 cKO cells presented significantly different MitoTimer ratios at baseline conditions. Opa1 cKO cells heavily favored green MitoTimer with greatly reduced red MitoTimer fluorescence, suggesting an upregulated level of protein turnover even at baseline conditions (Fig. 3-7E; Fig. 3-8). This phenotype persisted throughout the OGD/R paradigm (Fig. 3-7F). To probe for potentially upregulated proteases, we assayed matrix and inner membrane proteases in WT and Opa1 cKO cells by Western blot. We found that Opa1 cKO cells had dramatically increased levels of Oma1 protease expression at baseline conditions (Fig. 3-9). Together these data suggest that loss of Opa1 upregulates Oma1 protein levels and drives intramitochondrial proteostasis.

3.3 Discussion

Mitochondrial homeostasis is vital for efficient energy production and cell survival. Disruption of this homeostasis during I/R is thought to be a key driver of secondary injury with increasing ROS levels and perturbed bioenergetics. Mitochondria possess their own unique set of proteases/peptidases that work to maintain critical functions, clear damaged proteins, and initiate stress signals. The aim of this study was to interrogate the involvement of this mitochondrial proteostasis system in a model of neuronal I/R injury. The conclusions of this study are that mitochondria upregulate protease activity and protein turnover during reoxygenation, processes driven by LonP1 and Parkin-mediated mitophagy. Intriguingly, this response is intertwined with the pathways of mitochondrial dynamics, wherein mitochondrial fission and fusion appear to differentially regulate mitochondrial protein turnover.

Mitochondrial Protein Turnover in I/R injury

The turnover and remodeling of the mitochondrial proteome is driven by two independent but likely cooperative mechanisms: autophagy-dependent degradation and protease-dependent proteolysis. The autophagic degradation of mitochondria and their contents, termed mitophagy, is an elegantly coordinated system that involves the sequestration of mitochondria or mitochondrial-derived vesicles and subsequent degradation by lysosomes (42,108). Mitophagy has long been of substantial interest in the study of neuronal I/R. During I/R injury, classical pathways of mitophagy including PINK1/Parkin and BNIP3 are activated and increase mitophagic flux (86,153,159,164,273-275). However, several studies have highlighted that the traditional model of macroautophagic engulfment of mitochondria may not be the leading mechanism of protein turnover in neurons at basal conditions (132-134). Further, only a subset of mitochondrial proteins are degraded through autophagy-dependent pathways (132,134), therefore suggesting that intramitochondrial proteolysis may be a more critical process than previously thought.

Proteostasis has been demonstrated to mediate and modulate mitochondrial stress responses in hypoxic/ischemic injuries. For example, mitochondrial proteases in response to hypoxia degrade misfolded and oxidized proteins, as well as electron transport chain (ETC) components (175-178). Induction of the proteostatic system is believed to be beneficial to mitochondrial function and cell survival, including its upregulation in the mitochondrial unfolded protein response (mtUPR) (276-278). The mtUPR, although not extensively demonstrated in mammalian systems, includes the increased synthesis of mitochondrial chaperones and proteases for protection against various mitochondrial stresses (279). The potential protective effects of mitochondrial proteostasis, and its relatively unknown involvement in neuronal injury, warrant further study.

Intramitochondrial protein turnover in the context of I/R is not well understood and was therefore the focus of our study. We encoded conditional expression of the fluorescent protein MitoTimer for the temporal tracking of mitochondrial protein turnover. MitoTimer, a variant of the designer protein Timer, fluoresces green when newly synthesized and trafficked to the mitochondrial matrix (267,268,280). Upon oxidation over time, the protein irreversibly switches to a red fluorescence. This system allows for visual tracking of protein dynamics. Importantly, MitoTimer has little responsiveness to acute changes in mitochondrial matrix pH and is stable for long periods of time in various cell types, including neurons (83). The degradation of red, or

"aged", MitoTimer protein is dependent on both forms of mitochondrial quality control: mitophagy and proteolysis. Within mitochondria, knockdown experiments of the matrix proteases LonP1 and CLPP demonstrate they are the predominant proteases responsible for red MitoTimer degradation (269). These findings align with the classical thinking that LonP1 and CLPP survey the matrix and preferentially degrade oxidized proteins (144). Our study demonstrates novel findings of acute changes in mitochondrial protein turnover in response to OGD/R in neurons. Specifically, at 2 hours of reoxygenation, there is a significant loss of red MitoTimer protein, a sign of increased protein degradation. We found a corresponding increase in LonP1-dependent protease activity at this timepoint, and red MitoTimer protein degradation required LonP1 activity. Following 2 hours reoxygenation, variable trajectories arise in which some cells remain at low red/green MitoTimer ratios, while others drift towards oxidized protein accumulation. Long-term MitoTimer red accumulation in nerve tissue has also been reported in a hindlimb I/R model (268). The multimodal distribution of proteostasis may be dependent on programmed cell death, as this time window has been suggested as a critical decision point for cell fate (34,265,273). The amount of green MitoTimer remains relatively stable throughout the injury paradigm, with a trending increase over time. It is important to note that expression of MitoTimer in the cassette used is under the control of the β-actin promoter (268). Therefore, accumulation of green MitoTimer protein is not a reliable measure of mitochondrial biogenesis, but could be interpreted as the level of current protein translation and mitochondrial import.

Neuronal mitophagy has been extensively studied in numerous contexts, including Parkinson's disease, Alzheimer's disease, and I/R injury (131,158,281,282). The classical PINK1-Parkin pathway of mitophagy has long been considered to be the dominant stress-response of neuronal mitochondria. To assess the influence of this pathway in our I/R paradigm, we measured MitoTimer protein dynamics in Parkin KO neurons. We found that Parkin KO cells had dramatically increased levels of red MitoTimer protein throughout OGD/R compared to WT cells. The abundance of red MitoTimer protein increased throughout reoxygenation, without a significant peak in degradation. These results identify mitophagy as a key regulator of the observed protein dynamics in response to OGD/R. Despite evidence that classical mitophagy may not be highly active at basal conditions in neurons (132-134, 283), we found that Parkin KO significantly altered the balance of new and old MitoTimer protein under control conditions. Our findings of

mitophagic activity in neuronal OGD/R add to an abundance of evidence in the field, and additionally highlight its importance in mitochondrial protein turnover.

An important note regarding our findings is that MitoTimer is a non-native protein and interpretations of our data should reflect that limitation. MitoTimer protein dynamics likely model those of similar native proteins, such as other soluble oxidizable matrix proteins. Western blot analysis of key subunits of each complex in the ETC did not reveal any macro-level trends in protein levels during OGD/R. Fundamental differences between these membrane-bound and complex-embedded proteins and MitoTimer likely explain the contrasting observations. Additionally, protein levels are dependent on the opposing forces of synthesis and degradation. MitoTimer green and red signals allow for the disentanglement of these processes, whereas classical Western blot techniques do not.

Role of LonP1 in Mitochondrial Stress

To better understand the causal mechanism of increased protein turnover at 2 hours reoxygenation after OGD, protease activity was assayed. Protease activity from crude mitochondrial fractions displayed significantly higher activity than normoxic control samples. Treatment of cells for 2 hours (at onset of reperfusion) with the LonP1 inhibitor CDDO-Me ameliorated this increase and in fact decreased both control and 2hR protease activity to equal levels. These results were followed up by treating MitoTimer neurons with CDDO-Me. LonP1 inhibition by CDDO-Me resulted in a perturbed degradation of red MitoTimer during reoxygenation. Together, these results point to LonP1 being the causal protease degrading oxidized MitoTimer protein. Interestingly, protein levels of the known LonP1 substrates TFAM and NDUFS1 (complex I peripheral arm subunit) were not significantly altered during the course of OGD/R (284-286). These contrasting observations suggest that LonP1 increases activity only for specific substrates (e.g. oxidized soluble proteins), as others have shown but was not directly tested in this study (144,175,287). LonP1 has also been implicated in the turnover of cytochrome *c* oxidase subunits during I/R, with preference towards phosphorylated proteins (288). Although LonP1 was found to be more active following reoxygenation, it is still unclear if this activity is beneficial or detrimental. Clearance of oxidized, misfolded, or damaged proteins would generally be considered pro-survival, but the greater discussion of its activation during stress is debated. For example, I/R studies in cardiomyocytes have demonstrated contrasting conclusions about LonP1,

as either pro- or anti-apoptotic (286,289). Due to LonP1's diverse roles in mitochondria, it is likely that a balance of activity or substrate-specific activity is required. This is similar to the stress response pathways that LonP1 partially mediates, including stress granule formation, the mitochondrial unfolded protein response, and the integrated stress response (ISR) (178,290-292). Wherein activation during stress conditions is necessary for survival, and prolonged/chronic activation is deleterious to the cell. Nuanced studies regarding substrate-specific activity are needed to further disentangle the role of LonP1 and mitochondrial protein turnover in cell fate decisions during I/R injury.

Interplay between Quality Control Pathways and Mitochondrial Dynamics

Mitochondrial morphology and function are tightly regulated by the cooperating pathways of mitochondrial dynamics and quality control. An abundance of evidence points to crosstalk between mitochondrial fission/fusion with mitophagy, proteostasis, and the mtUPR (273,293,294). Additionally, mitochondrial dynamics are highly involved in the response to I/R injury (42,273,295). To elucidate the effects of mitochondrial fission and fusion on protein turnover, we analyzed MitoTimer turnover in Drp1 (fission) and Opa1 (fusion) cKO neurons in OGD/R. Interestingly, Drp1 cKO neurons displayed no protein turnover peak at 2hR, in fact, red MitoTimer signal steadily increased over time during reoxygenation. This deficiency due to fission impairment has also been reported in flies and human patient fibroblasts (187,189,296). Mitochondrial fission additionally has an inverse relationship with whole cell proteostasis and ISR and mtUPR initiation (189,297,298). Conversely, much less is known about the interactions between mitochondrial fusion and protein turnover. Opa1 cKO cells showed a large shift in MitoTimer red/green ratio towards newly synthesized proteins, indicative of upregulated turnover of old/red MitoTimer. This pattern was consistent throughout OGD/R. Intriguingly, this effect contrasts previous studies with Opa1 and MitoTimer. MitoTimer expression in rat insulinoma cells (INS1) after Opa1 knockdown revealed increased heterogeneity of the red/green ratio due to fusion inhibition; however, overall red/green ratios were not compared to control cells (83). Additionally, Opa1 knockdown in *Drosophila* resulted in increased oxidative stress and red MitoTimer in nerve tissue (299). The differences in our findings and these studies may depend on organismal (rat, fly, mouse) or cell environment factors (immortalized, *in vivo*, primary culture). To probe the potential effectors of the Opa1 cKO phenotype, we assessed protease expression levels at baseline

conditions. Opa1 cKO cells had massively upregulated levels of Oma1. This inner membrane metalloprotease is responsible for Opa1 processing, protein import, and stress signaling (139). Due to the interdependent relationship between Opa1 and Oma1, the MitoTimer phenotype observed in this study may not be completely representative of fusion perturbation, but rather a specific effect of Opa1 loss. Future studies focusing on other fusion machinery (e.g., Mfn1, Mfn2) would provide clarity on these observations.

Conclusion

This study reveals a novel neuronal pattern of mitochondrial protein turnover during *in vitro* I/R injury. LonP1 and Parkin are identified as key mediators of the observed protein dynamics. Importantly, the proteolytic and mitophagic responses work in cooperation with the forces of mitochondrial dynamics, as evidenced by the effects of fission and fusion loss. This reoxygenation-induced proteostasis could serve as a future therapeutic window for modulation of mitochondrial quality control. Further work is needed to better our understanding of how LonP1 and mitochondrial protein turnover contribute to critical cell fate decisions and repair after neuronal I/R injury.

3.4 Materials and Methods

Animals

All procedures were performed in accordance with institutional guidelines and approved by the University of Michigan Institutional Animal Care and Use Committee (IACUC). Mice were maintained on a 12 h light/dark cycle with standard rodent chow and water available ad libitum. Wild-type (WT) mice (C57BL/6J) were purchased from The Jackson Laboratory (Bar Harbor, ME). Drp1 floxed ($Drp1^{flx/flx}$) mice (Dnm1ltm1.1Hise) were generously provided by Hiromi Sesaki, Johns Hopkins University, Baltimore, MD (242). Opa1 floxed ($Opa1^{flx/flx}$) mice were generously provided by Luca Scorrano, University of Padua, Italy (243). Conditional MitoTimer mice were generously provided by Zhen Yan, Virginia Polytechnic Institute and State University, VA (268). Parkin null mice (B6.129S4-Prkntm1Shn/J) were purchased from The Jackson Laboratory (Bar Harbor, ME).

Genotyping

Ear and tail samples, collected from adult and postnatal mice, were lysed in DirectPCR Lysis Reagent (Mouse Tail; Viagen, 102-T) overnight at 55 °C. The following day, samples were boiled for 10 min. Gene fragments were amplified by polymerase chain reaction (PCR) with 5x Green GoTaq Reaction Buffer (Promega, M791A), dNTP mix (Promega, U1515), and GoTaq G2 DNA polymerase (Promega, M7848). PCR products were run on 1.5% agarose gels with 1X GelRed Nucleic Acid Stain (MilliporeSigma, SCT123) and visualized via iBright1500 imager (Invitrogen). Primer sequences used in this study were as follows: MitoTimer (tg Fwd) GAGTTCATGCGCTTCAAGGT, (tg Rev) GAGGTGATGTCCAGCTTGGT, (control Fwd) CTA GGCCACAGAATTGAAAGATCT, (control Rev) GTAGGTGGAAATTCTAGCATCATCC; $Drp1^{flx}$ (Fwd) ACCAAAGTAAGGAATAGCTGTTG, (Rev) ATGCGCTGATAATACTATCAACC; $Opa1^{flx}$ (Fwd) CAGTGTTGATGACAGCTCAG, (Rev) CATCACACACTAGCTTACATTTGC.

Primary Neuron Culture

Cerebral cortices from postnatal day 0–1 (P0–P1) mouse pups were isolated and minced following sacrifice by decapitation. Tissue was incubated in enzyme digestion solution (Hibernate-A Medium (Gibco, A1247501), 1X B-27 supplement (Gibco, 17504044), 0.06 mg/mL L-cysteine (Sigma, 778672), 1.4×10^{-2} N NaOH (Sigma, 43617), 10 ng/mL APV (2-Amino-5-phosphonopentanoic acid, Sigma, A-5282), 1:100 Papain (Worthington, LS 03126), 40µg/mL Dnase I from bovine pancreas (Roche, 11284932001) for 30 min at 37 °C. Following digestion, tissue was washed with DPBS and dissociated in Hibernate-A medium with 1X B-27. Cell density was measured by hemocytometer and trypan blue staining. Cells were seeded onto 0.1% PEI-coated glass coverslips in 24-well dishes (0.3 x 10^6 cells/well), 6-well dishes (1.5 x 10^6 cells/well) or 60mm dishes (4.5 x 10^6 cells/dish). After 30 min, complete media change was performed with neurobasal complete medium (1x Neurobasal Plus medium (Gibco, A3582901), 1X B-27 Plus supplement (Gibco, A3653401), 0.5 mM Glutamax Supplement (Gibco, 35050061), and 1% Penicillin/Streptomycin Solution (Gibco, SV30010)). Cells were incubated at 37 °C with 5% CO2 for 14 days. Half-media changes were performed every 3–4 days with neurobasal complete medium.

Viral transduction

Viral infection was performed 7 days prior to experimentation on day-in-vitro 7 (DIV7). Adeno-associated viruses were generated by the University of Michigan Vector Core (rAAV8-hSyn-Cre). Neuron-specific conditional expression of MitoTimer and knockout of target proteins was performed via administration of AAV8-hSyn-Cre at 2 x 10^{10} vg/mL. Infection rates and neuron specificity were determined by administering AAV8-hSyn-eGFP at varying concentrations. AAV8-CAG-empty was used as viral control when applicable. Half-media changes were performed the day following infection.

Oxygen-Glucose Deprivation and Reoxygenation (OGD/R)

Oxygen-glucose deprivation was performed in O_2 Control In Vitro Glove Box (Coy Lab Products). The chamber was maintained at <0.1% O_2 and 5% CO_2. EBSS without glucose was bubbled in the hypoxic chamber with 95% N_2/5% CO_2 gas for 60 min for deoxygenation. Cells were placed inside the chamber and washed 3x with deoxygenated EBSS (no glucose) and allowed to incubate for 90 min. Cells were then removed from the chamber and reoxygenated with Neurobasal Plus medium with 1X B-27 minus antioxidants (Gibco, 10889038) and incubated at 37 °C in 5% CO_2. Control cells remained at normoxic conditions, were washed 3X EBSS with glucose, and changed to Neurobasal Plus medium with 1X B-27 minus antioxidants after 90 min. CDDO-Me treatment (0.5μM) was administered at the onset of reperfusion in the appropriate experiments.

Immunofluorescence & Fluorescent Microscopy

Cells on coverslips were washed with DPBS and fixed with 4% paraformaldehyde (Fisher Scientific, 50980487) for 15 min at 37 °C. Following fixation, cells were washed 3x with DPBS and stored at 4 °C. For immunofluorescent staining, coverslips were incubated in blocking solution (5% goat serum (Sigma, G9023) and 0.3% Triton-X100 (Acros Organics, 215682500) in PBS) for 60 min. Coverslips were then incubated in primary antibody solution (1:1000 Chicken Anti-MAP2 (Abcam, ab5392), 1% BSA (Sigma, A9647) and 0.3% Triton-X100 in PBS) at 4 °C overnight. Coverslips were then washed 3x in PBS and incubated in secondary antibody solution (1:200 Anti-Chicken Alexa Fluor 647 (Invitrogen, A21449), 1% BSA (Sigma, A9647) and 0.3% Triton-X100 in PBS) for 60 min. Coverslips were mounted on glass slides using Fluoroshield with DAPI (Sigma, F6057) after 3x washes with PBS.

Cells were imaged via Zeiss Axio Observer Z1 inverted microscope with LED illumination. For each coverslip, 7-8 image z-stacks (0.24 μm slices) were acquired at 63x magnification with oil immersion. MitoTimer experiments were performed with 2-3 technical replicate coverslips, therefore 14-24 images were acquired per biological replicate in each condition. Z-stacks were processed using Zeiss Zen Pro extended depth of focus wavelets method. Images were exported in TIFF format for post-processing. LED power, exposure time, and histograms were fixed for all MitoTimer experiments.

MitoTimer Analysis

MitoTimer image analysis was performed in FIJI (213). Merged TIFF images of the green and red channels were imported and converted to 8-bit grayscale. Background noise was removed using a rolling ball radius of 20 pixels. Mitochondrial objects (positive for green and/or red signal) were segmented using the Trainable Weka Segmentation plug-in (240). The segmentation classifier model was trained using hand identified mitochondria from processed images. Resultant segmented images were converted to 8-bit binary and the known scale was set. The Analyze Particles plug-in was used to define discrete mitochondrial objects and store them as regions of interest (ROIs). All ROIs for a given image were combined and the mean intensity was measured in the raw images for the green and red fluorescent channels (Fig. 3-10). These measurements defined the mean fluorescent intensity of all mitochondrial area in each respective channel. The MitoTimer red/green ratio was then calculated by dividing the red intensity by the green intensity for each image. Ratios were averaged across all images from individual biological replicates.

Western Blot

Cells were scraped in homogenization buffer (10mM HEPES (MilliporeSigma, H-4034), 1mM EDTA (ThermoFisher, J15694-AP), 1mM EGTA (MilliporeSigma, 324626), 100mM KCl (Calbiochem, 7300), 210mM D-Mannitol (MilliporeSigma, M4125), 70mM Sucrose (MilliporeSigma, S0389), 1x Halt Protease & Phosphatase Inhibitor (Fisher Scientific, 78444) in ddH_2O) and lysate was collected on ice. Samples were then sonicated and protein concentration was measured using the Bradford Plus Assay Reagent (ThermoFisher, PI23236). Polyacrylamide gels (7.5% and 4-20% 29:1 polyacrylamide/bisacrylamide (Fisher BioReagents, BP1408-1), 375 mM Tris pH 8.8 (Fisher BioReagents, BP152-1), 0.1% sodium dodecyl sulfate (SDS, Sigma, L3771), 0.1% ammonium persulfate (APS, Sigma, #A3678), and 0.1% TEMED (GE Healthcare,

45-000-226)) were loaded with 5-10µg of whole cell lysates and transferred to nitrocellulose membranes. Membranes were incubated with primary antibodies (1:1000 Rabbit Anti-α-Tubulin (Cell Signaling, 11H10); 1:2000 Rabbit Anti-AFG3L2 (ProteinTech, 14631-1-AP); 1:5000 Mouse Anti-β-Actin (Abcam, ab8226); 1:2000 Rabbit Anti-CLPP (ProteinTech, 15698-1-AP); 1:1000 Mouse Anti-Dlp1/Drp1 in 2% milk (Clone 8, BD Transduction Laboratories, BD6111112); 1:10,000 Rabbit Anti-GAPDH (14C10, Cell Signaling, 2118); 1:1000 Mouse Anti-HSP60 (BD Transduction Laboratories, 611562); 1:1000 Rabbit Anti-LonP1 (ProteinTech, 1540-1-AP); 1:10000 Rabbit Anti-NDUFS1 (Abcam, ab169540); 1:200 Mouse Anti-Oma1 (Santa Cruz, sc-515788); 1:1000 Mouse Anti-Opa1 (BD Transduction Laboratories, BD612607); Mouse Anti-Total OXPHOS Cocktail (MitoScience, MS604); 1:200 Mouse Anti-TFAM (Santa Cruz, sc-166965; 1:200 Rabbit Anti-TOMM20 (ProteinTech, 11802-1-AP); 1:300 Rabbit Anti-Yme1L (ProteinTech, 11510-1-AP)) at 4 °C overnight. Membranes were washed 3x with Tris-Buffered Saline and 0.1% Tween (TBST, Fisher Scientific, BP337500) and incubated in secondary antibodies (1:5000 Donkey Anti-Mouse (Jackson Immuno Research Labs, 715-035-150 or 1:10000 Donkey Anti-Rabbit (Jackson Immuno Labs, 711-035-152) for 60 min at RT. All antibodies were prepared with 2% BSA in TBST unless otherwise specified. Membranes were then washed 3x with TBST. Membranes were incubated in SuperSignal West Pico Plus Chemiluminescent Substrate (ThermoFisher, 34577) and imaged with iBright 1500 imager (Invitrogen) and quantified by densitometry using FIJI.

Mitochondrial Fractionation & Protease Activity Assay

Cells (3-4 million) were scraped in fractionation buffer (10mM HEPES (MilliporeSigma, H-4034), 100mM KCl (Calbiochem, 7300), 210mM D-Mannitol (MilliporeSigma, M4125), 70mM Sucrose (MilliporeSigma, S0389) in ddH_2O) and whole cell lysate was collected on ice. Lysate was homogenized using a Teflon Potter-Elvehjem homogenizer (35 strokes at 300 rpm) (Thomas Scientific, 3432S90). Homogenates were then centrifuged at 1000 g for 10 min at 4 °C. The supernatant (mitochondria and cytosol) was centrifuged at 10,000 g for 10 min at 4 °C. The supernatant (cytosolic fraction) was discarded. Mitochondrial pellets were washed once with PBS and resuspended in fractionation buffer and sonicated. Protein concentration was measured using the Bradford Plus Assay Reagent (ThermoFisher, PI23236). The Pierce Fluorescent Protease Assay (Thermo Scientific, 23266) was performed per manufacturer's instructions. The assay was

performed in technical duplicates containing 3 μg of mitochondrial lysate in the presence of 3 mM ATP (MilliporeSigma, 20-306). For inhibitor treatment, 0.5 μM CDDO-Me (MilliporeSigma, SMB00376) was added to the reoxygenation media and additionally added to the mitochondrial lysate before the protease assay.

Statistical Analysis

Statistical analyses were performed in GraphPad Prism 8 (GraphPad Software, San Diego, CA). For comparisons of two discrete groups, one-way ANOVAs were performed, followed by post-hoc t-tests. For comparisons of more than two groups, two-way ANOVAs were performed with post-hoc comparisons made by Tukey's test corrected for multiple comparisons. Tests with $p < .05$ were considered statistically significant. The number of biological replicates is indicated by n, unless otherwise noted.

3.5 Figures

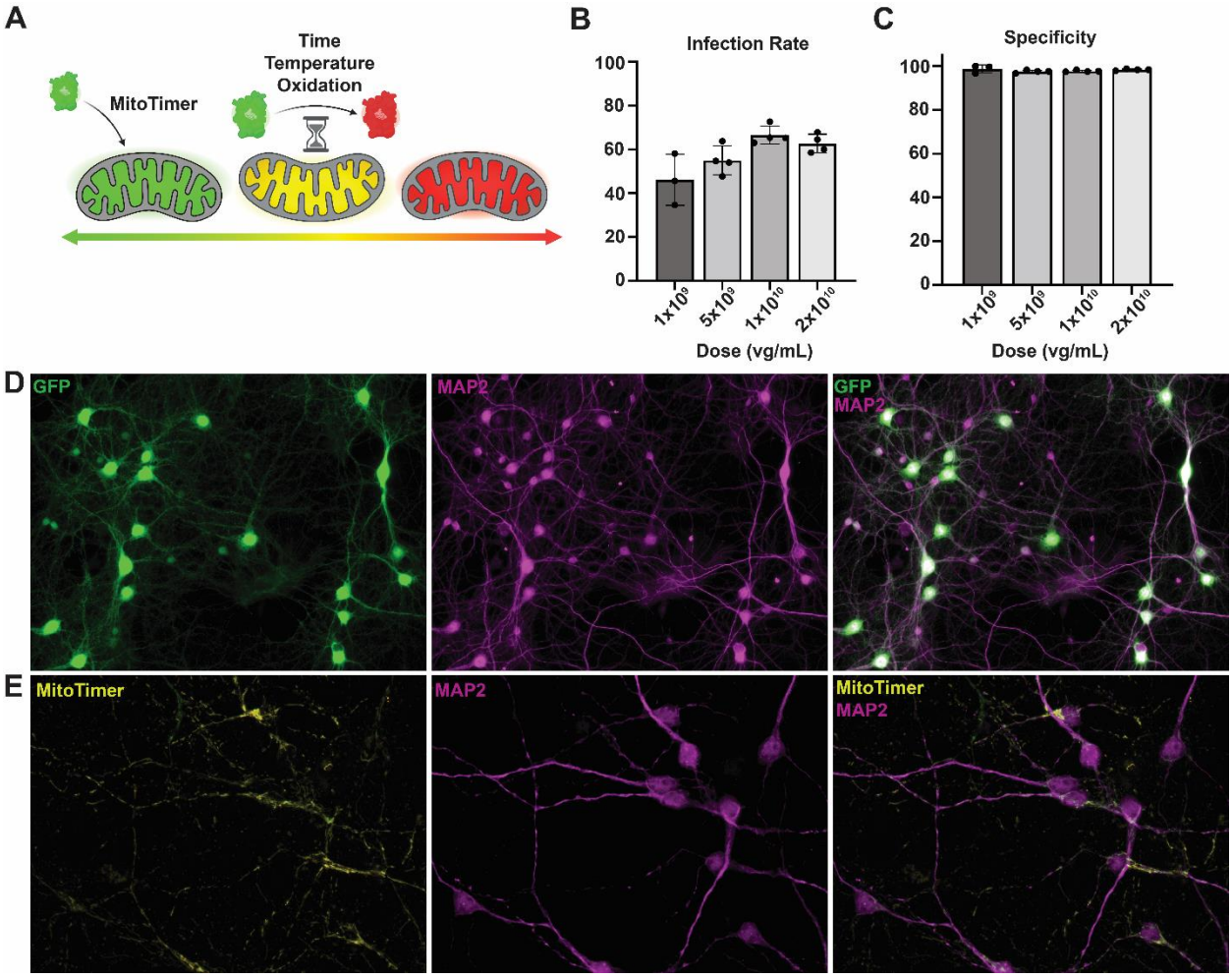

Figure 3-1. Neuron-specific expression of the fluorescent reporter MitoTimer

(A) MitoTimer protein is synthesized and trafficked to the mitochondrial matrix where it fluoresces green. Upon maturation over time, fluorescence shifts from green to red. The mix of MitoTimer green and red protein in mitochondria creates a spectrum of protein dynamics for visualization. Graphic made in BioRender. (B) Infection rates of neurons after 7 days of exposure to varying doses of AAV8-hSyn-GFP. Infection rates are quantified as the percentage of MAP2-positive neurons expressing GFP. (C) Specificity of AAV8-hSyn-GFP for neuronal transduction. Specificity is quantified as the percentage of GFP-positive cells that also express MAP2. (D) Representative images of neurons expressing GFP after infection with AAV8-hSyn-GFP. (E) Representative images of neurons expressing MitoTimer. N = 3-4 biological replicates

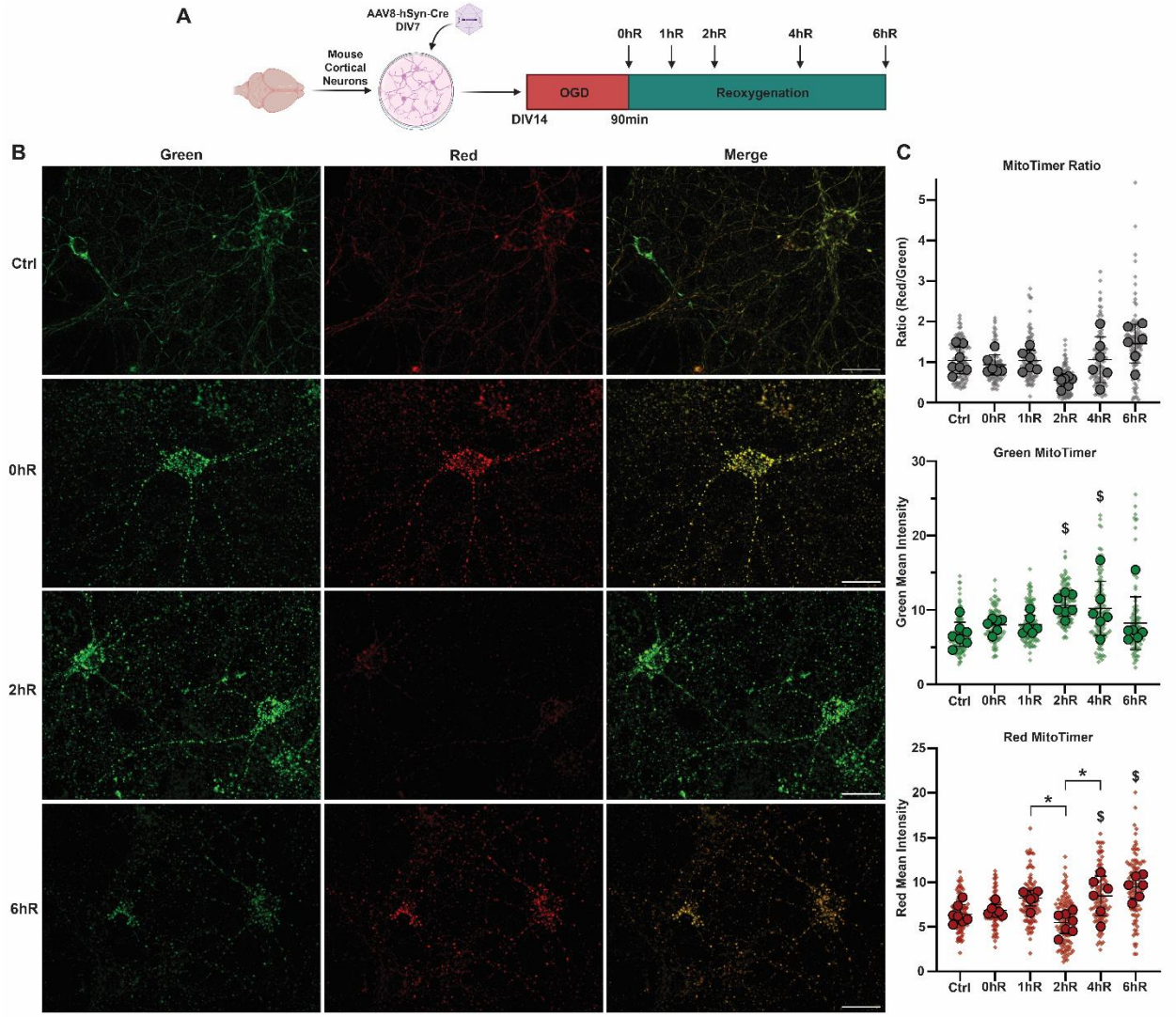

Figure 3-2. MitoTimer fluorescence dynamics following OGD/R

(A) Schematic overview of experimental timeline. Graphic made in BioRender. (B) Representative images of neuronal MitoTimer across timepoints throughout OGD/R. Scale bar = 20µm. (C) Quantitation of MitoTimer ratio and fluorescent mean intensities in OGD/R. Measurements were restricted to segmented mitochondrial area in each image. Large symbols display biological replicates, small symbols represent individual images. Statistical tests were performed using biological replicates. N = 6-7 biological replicates. * indicates $p < .05$ in pair-wise comparison. $ indicates $p < .05$ compared to control.

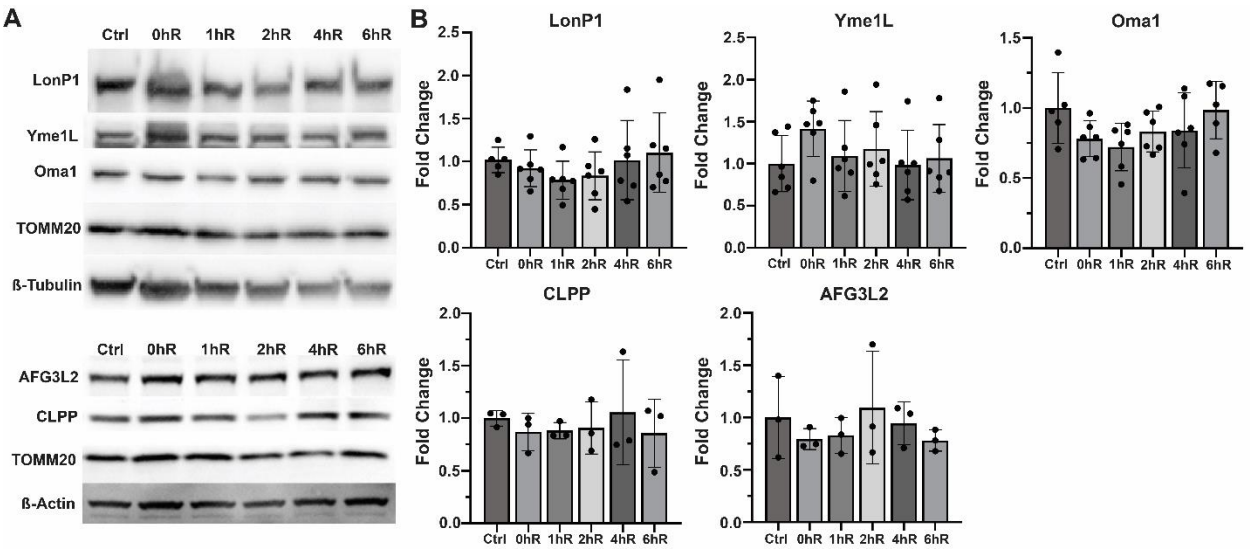

Figure 3-3. Mitochondrial protease levels are not changed in OGD/R

(A) Representative Western blots of mitochondrial proteases from neuronal whole cell lysates. (B) Quantification of mitochondrial matrix and inner membrane proteases in OGD/R corrected for mitochondrial content (TOMM20 expression) and normalized to normoxic control. N= 3-6 biological replicates.

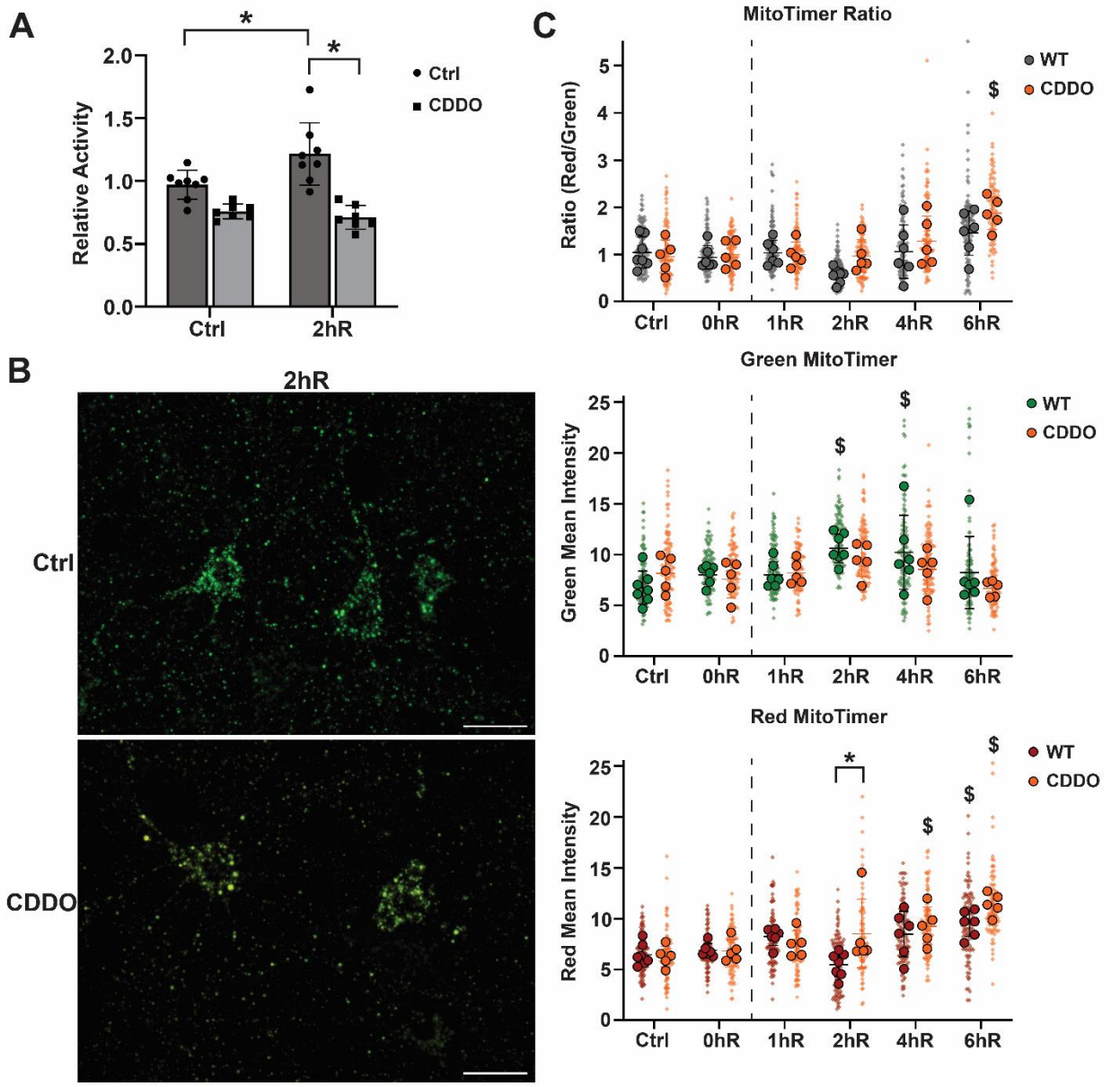

Figure 3-4. LonP1 contributes to protein turnover during reoxygenation

(A) Protease activity of mitochondrial lysates with(out) CDDO-Me (0.5μM) measured by FITC-casein proteolysis assay fit to Trypsin standard curve and normalized to normoxic control. N = 6-8 biological replicates. (B) Representative images of MitoTimer signal at 2hR for WT cells with(out) CDDO-Me treatment. Scale bar = 20μm. (C) Quantification of MitoTimer red/green ratio, green intensity, and red intensity throughout OGD/R. Dotted line indicates administration of CDDO-Me at onset of reoxygenation. N = 5-7 biological replicates. * indicates $p < .05$ in pair-wise comparison. $ indicates $p < .05$ compared to respective control.

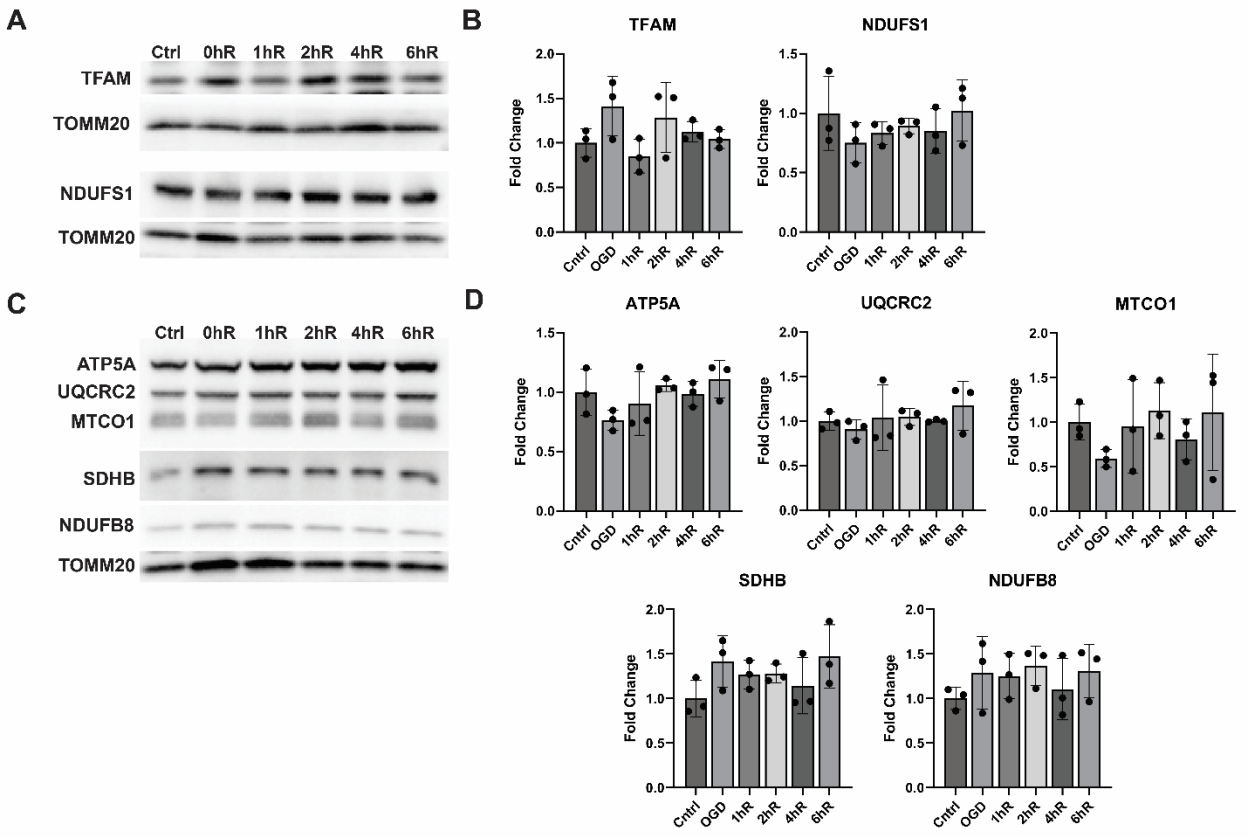

Figure 3-5. LonP1 substrates and OXPHOS subunits are unchanged during OGD/R

(A) Representative Western blots of TFAM and NDUFS1 during OGD/R. (B) Quantifications of Western blots for LonP1 substrates. N = 3 biological replicates. (C) Representative Western blots of OXPHOS antibody cocktail during OGD/R. (D) Quantifications of Western blots for OXPHOS components. All protein levels are corrected by TOMM20 levels and normalized to the mean of control. N = 3 biological replicates

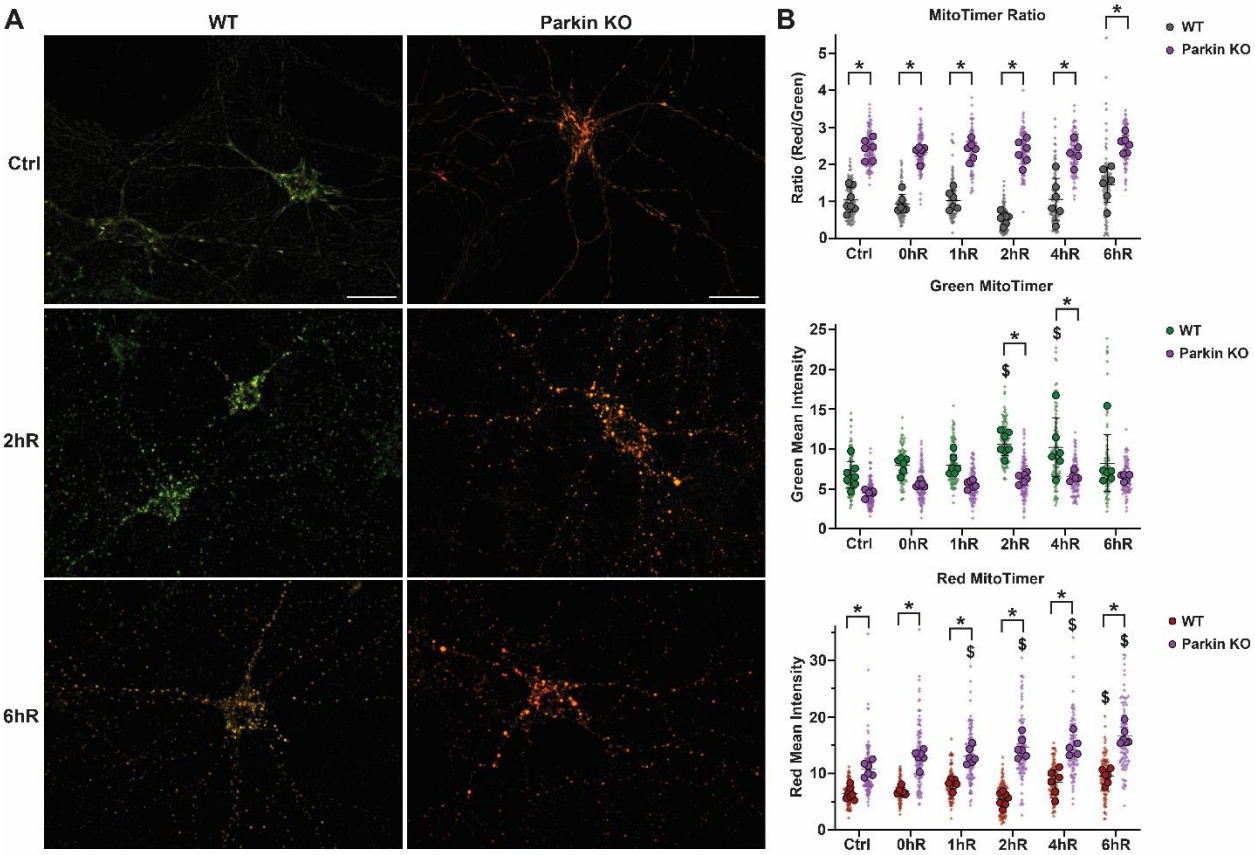

Figure 3-6. Parkin regulates protein turnover during basal and stress conditions

(A) Representative images of MitoTimer signal from WT and Parkin KO cells at control conditions and 2hR. Scale bar = 20μm. (B) Quantification of MitoTimer red/green ratio, green intensity, and red intensity throughout OGD/R. n = 5-7 biological replicates. * indicates $p < .05$ in pair-wise comparison. $ indicates $p < .05$ compared to respective control.

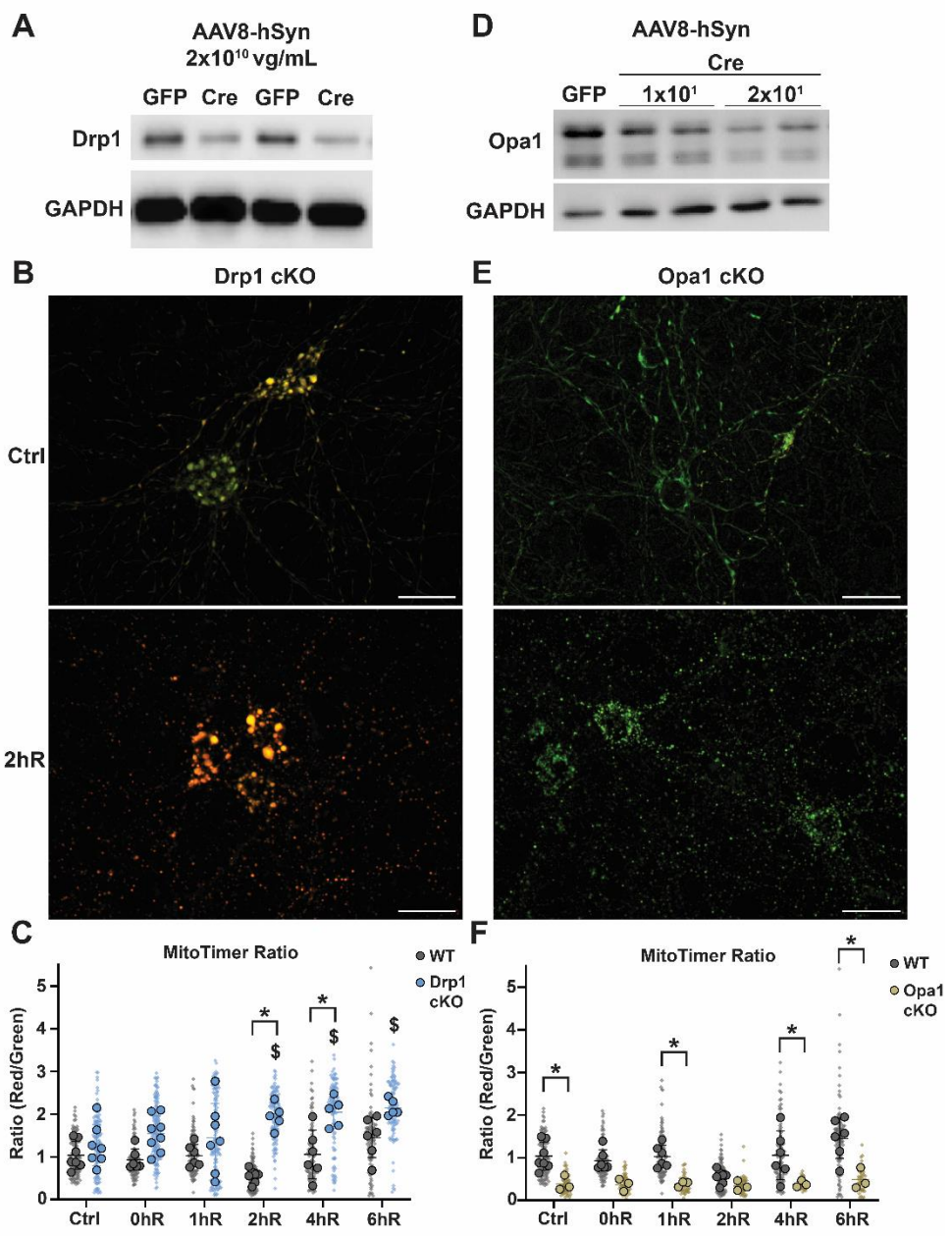

Figure 3-7. Drp1 and Opa1 differentially affect mitochondrial protein turnover

(A) Representative Western blot of Drp1 cKO after Cre expression. Control cells were transduced with a GFP vector. (B) Representative images of Drp1 cKO MitoTimer cells at baseline conditions and after OGD and 2 hours reoxygenation. Scale bar = 20µm. (C) Quantification of MitoTimer red/green ratio during OGD/R in WT and Drp1 cKO neurons. N = 3-8 biological replicates. (D) Representative Western blot of Opa1 cKO after Cre expression. Viral concentrations after listed in vg/mL. (E) Representative images of Opa1 cKO MitoTimer cells at baseline conditions and after OGD and 2 hours reoxygenation. Scale bar = 20µm. (F) Quantification of MitoTimer red/green ratio during OGD/R in WT and Opa1 cKO neurons. N = 3-7 biological replicates. * indicates $p < .05$ ©n pair-wise comparison. $ indicates $p < .05$ compared to respective control.

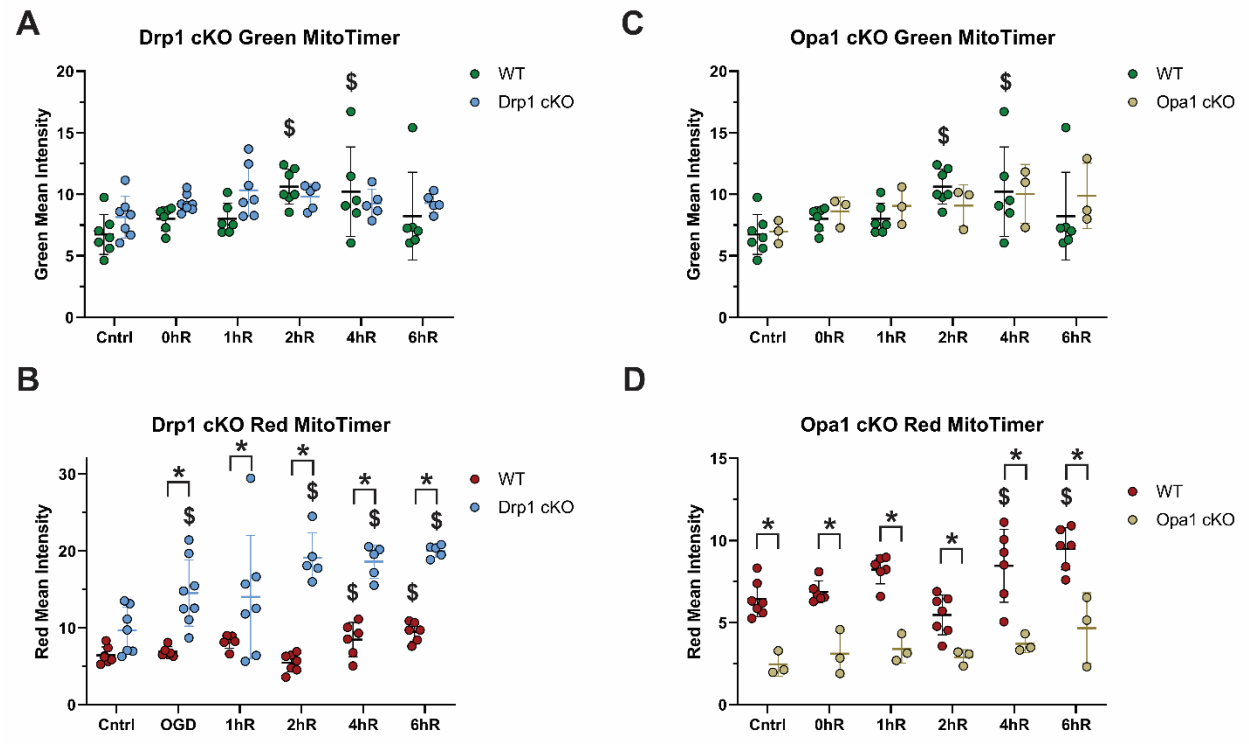

Figure 3-8. MitoTimer green and red signal in Drp1 and Opa1 cKO

(A) Quantification of MitoTimer green intensity throughout OGD/R in WT and Drp1 cKO cells. (B) Quantification of MitoTimer red intensity throughout OGD/R in WT and Drp1 cKO cells. N = 6-7 biological replicates. (C) Quantification of MitoTimer green intensity throughout OGD/R in WT and Opa1 cKO cells. (D) Quantification of MitoTimer red intensity throughout OGD/R in WT and Opa1 cKO cells. N = 3-7 biological replicates. * indicates $p < .05$ in pair-wise comparison. $ indicates $p < .05$ compared to respective control.

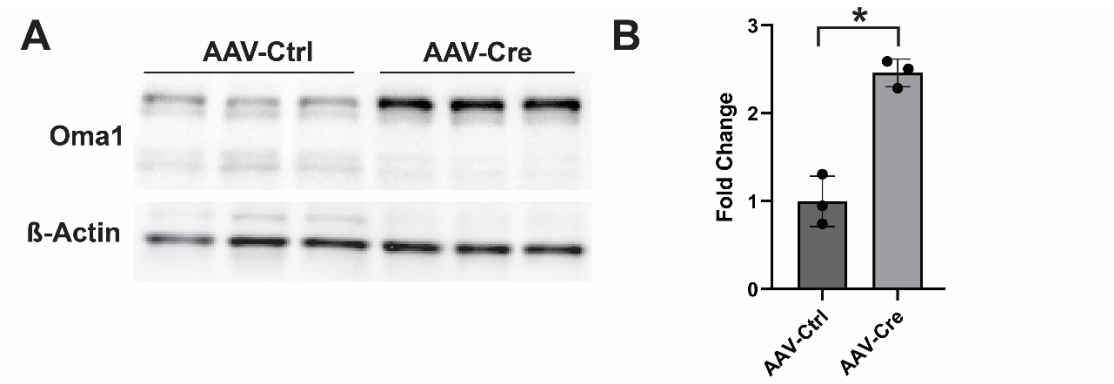

Figure 3-9. Oma1 protease levels are increased in Opa1 cKO cells

(A) Representative Western blot of Oma1 levels in Opa1 cKO cells. (B) Quantification of Oma1 protein levels in Opa1 cKO cells, normalized by beta-Actin. N = 3 biological replicates. * indicates $p < .05$

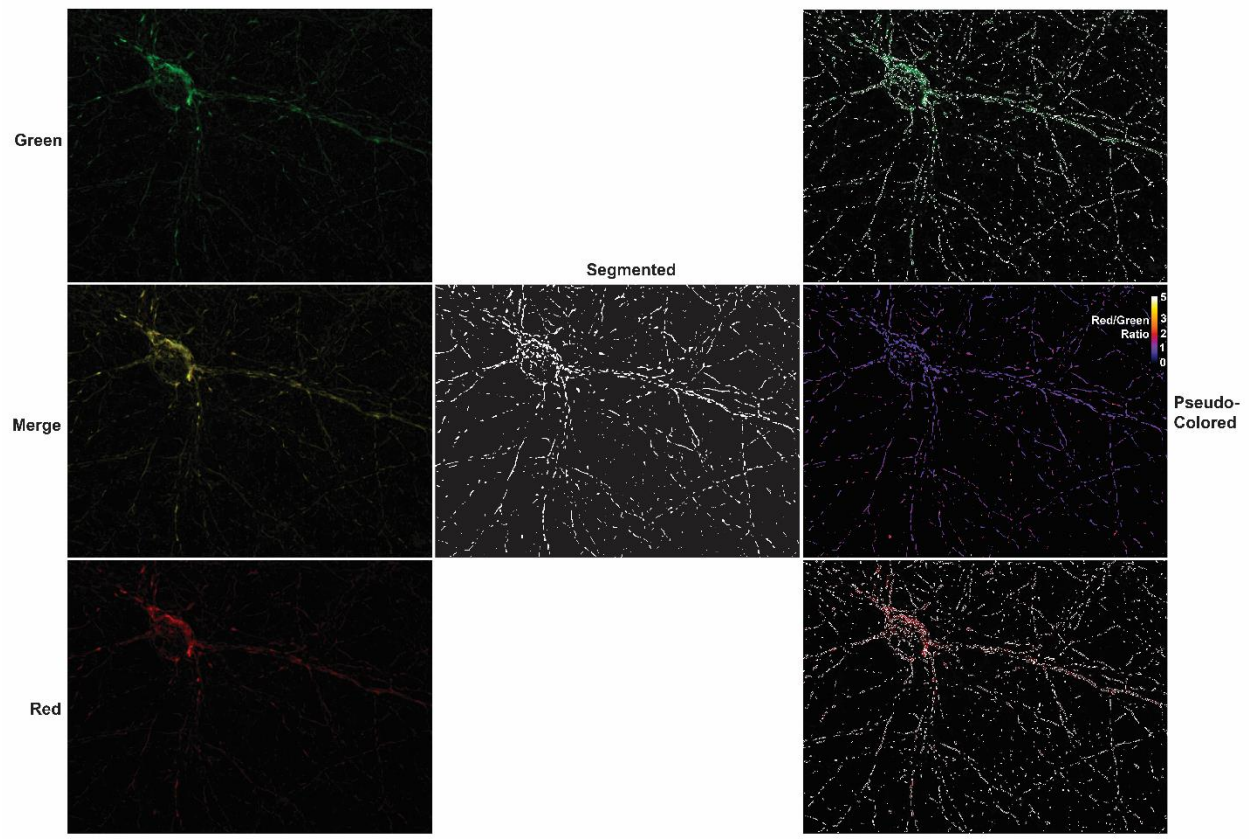

Figure 3-10. Image processing pipeline for MitoTimer analysis

MitoTimer green and red images are merged, converted to 8-bit, and background is subtracted. Mitochondrial area is segmented and defined as the mitochondrial ROI. ROI is overlaid onto original green and red images for measurement of respective intensities across all mitochondrial area. The MitoTimer red/green ratio is psuedo-colored and scaled for visual inspection.

Chapter IV: Mitochondrial Membrane Potential and Oxidative Stress Interact to Regulate Oma1-dependent Processing of Opa1 and Mitochondrial Dynamics [3]

4.1 Introduction

Mitochondrial fusion is stimulated while fission is slowed at the onset of reperfusion (Chapter II; 85,86). Fusion is however halted during later reperfusion, with fission once again taking over. This pattern prompted us to investigate possible mechanisms underlying fusion dissipation during reperfusion.

Optic atrophy 1 (Opa1) is a dynamin-related GTPase localized to mitochondrial cristae junctions that plays several important roles in mitochondrial biology. It has been well characterized that Opa1 mediates mitochondrial inner membrane fusion, cristae remodeling, and ER-mitochondria contacts (47,300-302). These functions are critical for cellular homeostasis and efficient mitochondrial function, making Opa1 an important protein for cell survival, differentiation, and function (303-306). Opa1 exists in most mammalian cells with up to 8 different isoforms, commonly expressed as 5 isoforms in the brain (78,79,307). Opa1 protein contains cleavage sites for two mitochondrial inner membrane proteases, Oma1 and Yme1L. These two proteases work in tandem to cleave splice variants of long Opa1 (L-Opa1) into short Opa1 (S-Opa1) (217,308). Differential isoform expression and proteolytic processing of Opa1 protein give rise to 5 distinct protein bands in brain tissue when resolved by Western blot (78,79,307). Intriguingly, complete and efficient mitochondrial fusion requires a balance of both L-Opa1 and S-Opa1 protein (80,307). The necessity for balance of Opa1 isoforms places importance on understanding how Oma1 and Yme1L mechanistically operate and react to varying cellular conditions.

[3] This chapter is composed of the submitted manuscript: "Fogo GM, Raghunayakula S, Emaus KJ, Torres Torres FJ, Wider JM, Sanderson TH. Mitochondrial membrane potential and oxidative stress interact to regulate Oma1-dependent processing of Opa1 and mitochondrial dynamics. *Submitted.*". Sarita Raghunayakula generated the CRISPR Cas9 KO of Oma1 in HT22 cells. I performed all remaining experiments.

Oma1 and Yme1L protease activity also requires a coordinated and balanced relationship. Oma1 and Yme1L cleave Opa1 at different sites, S1 and S2 respectively, and therefore produce unique S-Opa1 isoforms (79,308). Although the exact functions of each Opa1 isoform have not been resolved, the measurement of individual S-Opa1 isoform abundances allows for the assessment of each protease's relative activity. At homeostatic conditions, Yme1L is preferentially active, while Oma1 is better characterized as a stress-induced protease (309,310). This relationship is maintained in part due to reciprocal degradation of Oma1 and Yme1L, in which ATP availability determines the dominant active protease (311). In addition to the processing of Opa1, these proteases are involved in other aspects of mitochondrial biology, including protein import, stress signaling, and mitophagy (139,140,312). Together, these roles make delineation of Oma1 and Yme1L activation mechanisms integral to our understanding of basic mitochondrial biology and the response to stress. Due to its constitutive activity during basal conditions, little is known about the regulators of Yme1L activation. However, Oma1 has been demonstrated to be activated by many stresses, injuries, and diseases (43,306,313). The predominant mechanism described for Oma1 is activation by depolarization of the mitochondrial membrane potential (309,311,314). Commonly induced by protonophore treatment (e.g. FCCP, CCCP), depolarization is believed to be sensed by a string of positive amino acid residues on the N-terminus of Oma1. The matrix-localized N-terminus is required for depolarization-induced activation and may change conformation in response to polarization changes across the inner mitochondrial membrane (314). However, this mechanism is complicated by other findings that stresses such as heat, oligomycin (hyperpolarizing agent), hydrogen peroxide (H_2O_2), and apoptotic proteins are also sufficient to induce Oma1 activation (314-316). Oma1-dependent Opa1 processing has also been observed during neuronal I/R paradigms, which include combinatorial mitochondrial stresses (e.g. depolarization, oxidative stress) (85,88,317,318). Understanding the specific aspects of Oma1 activation during I/R could help identify mechanisms for therapeutic intervention to promote mitochondrial fusion and recovery after injury.

In this study, we aimed to determine the presence of Oma1 activation and Opa1 processing in a neuronal model of I/R injury and identify the potential causative mechanisms. Utilizing *in vitro* methodologies, we assayed Oma1-mediated cleavage of Opa1 in depolarizing, hyperpolarizing, and oxidative conditions. Additionally, we investigated the dependency of Oma1 activation on oxidative stress and the contributions of Oma1 to mitochondrial fission and fusion.

Ultimately, our results demonstrate the dynamic nature of Oma1 activation and its importance in both reaction to and recovery from mitochondrial stress.

4.2 Results

4.2.1 Neuronal Opa1 processing and Oma1 activation in oxygen-glucose deprivation and reoxygenation (OGD/R)

Mitochondrial fission and fusion play important roles in the response to I/R injury (42). Due to its importance in mitochondrial fusion, we evaluated the status of Opa1 during neuronal oxygen-glucose deprivation and reoxygenation (OGD/R; an *in vitro* model of I/R in primary neuron cultures). Opa1 has five dominant protein bands (*a*-*e*) in murine neurons that work in coordination to perform inner membrane fusion and other essential functions (47,78,79). The long Opa1 isoforms (L-Opa1) *a* and *b* are splice variants, with cleavage sites for the two mitochondrial proteases Oma1 and Yme1L. Cleavage of splice variants by each protease produces unique short Opa1 (S-Opa1) bands: Oma1 produces *c* and *e*, Yme1L produces *d* (Fig. 4-1A). The balance of L-Opa1 and S-Opa1 is critical to maintain proper function, with an ideal ratio around 1:1 (80). Mouse primary cortical neurons displayed an equal balance of L-Opa1 and S-Opa1 at control conditions (Fig. 4-1B). We hypothesized that OGD would stimulate Opa1 cleavage, while reoxygenation would exacerbate this effect. Indeed, upon OGD, loss of the *b* band was evident with an increase in the Oma1-dependent *e* band. However, this pattern of increased Opa1 processing did not progress further and remained consistent from the conclusion of OGD (0hR) through 6 hours of reoxygenation (6hR; Fig. 4-1B,D). The protease Oma1 performs autocatalytic self-cleavage upon activation (314). Interestingly, we observed an increase of cleaved Oma1 product throughout the progression of OGD/R, but no significant change in total Oma1 levels (Fig. 4-1C,E). Together, these results demonstrate that neuronal OGD/R induces alterations in Oma1 and Opa1 proteolytic processing in response to injury.

4.2.2 Opa1 processing is sensitive to both mitochondrial depolarization and hyperpolarization

The proteolytic processing and activation of Opa1 and Oma1 during OGD/R prompted us to investigate the specific mitochondrial stresses that could be responsible for disruption of mitochondrial homeostasis. It has been demonstrated that positively charged amino acids on the matrix-localized N-terminus of Oma1 regulate its activation upon mitochondrial membrane depolarization (314). Therefore, we investigated the effects of mitochondrial membrane potential

depolarization on Opa1 processing. The electron transport chain (ETC) inhibitors rotenone (complex I inhibitor; 20μM) and antimycin A (complex III inhibitor; 20μM), along with the protonophore FCCP (3μM), were applied to HT22 cells (mouse hippocampal neuronal cell line) for 2 hours (Fig. 4-2A). Depolarization of the mitochondrial membrane potential was confirmed by flow cytometry with TMRM, a mitochondrial membrane potential-sensitive dye (Fig. 4-2B). Both rotenone and FCCP were sufficient to induce Opa1 cleavage, however, antimycin A treatment did not produce increased S-Opa1 (Fig. 4-2C,D). Conversely, we tested the effects of two hyperpolarizing agents, oligomycin (5μM) and histamine (500μM). Oligomycin, an inhibitor of ATP synthase (complex V), significantly increased hyperpolarization and Opa1 cleavage (Fig. 4-2E-G). Histamine causes increased cytosolic and subsequently mitochondrial calcium to hyperpolarize the mitochondria via increased oxidative phosphorylation activity (319-322). Interestingly, hyperpolarization by histamine was not sufficient to increase Opa1 processing above baseline (Fig. 4-2E-G). These experiments show that Opa1 processing can be induced by compounds that drive both mitochondrial membrane depolarization and hyperpolarization.

4.2.3 Opa1 processing is contextually dependent on oxidative stress

Toxins and stressors modulate multiple aspects of mitochondrial function and are not limited to membrane polarization. Therefore, we set out to investigate other possible factors influencing Oma1 activation and Opa1 processing. Focusing on oxidative stress, we applied 50μM hydrogen peroxide (H_2O_2) to HT22 cells for 2 hours and found significant cleavage of Opa1 (Fig. 4-3A,B). To confirm that oxidative stress was present in the other conditions, we evaluated mitochondrial reactive oxygen species (mROS) production via flow cytometry with MitoSOX, a mitochondrial-specific superoxide indicator. Drugs that affected mitochondrial membrane potential and induced Opa1 processing (rotenone, oligomycin, FCCP) all produced elevated levels of mROS (Fig. 4-3C). Notably, 20μM antimycin A produced a small amount of mROS and did not induce Opa1 processing, suggesting that high mROS levels may be required to induce Opa1 processing. To test the direct involvement of mROS in stress-induced Opa1 processing, we pre-treated cells with the antioxidant N-acetyl cysteine (NAC; 3mM) for 1 hour prior to stress/drug treatment (Fig. 4-3D). NAC pretreatment ameliorated H_2O_2, rotenone, and FCCP-induced Opa1 cleavage, suggesting that oxidative stress is necessary for Opa1 processing (Fig. 4-3E-F). However, oligomycin-treated cells could not be rescued by NAC treatment. These results underline oxidative stress as a key player in Opa1 processing, but the dependence on mROS is stress-specific.

4.2.4 Mitochondrial stress induces Opa1 processing through Oma1 proteolytic activity

The predominant Opa1 processing pattern observed after drug treatment displayed decreased *a* and *b* bands and increased *e*. This pattern is characteristic of Oma1 proteolytic activity, as only Oma1 can produce the *e* protein band (78,308). To test the dependence on Oma1, we generated Oma1 KO HT22 cells using CRISPR/Cas9 gene editing. Indeed, we found that Oma1 KO cells did not produce either *c* or *e* bands, but could generate the Yme1L-dependent *d* band (Fig. 4-4A). Treatment of Oma1 KO cells with rotenone, FCCP, and oligomycin demonstrated no significant Opa1 processing (Fig. 4-4A,B). These results identify Oma1, and not Yme1L, as the primary driver of Opa1 proteolytic processing in response to mitochondrial stress induced by rotenone, FCCP and oligomycin.

4.2.5 Oma1 has dual roles in mitochondrial dynamics under stress

Opa1 plays a critical role in mitochondrial fusion, therefore we evaluated the effects of Oma1 KO on mitochondrial morphologic disruption following mitochondrial toxin exposure. WT and Oma1 KO HT22 cells were treated with mitochondrial stressors, and stained in parallel for analysis of mitochondrial morphology. Morphology was assessed by quantifying the percentage of mitochondrial area in four distinct phenotypes (networks, unbranched, punctate, swollen) using our previously validated machine learning-based approach for mitochondrial classification (Chapter II). In control conditions, Oma1 KO cells did not present any deviations from WT control mitochondrial morphology (Fig. 4-5A). To assess mitochondrial fusion capability, cells were treated with 5μM cycloheximide (CHX), a protein synthesis inhibitor, to induce mitochondrial hyperfusion (79,323). Both WT and Oma1 KO cells produced long interconnected filamentous mitochondria after CHX treatment. Interestingly, Oma1 KO cells produced more mitochondrial fragmentation and swelling after 2 hours of 10μM FCCP treatment (Fig. 4-5A,B). This phenotype was replicated with oligomycin (5μM) treatment, but not rotenone (20μM; Fig. 4-6). These results demonstrate that a lack of Oma1, and the dependent S-Opa1 bands, may exacerbate responses and/or susceptibility to mitochondrial stress.

Despite increased mitochondrial fragmentation after stress, we hypothesized that Oma1 KO cells would have enhanced recovery after mitochondrial fragmentation due to preserved L-Opa1, whereas WT cells would possess deficient mitochondrial fusion due to a lack of L-Opa1. To test this, we applied FCCP (10μM) for 2 hours to induce L-Opa1 processing by Oma1, resulting

in a loss of L-Opa1 bands to completion in WT cells (Fig. 4-5B). Cells were then allowed to recover after FCCP washout with or without CHX for 2 hours. During recovery from FCCP in WT HT22 cells, new L-Opa1 is produced and mitochondrial fusion is restored. However, treatment with CHX, a protein translation inhibitor, blocks new L-Opa1 synthesis, while also inducing mitochondrial hyperfusion. In WT cells, FCCP induced cleavage of L-Opa1 and washout allowed for limited biogenesis of new L-Opa1, while biogenesis was blocked with CHX treatment (Fig. 4-5B). In both WT and Oma1 KO cells, washout after FCCP treatment allowed for the mitochondrial network to rebalance to a normal state (Fig. 4-5A,C). However, CHX treatment in WT cells during FCCP washout resulted in a persistent state of mitochondrial fragmentation, presumably due to the lack of L-Opa1. This phenotype was strikingly contrasted by Oma1 KO cells that fully fused in response to CHX after FCCP (Fig. 4-5A,C). In summary, we observed that stress-induced fragmentation is exacerbated by the lack of Oma1. Despite this, Oma1 KO cells were capable of mitochondrial fusion after stress and had preserved L-Opa1 protein. These studies demonstrate differential roles for Oma1 in mitochondrial fusion and fission during response to stress.

4.3 Discussion

The importance of Opa1 in mitochondrial dynamics, mito-ER contacts, cristae formation, and cell signaling pathways make understanding its regulatory mechanisms of high value. The balance of Opa1 protein isoforms, regulated by the proteases Oma1 and Yme1L, is critical for efficient function (78,80,217). Therefore, we set out to determine the temporal pattern of Opa1 cleavage in a primary neuron model of *in vitro* I/R injury and evaluate the specific stress stimuli that drive Opa1 processing. In this study, we demonstrate that Opa1 processing is stimulated in the "ischemic" state of an I/R paradigm. Further, Opa1 is preferentially processed by Oma1 in response to both depolarizing and hyperpolarizing stresses. Importantly, the effects of depolarizing agents are dependent on oxidative stress. This data expands on the current model of Oma1 activation, suggesting a role for redox sensitivity. We also evaluated the role of Oma1 in mitochondrial fusion during and after stress. Oma1 KO cells had higher rates of fragmentation upon stress, however, they were also more capable of fusion recovery after stress. These results suggest that Oma1 plays a dual role in the acute reaction to stress and recovery from mitochondrial fragmentation.

Opa1 processing in neuronal I/R

During cerebral I/R, mitochondria dynamically respond with waves of fission and fusion that accompany mitochondrial stress (42,85). As the critical regulator of inner mitochondrial membrane fusion, Opa1 is proposed to be an important mediator of these responses. In our model of primary neuron OGD/R, we identify significant Opa1 cleavage during the "ischemic" phase (OGD). In ischemia, mitochondria depolarize and are unable to perform oxidative phosphorylation, leading to ATP depletion (29,324). Depolarization is the best characterized activation stimulus for Oma1 activity, which aligns with our findings of Opa1 *c* and *e* (Oma1-dependent) band formation, along with Oma1 cleavage during OGD (309). Interestingly, Opa1 cleavage was not exacerbated, but rather preserved throughout reoxygenation. Reoxygenation brings forth a multitude of mitochondrial stressors including hyperpolarization, ROS production, and cation flux (34,324). These combinatorial stimuli did not provoke Opa1 cleavage to exceed that of the OGD phase. Our findings of OGD/ischemia-induced Opa1 processing align with many previous studies looking at neurons and the brain (85,88,174,317,326,327). However, the independent states of ischemia and reperfusion have not been well studied in regards to Opa1. The temporal resolution of this study highlights the induction of Opa1 cleavage during the initial "ischemic" phase and maintenance of its activity during reoxygenation.

It is important to note that the S-Opa1/L-Opa1 ratio is mediated by three forces: L-Opa1 biogenesis, cleavage to produce S-Opa1, and Opa1 degradation. Therefore, the lack of exacerbation during reoxygenation may be due to opposing forces of biogenesis and processing/degradation. This paradigm can be partially disentangled by analyzing Oma1 autocatalytic cleavage. Several groups have described Oma1 self-cleaving to produce a lower molecular weight Oma1 band as a potential safeguard against overactivation (309,314,316,328). We analyzed the abundance of this cleavage product throughout OGD/R and found dramatic increases over time in Oma1 cleavage. It is therefore likely that Oma1 is stimulated by OGD and continuously active throughout reoxygenation. This activity is however opposed by synthesis of new L-Opa1 and degradation of S-Opa1 to cap the S-Opa1/L-Opa1 ratio during reoxygenation.

Mitochondrial membrane polarization-dependent Oma1 activation

The dominant narrative and best characterized method of Oma1 activation is by FCCP/CCCP-induced depolarization or collapse of the mitochondrial membrane potential (309). The mitochondrial membrane potential and proton motive force across the inner mitochondrial

membrane drive oxidative phosphorylation for ATP synthesis. FCCP and CCCP are protonophores that allow free transfer of protons across biological membranes, therefore ameliorating the proton gradient in mitochondria. We first set out to replicate depolarization-induced Opa1 processing in HT22 cells. Indeed, we found that FCCP and rotenone (complex I inhibitor) were sufficient to induce both mitochondrial depolarization and Oma1-dependent Opa1 processing. However, mitochondrial depolarization by complex III inhibition with antimycin A did not activate Opa1 processing. The mechanism for these confounding effects is not known, but these findings do replicate previous studies (314). Our findings of consistent neuronal Oma1 activity during reoxygenation prompted us to investigate the effects of mitochondrial membrane hyperpolarization, a state normally observed during early reoxygenation, on Opa1 processing. Competing results were found from two hyperpolarizing agents: oligomycin and histamine. Oligomycin inhibits ATP synthase to cause hyperpolarization and ATP depletion, whereas histamine causes hyperpolarization by Ca^{2+}-induced increases in ETC activity. These results demonstrate that mitochondrial membrane potential perturbations can induce Opa1 processing by Oma1, but there is a dependence on the drug's mechanism of action. Oma1 activation by FCCP/CCCP is dependent on a string of positive residues on the matrix-facing N-terminus of Oma1 (314). The working model is therefore that the N-terminus induces conformational changes in response to membrane potential fluctuations to regulate protease function. Our findings reiterate that Oma1 can be induced by membrane potential changes, but identify paradigms in which other aspects of mitochondrial biology must be influencing activation.

Oma1 activation is responsive to oxidative stress

The differential results after polarization changes prompted us to investigate other mechanisms for Oma1 activation and Opa1 processing. Treatments with strong mitochondrial inhibitors/protonophores (e.g. oligomycin, FCCP) promote multiple aspects of mitochondrial stress including polarization, fission, metabolite depletion, and oxidative stress. We therefore postulated that the effects of polarization agents may be influenced by another causative mechanism. Mitochondrial ROS and oxidative stress have been shown to be sufficient for Opa1 cleavage (314,315,329). We replicated these findings using H_2O_2 treatment, which induced significant Opa1 processing in an Oma1-dependent manner. We additionally found that mROS production was increased in response to polarizing agents. Critically, the Opa1 processing

phenotypes of H_2O_2, rotenone, and FCCP could be rescued by pre-treatment with the antioxidant N-acetyl cysteine (NAC). These results demonstrate a novel dependence of Oma1 activation on oxidative stress. Work in yeast has demonstrated that Oma1 stability and substrate interaction is influenced by redox-sensitive cysteine residues in the mitochondrial intermembrane space (330,331). However, there are marked differences in the C-terminal domains of yeast and mammalian Oma1 (314), therefore, the mechanism by which mammalian Oma1 responds to redox changes is unclear. NAC pretreatment did not rescue oligomycin-induced Opa1 cleavage, further suggesting that Oma1 activation is multidimensional and likely not dependent on a singular aspect of mitochondrial stress.

Oma1 differentially influences mitochondrial fission and fusion

As a mediator of Opa1 structure and function, Oma1 plays an important role in the regulation of mitochondrial fission and fusion. To probe how Oma1 and subsequent Opa1 isoform patterns influence the mitochondrial dynamics response to stress, we analyzed mitochondrial morphology in WT and Oma1 KO HT22 cells. Because Oma1 KO cells have preserved L-Opa1 protein after stress, we hypothesized that they would be better equipped to handle mitochondrial fragmentation. However, KO cells produced more fragmentation after FCCP and oligomycin treatment compared to WT cells. These findings suggest that Oma1 and/or S-Opa1 protein are important for the acute response to stress. Oma1 serves to process/degrade other critical mitochondrial proteins that may be mediating these effects, namely DELE1. Oma1 has been demonstrated to cleave the protein DELE1 to allow for its translocation back to the cytosol for integrated stress response activation and downstream signaling (145,313). It is unlikely that the lack of S-Opa1 protein additionally contributed to mitochondrial stress, as others have demonstrated that Oma1-produced S-Opa1 isoforms are detrimental to mitochondrial health (88). Although it is possible that release of S-Opa1 from mitochondria may be required for certain stress response pathways (329).

Recovery from mitochondrial fragmentation was equal in both WT and Oma1 KO cells after FCCP washout. This finding was again contrary to our hypothesis that preserved L-Opa1 would be beneficial in the response to stress. However, the FCCP+washout condition did not accurately isolate a L-Opa1 deficient condition. During the washout period, biogenesis of new proteins produced a small amount of L-Opa1. Therefore, we treated cells during the washout period

with CHX to inhibit protein translation. CHX interestingly stimulates mitochondrial hyperfusion through an unknown mechanism (79,323). The washout with CHX condition in WT cells therefore allowed us to probe if L-Opa1 was necessary for mitochondrial fusion. Indeed, we found that WT cells with CHX during washout failed to perform fusion, whereas their Oma1 KO counterparts were successful. This experiment demonstrates that the preservation of L-Opa1 due to Oma1 KO is beneficial for the fusion recovery after mitochondrial fragmentation. Further, biogenesis of new L-Opa1 is necessary for fusion after complete L-Opa1 cleavage.

Oma1 has been extensively studied as a potential therapeutic target in many injuries/diseases. The identified dual roles for Oma1 in the fission/fusion response to stress adds nuance and context to the discussion of Oma1 as a therapeutic target. Oma1 knockout/inhibition has been demonstrated to be protective in models of I/R injury, heart failure, and neurodegeneration (318,332,333). Conversely, Oma1 activity is protective in other contexts, including ataxia and myopathies (146,313,335). These differential results may be due to compound effects of Oma1 loss. Oma1-dependent activation of stress responses, to an extent, is likely beneficial for survival, whereas Oma1-induced Opa1 cleavage may be detrimental to cell health. Further study of Oma1 activation and substrate-specific mechanisms is needed to understand how Oma1 influences mitochondrial responses to and recovery from stress.

Conclusions

Our findings highlight the multiplexed role of Oma1 and Opa1 processing in mitochondrial dynamics and the response to stress. We demonstrate Oma1 sensitivity to multiple mitochondrial stresses and variable dependence on oxidative stress for activation. This suggests an ability of mammalian Oma1 to respond to redox changes in the mitochondrial environment. Further work is required to disentangle the influences and interactions of mitochondrial stress components (e.g. membrane potential, ROS, ATP) in Oma1 activation and the downstream consequences on mitochondrial fission, fusion, and stress signaling pathways.

4.4 Methods and Materials

Animals

All procedures were performed in accordance with institutional guidelines and approved by the University of Michigan Institutional Animal Care and Use Committee (IACUC). Mice were

maintained on a 12 h light/dark cycle with standard rodent chow and water available ad libitum. Wild-type (WT) mice (C57BL/6J) were purchased from The Jackson Laboratory (Bar Harbor, ME).

HT22 Cell Culture

HT22 cells (immortalized mouse hippocampal neuronal cell line) were a generous gift from Dr. David Schubert (The Salk Institute, La Jolla, CA). Cells were maintained in Dulbecco's Modified Eagle Medium (DMEM; Invitrogen, 11995065) with 10% fetal bovine serum (FBS; Sigma-Aldrich, F2442), and incubated in 10% CO_2 at 37°C. Cells were passaged using 0.25% Trypsin (Invitrogen, 25200056) and kept below 70% confluency, not exceeding 7 passages (P7). Experiments were performed 12-18 hours after plating. Cells were exposed to 5μM oligomycin (Sigma, O4876), 3-10μM carbonyl cyanide 4-(trifluoromethoxy)phenylhydrazone (FCCP; SML2959), 20μM antimycin A (Sigma, A8674), 50μM H_2O_2 (FisherScientific, H325), 500μM histamine (Sigma, H7125), or 5μM cycloheximide (Sigma, C4859) for 2 hours prior to collection/fixation. Pre-treatment with 3mM N-acetyl cysteine (NAC; Sigma, A9165) was given for 1 hour prior to drug exposure.

CRISPR Gene Editing

Oma1 KO HT22 cells were generated using CRISPR-mediated mismatch repair. Cells underwent nucleofection (Lonza, Nucleofector Kit V, VCA-1003) with CRISPR RNA (5'-AAGAAAGUUUCUAGGCAGUA-3'), Oma1 forward primer 1 (5'-GCTTGTCCTGTTGAAGGTGC-3'), Oma1 forward primer 2 (5'-AATACATGTTTTCCACAGGTGTTT-3'), Oma1 reverse primer (5'-GGCCTCTATTACGGCAGGAC-3') and were administered Cas9 nuclease protein (Dharmacon, CAS11200). Clones were screened for mismatch repair by T7 endonuclease assay and Western blot was used to confirm loss of Oma1 protein.

Primary Neuron Culture

Cerebral cortices from postnatal day 0–1 (P0–P1) mouse pups were isolated and minced following decapitation. Tissue was incubated in enzyme digestion solution (Hibernate-A Medium (Gibco, A1247501), 1X B-27 supplement (Gibco, 17504044), 0.06 mg/mL L-cysteine (Sigma, 778672), 1.4×10^{-2} N NaOH (Sigma, 43617), 10 ng/mL APV (2-Amino-5-phosphonopentanoic

acid, Sigma, A-5282), 1:100 Papain (Worthington, LS 03126), 40µg/mL DNase I from bovine pancreas (Roche, 11284932001) for 30 min at 37 °C. Following digestion, tissue was washed with DPBS and dissociated in Hibernate-A medium with 1X B-27. Cell density was measured by hemocytometer and trypan blue staining. Cells were seeded 6-well dishes (1.5 x 10^6 cells/well). After 30 min, complete media change was performed with neurobasal complete medium (1x Neurobasal Plus medium (Gibco, A3582901), 1X B-27 Plus supplement (Gibco, A3653401), 0.5 mM Glutamax Supplement (Gibco, 35050061), and 1% Penicillin/Streptomycin Solution (Gibco, SV30010)). Cells were incubated at 37 °C with 5% CO2 for 14 days. Half-media changes were performed every 3–4 days with neurobasal complete medium.

Oxygen-Glucose Deprivation and Reoxygenation (OGD/R)

Oxygen-glucose deprivation was performed in O_2 Control In Vitro Glove Box (Coy Lab Products). The chamber was maintained at <0.1% O_2 and 5% CO_2. EBSS without glucose was bubbled in the hypoxic chamber with 95% N_2 and 5% CO_2 gas for 60 min for deoxygenation. Cells were placed inside the chamber and washed 3x with deoxygenated EBSS and allowed to incubate for 90 min. Cells were then removed from the chamber and reoxygenated with Neurobasal Plus medium with 1X B-27 minus antioxidants (Gibco, 10889038) and incubated at 37 °C in 5% CO_2. Control cells remained at normoxic conditions, were washed 3X EBSS with glucose, and changed to Neurobasal Plus medium with 1X B-27 minus antioxidants after 90 min.

Western Blot

Cells were scraped in homogenization buffer (10mM HEPES (MilliporeSigma, H-4034), 1mM EDTA (ThermoFisher, J15694-AP), 1mM EGTA (MilliporeSigma, 324626), 100mM KCl (Calbiochem, 7300), 210mM D-Mannitol (MilliporeSigma, M4125), 70mM Sucrose (MilliporeSigma, S0389), 1x Halt Protease & Phosphatase Inhibitor (Fisher Scientific, 78444) in ddH_2O) and lysate was collected on ice. Samples were then sonicated and protein concentration was measured using the Bradford Plus Assay Reagent (ThermoFisher, PI23236). Polyacrylamide gels (7.5% and 4-20% 29:1 polyacrylamide/bisacrylamide (Fisher BioReagents, BP1408-1), 375 mM Tris pH 8.8 (Fisher BioReagents, BP152-1), 0.1% sodium dodecyl sulfate (SDS, Sigma, L3771), 0.1% ammonium persulfate (APS, Sigma, #A3678), and 0.1% TEMED (GE Healthcare, # 45-000-226)) were loaded with 5-10µg of whole cell lysates and transferred to nitrocellulose membranes. Membranes were incubated with primary antibodies (1:1000 Rabbit Anti-Beta Actin

(Cell Signaling, 4967L); 1:1000 Mouse Anti-HSP60 (BD Transduction Laboratories, 611562); 1:200 Mouse Anti-Oma1 (Santa Cruz, sc-515788); 1:1000 Mouse Anti-Opa1 (BD Transduction Laboratories, BD612607)) at 4 °C overnight. Membranes were washed 3x with Tris-Buffered Saline and 0.1% Tween (TBST, Fisher Scientific, BP337500) and incubated in secondary antibodies (1:5000 Donkey Anti-Mouse (Jackson Immuno Research Labs, 715-035-150 or 1:10,000 Donkey Anti-Rabbit (Jackson Immuno Reserach Labs, 711-035-152) for 60 min at RT. All antibodies were prepared with 2% BSA in TBST unless otherwise specified. Membranes were then washed 3x with TBST. Membranes were incubated in SuperSignal West Pico Plus Chemiluminescent Substrate (ThermoFisher, 34577) and imaged with iBright 1500 imager (Invitrogen) and quantified by densitometry using FIJI.

Flow Cytometry

Mitochondrial superoxide levels were assayed by flow cytometry using MitoSOX Red (FisherScientific, M36008). HT22 cells were treated with the indicated drugs for 30 min and trypsinized to suspension. Cells were centrifuged and resuspended in Hanks' balanced salt solution (HBSS) no phenol red (FisherScientific, 14025092) and 5μM MitoSox Red. Cells were then allowed to incubate at 37°C for 30 min with gentle rocking. Cells were centrifuged and washed with HBSS twice.

For mitochondrial membrane potential assessment, TMRM (Millipore Sigma, T5428) was used per manufacturer's instructions. Cells were then trypsinized, centrifuged, and resuspended in HBSS with TMRM (15nM). Cells were allowed to incubate for 30 min before adding the indicated drugs. Flow was performed 30 min following drug treatment.

For both MitoSOX and TMRM experiments, DAPI (1μg/mL; FisherScientific, D1306) was added and used as a viability marker. Cells were analyzed via flow cytometry on a Bio-Rad ZE5 Cell Analyzer. Cells were gated by forward and side scatter to isolate single intact cells. DAPI-negative cells were analyzed for TMRM or MitoSOX Red signal. Flow cytometry analysis was performed using FlowJo™ v10.8.1 Software (BD Life Sciences).

Immunofluorescence & Fluorescent Microscopy

HT22 cells were plated on glass 12mm coverslips. The day after plating, cells were treated for 2-4 hours with the indicated drugs. Coverslips were washed with DPBS and fixed with 4%

paraformaldehyde (Fisher Scientific, 50980487) for 15 min at 37 °C. Following fixation, cells were washed 3x with DPBS and stored at 4 °C. For immunofluorescent staining, coverslips were incubated in blocking solution (5% goat serum (Sigma, G9023) and 0.3% Triton-X100 (Acros Organics, 215682500) in PBS) for 60 min. Coverslips were then incubated in primary antibody solution (1:1000 Mouse Anti-ATPB (Abcam, ab14730), 1% BSA (Sigma, A9647) and 0.3% Triton-X100 in PBS) at 4 °C overnight. Coverslips were then washed 3x in PBS and incubated in secondary antibody solution (1:200 Goat Anti-Mouse Alexa Fluor 488 (Invitrogen, A11029), 1% BSA (Sigma, A9647) and 0.3% Triton-X100 in PBS) for 60 min. Coverslips were mounted on glass slides using Fluoroshield with DAPI (Sigma, F6057) after 3x washes with PBS.

Cells were imaged via Zeiss Axio Observer Z1 inverted microscope with LED illumination. For each coverslip, 5-6 image z-stacks (0.24 μm slices) were acquired at 63x magnification with oil immersion. Z-stacks were processed using Zeiss Zen Pro extended depth of focus wavelets method. Images were exported in TIFF format for post-processing.

Mitochondrial Morphological Analysis

Mitochondrial morphology was analyzed as previously described (47). Briefly, compressed z-stack TIFFs of ATPB signal were imported into FIJI (65). Images were converted to 8-bit and background was subtracted with a rolling ball radius of 10 pixels. Discrete mitochondrial objects were segmented using the Trainable Weka Segmentation plug-in (66). Segmented images were converted to binary and 32 size/shape measurements were taken from each mitochondrial object (67). Measurements were input into a trained random forest algorithm in RStudio (RStudio, PBC, Boston, MA) for classification to one of four morphologies: network, unbranched, punctate, swollen. Each object was classified and percent mitochondrial area for each morphology was calculated per experimental replicate.

Statistical Analysis

Statistical analyses were performed in GraphPad Prism 8 (GraphPad Software, San Diego, CA). For comparisons of more than two experimental groups of the same genotype, one-way ANOVAs were performed with post-hoc comparisons between each experimental group and the control condition. Correction for multiple comparisons was evaluated by Dunnett's test. For comparisons between two discrete groups (e.g. genotype, NAC treatment) across multiple

experimental conditions, two-way ANOVAs were performed with post-hoc comparisons made by Sidak's test corrected for multiple comparisons. Tests with $p < .05$ were considered statistically significant. For primary neuron experiments, n denotes biological replicates. For HT22 cell experiments, n denotes experimental replicates.

4.5 Figures

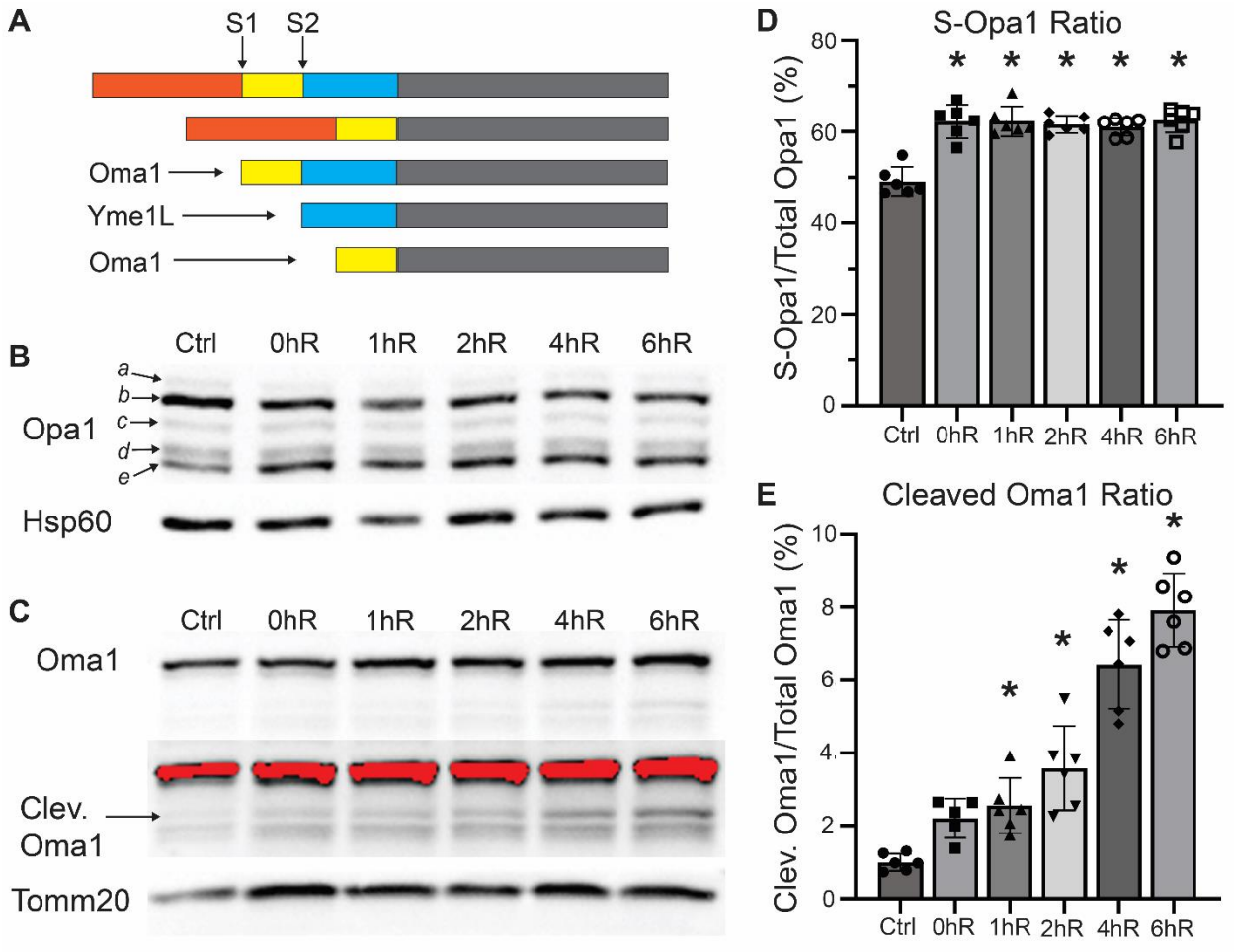

Figure 4-1. Opa1 and Oma1 processing initiate during OGD

(A) Graphic demonstrating the five main protein bands of Opa1 in neuronal cells. Bands *a* and *b* represent splice variants of full-length protein (L-Opa1). Protease Oma1 and Yme1L cleave L-Opa1 at sites S1 and S2, respectively to create short proteins (S-Opa1). (B) Representative Western blot of Opa1 processing during primary neuron OGD/R. Arrows point to each Opa1 protein band. (C) Representative Western blot of Oma1 and cleaved Oma1 during OGD/R. The cleavage band is visible after high exposure of the full length Oma1 band. Note that red overlay represents saturated full-length protein. (D) Quantification of Opa1 cleavage during OGD/R. n=6 biological replicates. (E) Quantification of Oma1 cleavage during OGD/R. n=6 biological replicates. *$p < 0.05$ vs controls

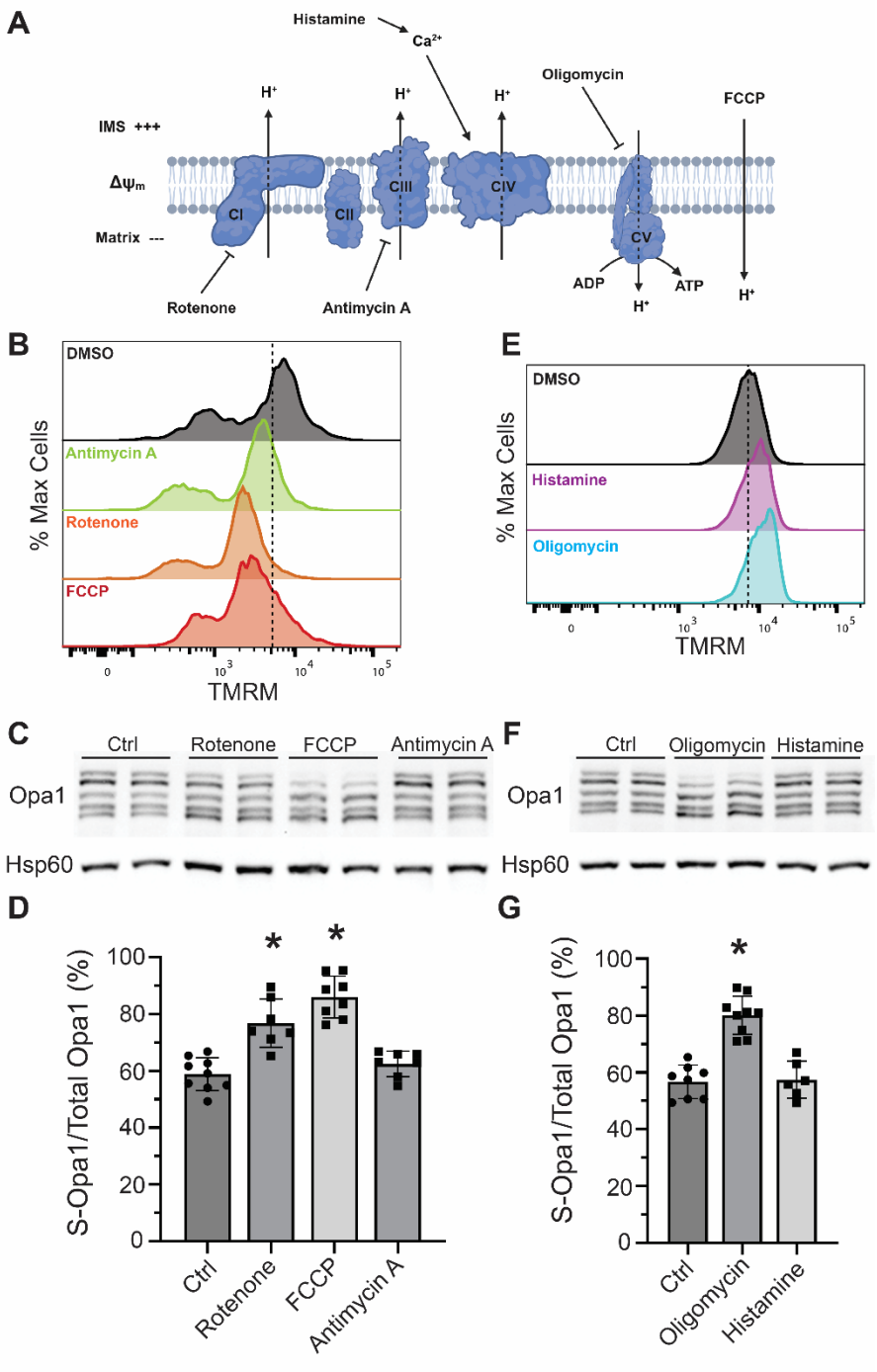

Figure 4-2. Opa1 processing is sensitive to both depolarization and hyperpolarization

(A) Graphic demonstrating the site-specific actions of chemicals used to alter mitochondrial membrane potential. (B) Representative flow cytometry histograms of HT22 cells with TMRM demonstrating depolarization. Dotted line denotes DMSO median. (C) Representative Western blot of Opa1 after treatment with depolarizing agents. (D) Quantification of Opa1 processing with depolarization treatment. n=7-9 experimental replicates. (E) Representative flow cytometry histograms of HT22 cells with TMRM demonstrating depolarization. Dotted line denotes DMSO

median. (F) Representative Western blot of Opa1 after treatment with hyperpolarizing agents. (G) Quantification of Opa1 processing with hyperpolarization treatment. n=6-9 experimental replicates. *$p < 0.05$ vs controls

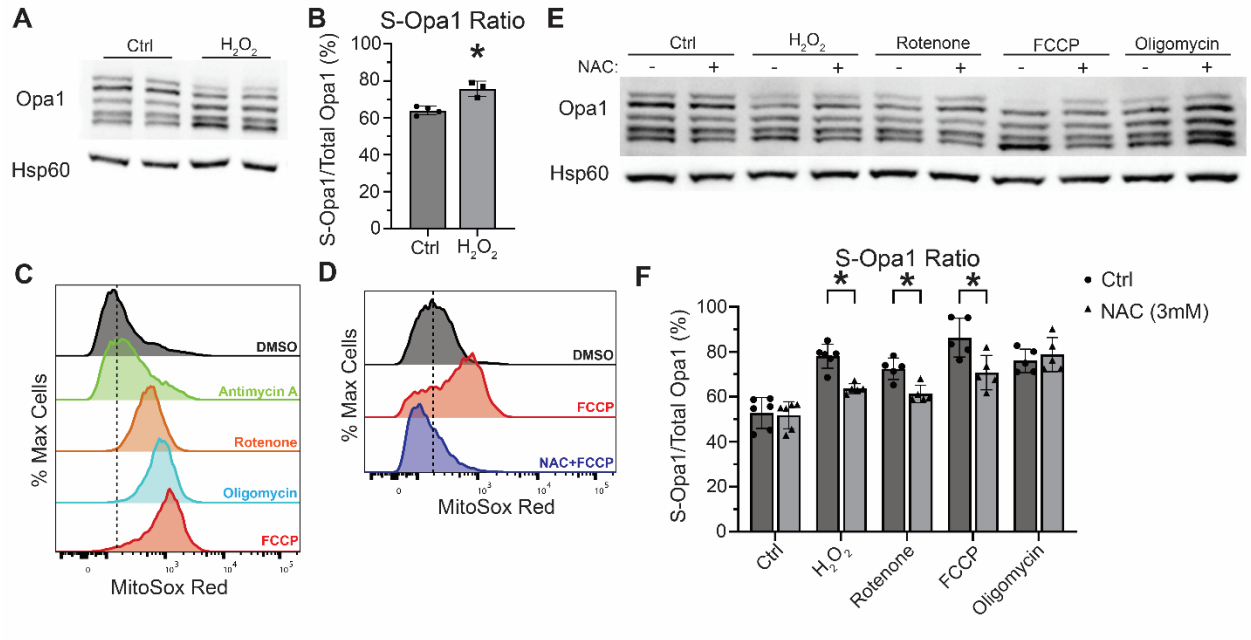

Figure 4-3. Opa1 processing is partially dependent on oxidative stress

(A) Representative Western blot of Opa1 after 2hr treatment with 50μM H_2O_2. (B) Quantification of Opa1 processing after H_2O_2 treatment. n=3-4 experimental replicates. (C) Representative flow cytometry histograms of HT22 cells with MitoSOX Red demonstrating production of mitochondrial reactive oxygen species (mROS). Dotted line denotes DMSO median. (D) Representative flow cytometry histograms of HT22 cells with MitoSOX Red demonstrating mROS scavenging by NAC. Dotted line denotes DMSO median. (E) Representative Western blot of Opa1 following drug treatment with and without pre-treatment of antioxidant NAC. (F) Quantification of Opa1 processing in NAC experiments. n=5-6 experimental replicates *$p < 0.05$ between controls and NAC.

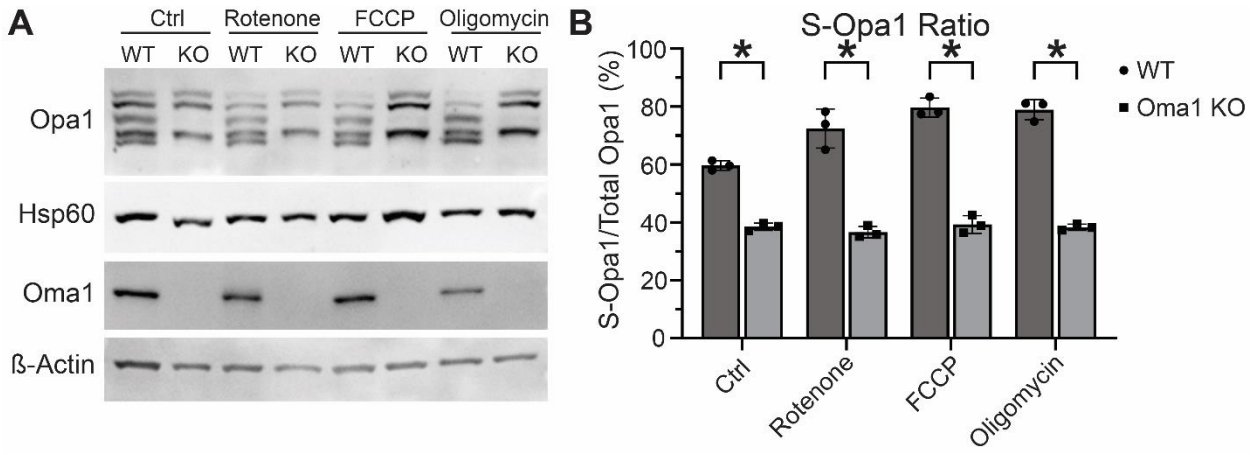

Figure 4-4. Stress-induced Opa1 processing is dependent on Oma1

(A) Representative Western blots of Opa1 and Oma1 in WT and Oma1 KO HT22 cells with drug treatment. (B) Quantification of Opa1 processing in WT and Oma1 KO cells after drug treatment. n=3 experimental replicates. *$p < 0.05$ between WT and KO.

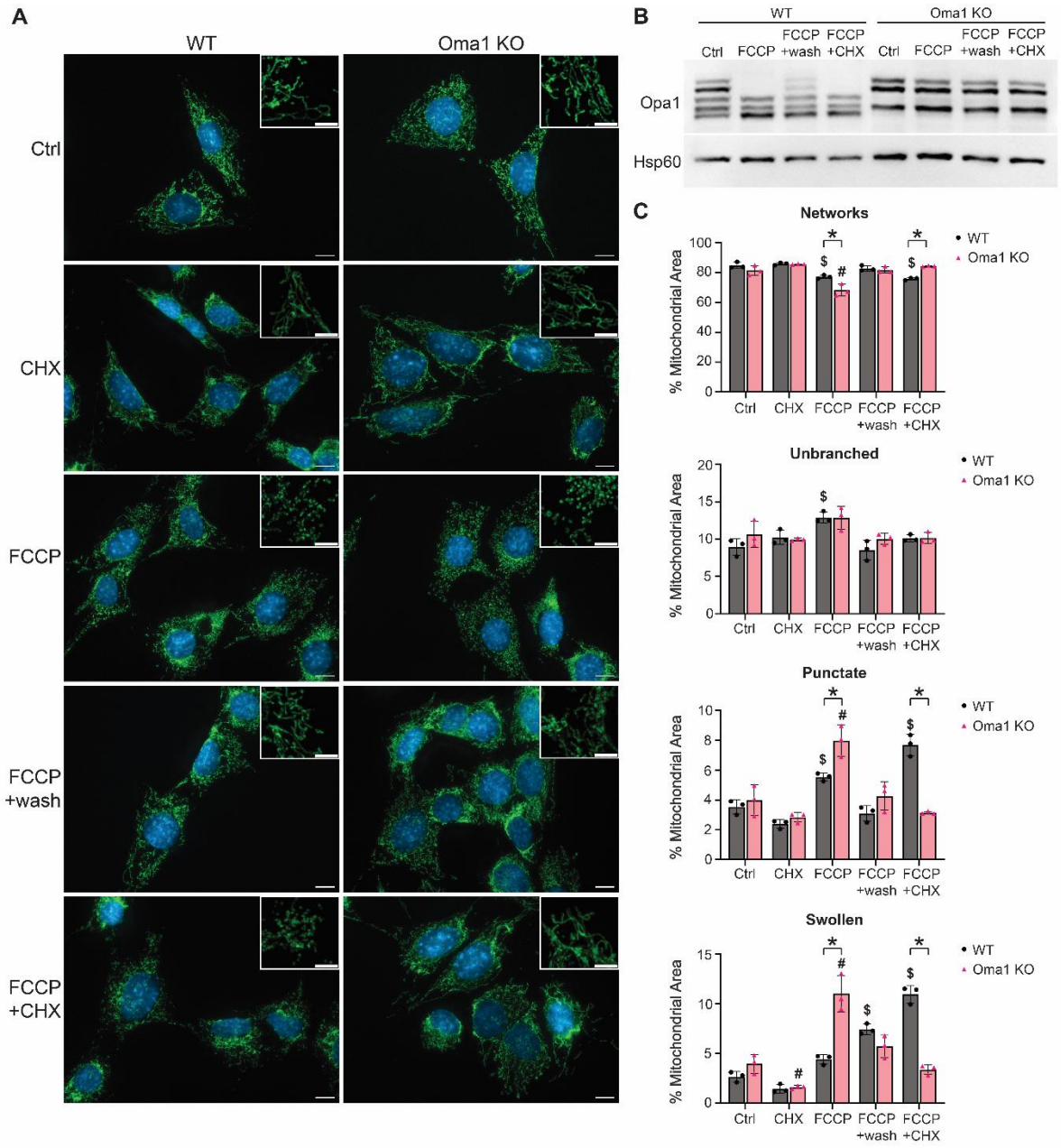

Figure 4-5. Oma1 has dual roles in mitochondrial dynamics during response to stress

(A) Representative micrographs of immuno-labeled ATP synthase (green) after 2 hours of treatment with cycloheximide (CHX), FCCP, FCCP + 2 hour washout, FCCP + 2 hour washout with CHX. Scale bar = 10μm. Insert: magnified view of mitochondrial morphology, scale bar = 5μm. (B) Representative Western blot of Opa1 and Oma1 in FCCP and CHX conditions. (C) Quantification of mitochondrial morphology during FCCP and CHX experiments. Proportions of mitochondrial area are displayed for each of the four distinct morphologies: networks, unbranched, punctate, swollen. n=3 experimental replicates. *$p < 0.05$ between WT and KO; $^{\$}p<0.05$ vs WT control; $^{\#}p<0.05$ vs KO control.

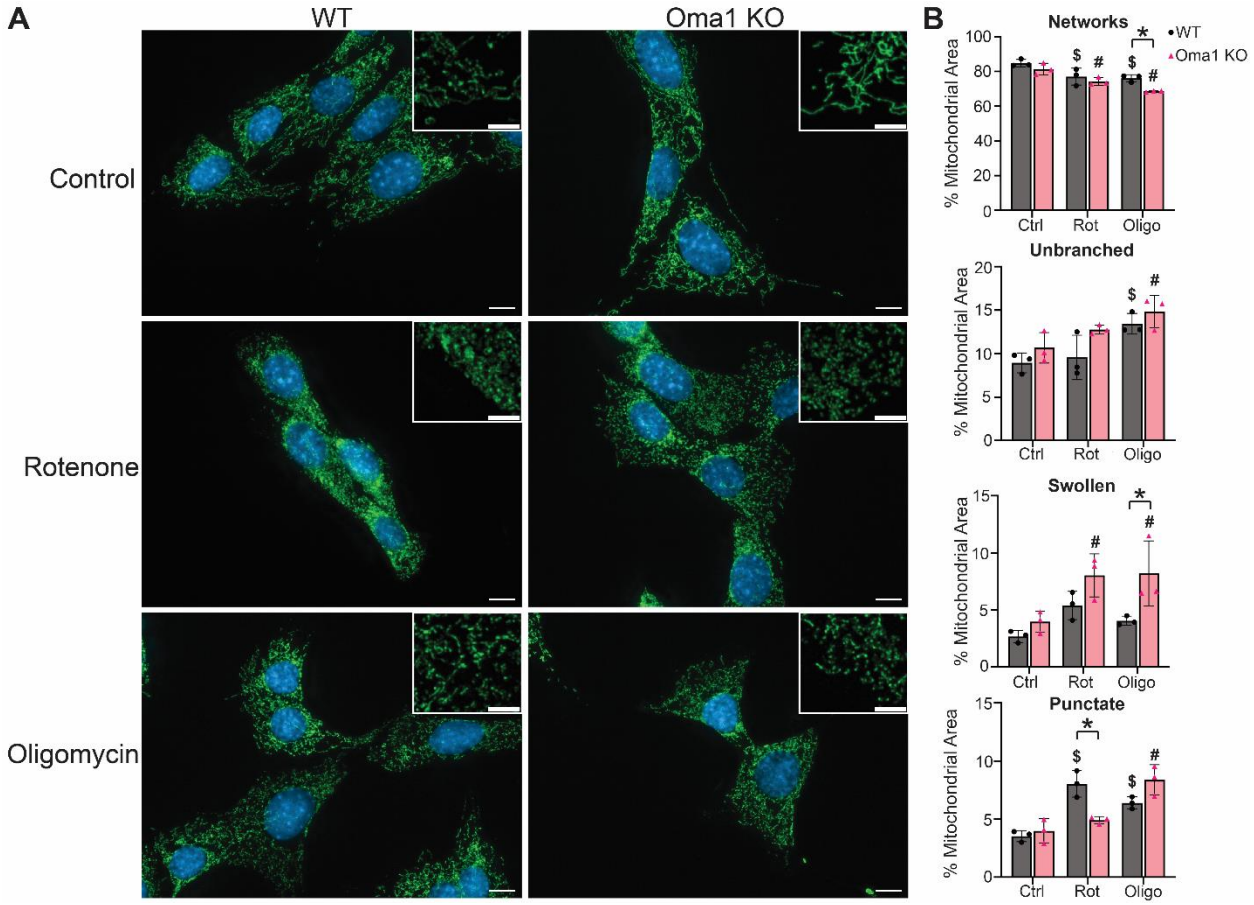

Figure 4-6. Oma1 KO morphology after rotenone and oligomycin treatment

(A) Representative micrographs of immuno-labeled ATP synthase (green) after 2 hours of treatment with rotenone or oligomycin. Scale bar = 10μm. Insert: magnified view of mitochondrial morphology, scale bar = 5μm. (B) Quantification of mitochondrial morphology during rotenone and oligomycin experiments. Proportions of mitochondrial area are displayed for each of the four distinct morphologies: networks, unbranched, punctate, swollen. n=3 experimental replicates. *$p < 0.05$ between WT and KO; $^{\$}p<0.05$ vs WT control; $^{\#}p<0.05$ vs KO control.

Chapter V: Agent-based Modeling of Neuronal Mitochondrial Dynamics using Intrinsic Variables of Individual Mitochondria [4]

5.1 Introduction

Having developed a methodology for analyzing the morphology of single mitochondrion and additionally demonstrating that mitochondrial membrane potential and oxidative stress can modulate mitochondrial dynamics machinery, we culminated a system to evaluate dynamics and intrinsic variables of single mitochondria.

Computational modeling of biological mechanisms is a growing field as access to software and resources, along with computer literacy, has significantly increased in recent years. *In silico* experimentation with models of biological systems allows for hypothesis testing and predictive modeling for optimization of experimental design. The predictive power of computational models is particularly valuable for designing preclinical and clinical trials (336-338). Subject, budgetary, and logistical limitations often complicate the ideal design of therapeutic trials. For example, it is not feasible to test greater than 5-10 possible dosing strategies in a single study while maintaining statistical power and feasibility. Predictive models can be leveraged to identify the therapeutic strategies with the best possible chances of success prior to (pre)clinical trials, therefore minimizing cost, streamlining trial execution, and limiting potential harm.

The complexities of mitochondrial biology have been modeled using mathematical and systems-level techniques (339-343). Various modeling approaches (e.g. ordinary differential equations, boolean networks) have been utilized to model mitochondrial dynamics on the order of cells and organisms (344-348). Because cells and organelles, like mitochondria, are discrete objects with innate abilities to perform certain functions, agent-based modeling is an optimal methodology to create a working model of mitochondrial behavior (349). Agent-based models are

[4] This chapter is composed of the submitted manuscript: "Fogo GM, Anzell AR, Sanderson TH. Agent-based modeling of neuronal mitochondrial dynamics using intrinsic variables of individual mitochondria. *Submitted*.". I performed all detailed experiments.

comprised of individual agents that have given rule sets to perform actions and interactions. These micro-rule sets can give rise to macro-level patterns of the entire system. Several groups have composed agent-based models of mitochondrial dynamics yielding insights into the crosstalk of dynamics with motility, mitophagy, and aging (346,350,351).

The aim of the present study was to identify the relationships between intrinsic variables of individual mitochondria and fission/fusion behavior. To this end, we analyzed the size, shape, mitochondrial membrane potential, and protein oxidation level of mitochondria undergoing fission and fusion in mouse primary neurons. We synthesized our findings into an agent-based model of mitochondrial dynamics, called the **Mi**tochondrial **Dy**namics **S**imulation (**MiDyS**). Further, we illustrate the potential utility of MiDyS for *in silico* experimentation with simulated ischemia/reperfusion (I/R) injury and therapeutic intervention.

5.2 Results

5.2.1 Dynamic mitochondria have distinct intrinsic properties

To investigate the relationships between intrinsic properties of individual mitochondria and their behavior, we utilized live cell microscopy with fluorescent mitochondrial labeling. The size and shape of individual mitochondria is the result of mitochondrial fission and fusion. The size, shape, and proximity of mitochondria also directly influence the processes of mitochondrial dynamics. Mitochondrial membrane potential ($\Delta\Psi$) is the electrochemical gradient formed across the mitochondrial inner membrane that is critical for oxidative phosphorylation and has been shown to influence the balance of mitochondrial dynamics (352,353). Therefore, we labeled mitochondria in mouse primary cortical neurons with 30nM MitoTracker Deep Red (MTDR). MTDR is a fluorescent dye whose uptake to the mitochondrial matrix is dependent on the mitochondrial membrane potential, allowing analysis of mitochondrial morphology and mitochondrial membrane potential (354,355). Mitochondrial networks were imaged every 60 seconds over a period of 30 minutes to capture dynamic changes and the corresponding relative mitochondrial membrane potential (Fig. 5-1A). Image sequences were then analyzed for identification of mitochondrial fission and fusion events using ROI-based automated detection script in FIJI (213). If a mitochondrial object was detected to perform fission or fusion between $frame^{n-1}$ and $frame^{n}$, the mitochondrial object would be tagged and measurements would be taken

from frame^{n-1} (Fig. 5-1B). Area distribution was analyzed to reflect mitochondrial size, aspect ratio for mitochondrial shape, and MTDR signal for relative mitochondrial membrane potential of each mitochondrial object undergoing fission, fusion, and objects that remained unchanged. A total of 105,958 mitochondrial objects were analyzed, with 29,627 and 15,386 objects undergoing fusion and fission, respectively. MTDR mean intensity within mitochondrial objects remained stable throughout the recording periods (Fig. 5-1C). We observed a balance between fusion (18.18%) and fission (16.62%) events (quantified as percentage of total mitochondria), with slight favor to fusion during MTDR recordings (Fig. 5-1D).

Mitochondrial fission and fusion have been proposed to organize mitochondrial proteostasis, mitochondrial DNA nucleoids, and ultrastructure (82,356,357). We sought to determine if mitochondrial protein status altered dynamics. We therefore crossed Thy1-Cre (358) mice with conditional MitoTimer mice for neuron-specific expression of MitoTimer protein (267,268). MitoTimer is a designer protein that fluoresces green when newly synthesized and trafficked to the mitochondrial matrix. Oxidation of MitoTimer, whether over time or due to oxidative stress, causes an irreversible shift in fluorescence to red. The MitoTimer red/green ratio therefore is an indicator of the balance between new and old/oxidized protein within the mitochondria (267,268). Live cell recordings were taken of MitoTimer-expressing primary neurons over 30 minutes. MitoTimer neurons were imaged every 120 seconds over this period to limit photobleaching. MitoTimer recordings were then analyzed for fission and fusion events (Fig. 5-1E,F). Similar to MTDR recordings, mitochondrial fluorescence remained stable over time with a balance of fusion (14.26%) and fission (11.49%) events (Fig. 5-1G,H). A total of 20,437 MitoTimer-expressing mitochondria were analyzed with 1,963 fission and 3,208 fusion-tagged objects.

The distribution of intrinsic variables was assessed across 3 groups of labeled mitochondria: stable, fission, and fusion. Mitochondrial area was found to be differentially distributed among the three groups. Fission objects had a shift towards larger mitochondrial area (6.924±12.82μm), while the fusion group (1.772±3.099μm) demonstrated a wider variability of area compared to stable mitochondria (2.575±6.304μm) (Fig. 5-2A). This finding appears logical as parent mitochondria must be large enough to produce two viable daughter mitochondria when undergoing fission, whereas fusion can be performed by even the smallest viable mitochondrial

object. Aspect ratio (AR), the ratio between the longest (major) and shortest (minor) axis of an object's fitted ellipse, was similar between stable (2.881±1.916) and fusion objects (2.836±1.862). However, fission objects had a shifted AR distribution (4.219±2.614), indicating a higher likelihood of long linear objects in that group (Fig. 5-2B). MTDR signal was quantified as the mean intensity of MTDR within each mitochondrial object relative to the mean intensity of the entire image. Mitochondria from all three groups had similar central values of MTDR intensity, however, fission and fusion objects were more likely to have MTDR values near the outer limits of the distribution (Fig. 5-2C). This data suggests mitochondrial membrane polarization outside of the baseline range is associated with dynamic behavior. In MTDR recordings, MTDR relative intensity did not have strong correlations with any size or shape descriptors (Fig. 5-2D). The distribution of MitoTimer ratio in analyzed mitochondria was a non-normal distribution in all three groups. Distributions for stable (0.2620±0.1050) and fission objects (0.2829±0.1047) appeared to follow a sum of two gaussian distributions. Fusion mitochondria were more distributed on the higher end of MitoTimer ratio (0.3341±0.1165), suggesting that fusion is associated with older or more oxidized proteins (Fig. 5-2E). Similar to MTDR, MitoTimer ratio did not correlate strongly with other variables (Fig. 5-2F). Our results from primary neuron recordings identify distinct features of mitochondria prior to fission and fusion, wherein fission mitochondria are more likely to be larger linear objects and fusion mitochondria are more likely to have altered protein oxidation levels. Additionally, fusion and fission mitochondria are more likely than stable mitochondria to have membrane potentials that deviate from a normal range.

5.2.2 Prediction of mitochondrial fission/fusion events

Due to the distinct properties of fusion and fission mitochondria, we evaluated our ability to predict mitochondrial behavior using measured intrinsic values. During our recordings, we identified many mitochondrial objects that could perform fusion and fission within the 60-120 second intervals, therefore, we decided to split our predictions into stable vs. fusion and stable vs. fission, rather than a three-way decision. The overlapping fluorescent spectra between the red MitoTimer and MTDR, did not allow us to record data of both reporters from the same mitochondria. This led us to generate two separate prediction models for each reporter. Multiple logistic regression was performed on stable, fission, and fusion mitochondria with mitochondrial area, major, minor, AR, and MTDR or MitoTimer as the inputs with stable being the negative

outcome and fission or fusion being the positive outcome. Prediction fission from MTDR and MitoTimer data produced ROC curves with area under the curve (AUC) of 0.7926 and 0.8485, respectively (Fig. 5-3A,E). Both regressions produced similar predicted probability distributions with high negative predictive power (Fig. 5-3B,F). Fusion regressions had lower AUC values (0.6497 & 0.7370) and less negative predictive power (Fig. 5-3C,D,G,H). Fusion prediction was predicted to be more difficult as the behavior of two or more mitochondria must be predicted, compared to fission which requires only one parent mitochondria.

5.2.3 Agent-based model of mitochondrial dynamics

Agent-based models utilize rulesets given to individual autonomous agents, wherein the actions and interactions of the agents produce the dynamics of the overall simulated network/environment. We applied our data from individual mitochondria and logistic regressions to construct an agent-based model of mitochondrial dynamics in NetLogo, an open-source agent-based modeling program (359). Our model, called MiDyS, is composed of a single cell simulation environment with agents representing the smallest measured mitochondrial objects. Agents (circles) in the simulation can move and perform interactions with other agents to model dynamic behavior. Agents create and destroy fusion links with other agents to simulate mitochondrial fusion. Alternatively, fission is modeled by the loss of a link between two agents to form two smaller objects. The number of agents in the simulation is controlled by simulated biogenesis (growth of new linked agent from parent agent) and mitophagy (loss of unlinked agent). Each agent can perform any of these four functions, each interval simulating 1min of time progression (Fig. 5-4A). The MiDyS simulation environment represents a single cell (2500μm^2) made up of 50x50 patches of 1x1μm^2 (Fig. 5-4B). Mitochondrial agents are each 0.5μm^2 in size and have encoded intrinsic properties, including membrane potential and MitoTimer ratio. When an agent creates a fusion link with another agent, those agents represent a continuous mitochondrial agent, therefore size and shape parameters are measured by mitochondrial object. Conversely, membrane potential and MitoTimer ratio are not equilibrated across mitochondrial objects and are rather localized to the individual agents within an object. This mirrors the spatial restriction of membrane potential and protein homeostasis observed in cells (248,360-362). The NetLogo interface of MiDyS allows for precise control of starting parameters including number of agents and initial networking density on the left side of the interface. The simulation window is located in the center

of the interface for visualization of mitochondrial dynamics. Custom output plots and monitors on the interface allow real-time and exportable data analysis of global and agent-specific parameters (Fig. 5-4B).

The fission and fusion actions of agents are determined by the multiple logistic regression equations derived from *in vitro* neuron data. Intrinsic values of mitochondrial agents are input to the regression model and the result represents the probability of fission/fusion. After calculation, each agent runs probability checks for fission and fusion, giving rise to the stochastic agent-based dynamics of MiDyS. Because two regression models were generated for both fusion and fission, agents perform both calculations and keep the larger value. The processes of mitochondrial biogenesis and mitophagy were not directly evaluated in our *in vitro* recordings, and therefore we used assumed rates based on literature review and other models (273,346,351). Biogenesis occurs at a rate of 5% for agents that fall within the baseline range of membrane potential, due to import of new protein in mitochondria being dependent on mitochondrial membrane potential (110,363). Mitophagy occurs at a rate of 10% for agents that have no links, this assumption is based on previous data from our group showing that mitophagy in primary neurons heavily favors mitochondrial objects $< 1\mu m^2$ in area (273). Simulations over time in MiDyS present stable balances of fusion and fission events over time with visualization of individual dynamics events and micro-interactions between agents (Fig. 5-5).

5.2.4 Simulated ischemia/reperfusion injury alters mitochondrial dynamics

One of the goals for MiDyS was to demonstrate the utility of agent-based modeling for *in silico* experimentation. MiDyS was therefore encoded with the ability to manipulate key intrinsic variables of the agents. Sliders on the interface allow users to manipulate the membrane potential and MitoTimer ratio by defined increments over time. This allows users to simulate disease/injury models of interest associated with oxidative stress and/or depolarization/hyperpolarization. Cerebral I/R injury injury is a leading cause of death and disability, as well as a known effector of oxidative stress, mitochondrial membrane potential, and mitochondrial dynamics (34,42,364,365). We therefore set out to simulate neuronal I/R injury in MiDyS. There are several leading models of mitochondrial membrane potential and oxidative stress temporal dynamics considered in I/R. We tested the outcomes of three models differing in the timing of mitochondrial membrane potential and reactive oxygen species (ROS) production: ischemia-induced ROS (23,366,367),

hyperpolarization-induced ROS (34,39,368), and reperfusion-induced ROS (28,90) (Fig. 5-6). We found that simulated ischemia in all three models produced extensive mitochondrial fragmentation and reduced fusion probability. Mitochondrial fission was inhibited in all models upon reperfusion, but fusion increased only in the hyperpolarization-induced ROS model. Late-stage reperfusion then induced a secondary phase of mitochondrial fission in the hyperpolarization-induced ROS model. This temporal pattern of ischemia-induced fission, early fusion during reperfusion, and secondary fragmentation matches previous observations of neuronal mitochondrial dynamics following I/R (Chapter II; 85,151) (Fig. 5-6). The changes in mitochondrial membrane potential of the hyperpolarization-induced ROS model were reduced to keep values within physiological range, and the pattern of fusion and fission remained consistent (Fig. 5-7). The balance of mitochondrial fission and fusion in MiDyS is quantified by the fission/fusion index (FFI), ranging from -1 (complete fission) to 1 (high fusion) (Fig. 5-7).

5.2.5 In silico experimentation defines therapeutic window of antioxidants

With the establishment of a simulated I/R paradigm, we proceed to test a simulated preclinical trial. Historically, antioxidants have been leading candidates for therapeutic intervention during cerebral I/R injury (369-372). Because the extent of oxidative stress applied to agents can be simply adjusted in our model, we chose to simulate antioxidant therapy during simulated I/R injury. A critical issue in designing preclinical and clinical trials is the determination of discrete treatment groups. Dose, delivery strategy, and timing are all key variables that must be considered. Selection of inopportune variables can contribute to negative and/or misleading results. Predictive modeling and *in silico* experimentation with MiDyS and similar programs can aid these critical decisions by quantitatively comparing outcomes with different combinations of variables. To demonstrate this, we set out to determine the therapeutic window for antioxidant therapy in our simulated I/R model. Treatment of acute brain injuries require defined therapeutic windows, as minutes can separate distinct pathological mechanisms and render a therapy beneficial, inert, or even detrimental (373-376). We simulated application of antioxidant therapy (reduction of oxidative stress by 40%) at the onset of reperfusion to first demonstrate therapeutic efficacy. Antioxidant therapy preserved mitochondrial content and mitochondrial morphology through the inhibition of mitochondrial fission probability (Fig. 5-8A). Next, we delayed antioxidant treatment by 5, 10, 20, and 25 minutes to determine the therapeutic window. Delayed

treatments had incremental changes in total oxidation and provided diminishing returns of therapeutic effect on mitochondrial content and morphology (Fig. 5-8B,C). Simulated data suggests that antioxidant therapy loses rescue of mitochondrial content at 20 minutes of delay, and rescue of mitochondrial morphology at 25 minutes of delay. Utilizing these observations, one could make an informed decision about the cutoff time for enrollment of patients in a clinical trial of antioxidant therapy for cerebral I/R injury. These *in silico* experiments demonstrate the potential utility of MiDyS and similar predictive models for experimental and trial design.

5.3 Discussion

Mitochondrial dynamics have been associated with and implicated in numerous disease and injury models of the brain. The field requires an intimate knowledge of the key factors contributing to mitochondrial fission and fusion in order to target and treat these pathologies. As individual mitochondria are discrete organelles with their own genomes and proteomes, we set out to define the relationships between the intrinsic properties of individual mitochondria and their respective dynamic behavior. We found that larger linear mitochondria are more likely to undergo fission and mitochondria with older/more oxidized proteins are more likely to perform fusion. Additionally, deviation from the basal range of mitochondrial membrane potential is associated with dynamic events, including both fusion and fission. Leveraging our collected datasets, we generated an agent-based model of neuronal mitochondrial dynamics, termed MiDyS. Simulations in MiDyS present balanced mitochondrial networks capable of replicating temporal patterns of mitochondrial dynamics in neuronal I/R injury. Further, we illustrated the potential application of MiDyS for simulated (pre)clincal trials by testing the effects of delayed antioxidant therapy after I/R. We believe that MiDyS can be a framework for the study of mitochondrial dynamics *in silico* and development of future therapeutic strategies targeting mitochondria.

Our live cell imaging results suggest that objects undergoing mitochondrial fission tend to be larger and more linear than stable and fusing mitochondria. Logic tells us that fission into two daughter mitochondria would require a parent mitochondrial object at least double the minimum size of a mitochondrial object, which aligns with our data. Kleele et al. (44) describe a model for distinct mechanisms of mitochondrial fission based on scission location. Although not the primary target of the study, their data also demonstrates that larger daughter mitochondrial objects after fission are more likely to undergo fission than fusion. MitoTimer ratio was not found to be different

in fission mitochondria compared to stable mitochondria, although both populations demonstrated two peak populations of MitoTimer ratio, rather than a normal distribution. These two populations may be separated by location of the scission point, as Kleele et al. (44) additionally demonstrated that high mitochondrial ROS levels are associated with peripheral fission (fission near the end of the mitochondrial object) and not midzone fission. The lack of association between MitoTimer ratio and fission was surprising, as oxidative stress is a well demonstrated inducer of mitochondrial fission in many contexts (377-379). However, it is important to note that MitoTimer is not a specific or exclusive reporter of mitochondrial ROS levels (267,268). Krzystek et al. (380) additionally found that a highly red (oxidized) MitoTimer ratio is not an exclusive determinant of fission or mitophagy. Considering MitoTimer as an indicator of protein age, also suggests that mitochondrial fission is not influenced by protein dynamics. Mitochondria in dividing cells use fission to sort mitochondria by protein age (381), however, we did not analyze MitoTimer ratio in daughter mitochondria and therefore cannot conclude if this is also true in post-mitotic neurons.

Mitochondria on the outer bounds of the mitochondrial membrane potential spectrum displayed more incidence of dynamic behavior. Interestingly, the distribution of mitochondrial membrane potential was similar between fission and fusion objects. Treatment of cells with toxins causing mitochondrial depolarization (e.g. FCCP) and hyperpolarization (e.g. oligomycin) generally produce mitochondrial fragmentation (382-384). Because our recordings only included neurons at control conditions, it is likely that we only captured physiological levels of mitochondrial membrane potential. Our data suggests that in this range, fusion and fission are just as likely to occur, whereas treatment with mitochondrial toxins may push mitochondrial membrane potential to super physiological levels. Our data is contrasted by a previous study that demonstrated depolarized daughter mitochondria after fission are less likely to fuse than the more polarized daughter (184). It is unclear if this effect is only true in the acute phase after fission or universal. Fusion mitochondria were more likely to have higher MitoTimer ratios, indicating a greater abundance of oxidized protein compared to new protein. This data compliments the findings from Feree et al. (83), wherein mitochondrial fusion is required to equilibrate MitoTimer signal across the mitochondrial network. Collectively, these findings suggest that mitochondria may have an ability to sense protein homeostasis and use it to trigger fusion for proteostatic equilibration across the entire mitochondrial network.

We culminated our live cell imaging data into a computational model of mitochondrial dynamics (MiDyS). Due to the individual nature of mitochondria, we chose to use an agent-based modeling approach, in which individual mitochondrial agents can perform fusion and fission by defined rule sets. Multiple logistic regressions leveraging intrinsic variables of individual mitochondria from our neuronal recordings composed the basis of our stochastic model. In MiDyS, individually encoded parameters of size, shape, membrane potential, and MitoTimer ratio determine the actions and interactions of agents, which give rise to patterns of mitochondrial dynamics comparable to *in vitro* observations. Other groups have similarly leveraged agent-based modeling for the study of mitochondrial dynamics (350,351). While other models have focused on hypothesis testing of fundamental mitochondrial questions, the aim of MiDyS was to produce a framework for informing future investigations. We based the stochastic equations of our model on *in vitro* observations of variables of interest. The parameters of those *in vitro* experiments define the usefulness, but also limitation of our model. MiDyS currently represents a model of how mitochondrial size, shape, membrane potential, and protein homeostasis affect fusion and fission dynamics in cultured neurons. Results and conclusions made beyond this context should therefore be taken with caution. We believe that MiDyS is a framework that can be further developed and improved for many more applications and contexts. A multitude of known and unknown biological factors likely influence mitochondrial dynamics beyond the variables in this study, including Ca^{2+}, ATP, kinase activity, temperature, and pH. Integration of MiDyS with data describing these factors, as well as other models of mitochondrial biology has the potential to greatly enhance its utility and improve future investigations.

Conclusions from the data collected in this study and produced by MiDyS should not be extended outside of its original context. Live cell imaging was performed in mouse primary cortical neurons, a post-mitotic cell type with distinct cellular compartments (e.g. axon, dendrites). It is therefore unlikely that all observations of mitochondrial behavior directly translate to other cell types of interest. Analysis of mitochondria within neurons was equalized across all cellular compartments. A limitation of the fusion and fission event identification algorithm utilized in this study is that mitochondrial motility is not taken into account. It is therefore possible that highly mobile mitochondria could arise as false positives or negatives. We believe this issue is minimal due to the speed of mitochondrial transport observed in our recordings, but should still be considered as a limitation. MiDyS is a computational model meant to inform future experiments

and is limited by the variables encoded and assumptions made during development. Dynamics of mitochondrial biogenesis and mitophagy were not based on in vitro data collected in this study. Future work will be required to optimize stochastic equations for these behaviors. A critical limitation of agent-based modeling is the underestimation of global or environment-driven parameters on agent behavior. For example, mitochondrial fission is known to be influenced by mitochondria-ER contact sites (62). Unless encoded by another species of agents, the influence of ER tubules on mitochondrial dynamics is not represented.

We applied MiDyS to simulate proposed models of mitochondrial membrane potential and oxidative stress during I/R injury. The three models consider differing peaks of ROS production and amplitudes of membrane polarization. We then evaluate each mechanism by comparing MiDyS results to known patterns of neuronal I/R mitochondrial dynamics. The first model (Ischemia-ROS) considers the ischemic phase of the injury to be the major producer of ROS, with limited ROS production and effects on mitochondrial membrane potential during reperfusion (23,366,367,385). The second model (hyperpolarization-ROS) postulates that hyperpolarization of the mitochondrial membrane potential drives ROS production during the early stages of reperfusion, with the limited presence of ROS during ischemia (34,39,368). The third model (reperfusion-ROS) follows a similar ROS pattern to hyperpolarization-ROS with ROS peaking during reperfusion, but in this model ROS production is not dependent on hyperpolarization (27,28,90,386). Interestingly, only the hyperpolarization-ROS model generated a fission/fusion pattern similar to *in vitro* and *in vivo* models of neuronal/brain I/R injury (Chapter II; 85,86,151). These results highlight hyperpolarization and ROS during early reperfusion may be required for the slowing of mitochondrial fission and mild rebuilding of the mitochondrial network.

Collectively, our results identify unique characteristics of mitochondria prior to fission and fusion. We can leverage these distinct intrinsic properties to predict fission and fusion events. Using an agent-based modeling approach, we constructed a predictive computational model of mitochondrial dynamics. We believe this model can serve as a foundational tool for the study of mitochondrial dynamics and be utilized to inform and improve therapeutic trials targeting mitochondria.

5.4 Materials and Methods

Animals

All procedures were performed in accordance with institutional guidelines and approved by the University of Michigan Institutional Animal Care and Use Committee (IACUC). Mice were maintained on a 12 h light/dark cycle with standard rodent chow and water available ad libitum. Wild-type (WT) mice (C57BL/6J) were purchased from The Jackson Laboratory (Bar Harbor, ME). Thy1-Cre mice (358) were purchased from The Jackson Laboratory (Bar Harbor, ME). Conditional MitoTimer mice were generously provided by Zhen Yan, Virginia Polytechnic Institute and State University, VA (268).

Primary Neuron Culture

Cerebral cortices from postnatal day 0–1 (P0–P1) mouse pups were isolated and minced following sacrifice by decapitation. Tissue was incubated in enzyme digestion solution (Hibernate-A Medium (Gibco, A1247501), 1X B-27 supplement (Gibco, 17504044), 0.06 mg/mL L-cysteine (Sigma, 778672), $1.4 \times 10{-}2$ N NaOH (Sigma, 43617), 10 ng/mL APV (2-Amino-5-phosphonopentanoic acid, Sigma, A-5282), 1:100 Papain (Worthington, LS 03126), 40µg/mL DNase I from bovine pancreas (Roche, 11284932001) for 30 min at 37 °C. Following digestion, tissue was washed with DPBS and dissociated in Hibernate-A medium with 1X B-27. Cell density was measured by hemocytometer and trypan blue staining. Cells were seeded onto 0.1% PEI-coated glass coverslips in 24-well dishes (0.3 x 106 cells/well), 6-well dishes (1.5 x 106 cells/well) or 60mm dishes (4.5 x 106 cells/well). After 30 min, complete media change was performed with neurobasal complete medium (1x Neurobasal Plus medium (Gibco, A3582901), 1X B-27 Plus supplement (Gibco, A3653401), 0.5 mM Glutamax Supplement (Gibco, 35050061), and 1% Penicillin/Streptomycin Solution (Gibco, SV30010)). Cells were incubated at 37 °C with 5% CO2 for 14 days. Half-media changes were performed every 3–4 days with neurobasal complete medium.

Live-Cell Microscopy

On day-in-vitro 14, primary neurons are transferred to a live cell microscopy incubation chamber (37 °C with 20.9% O_2 5% CO_2) and allowed to acclimate for 30 minutes. For MitoTracker Deep Red recordings, cells were washed once with sterile PBS and incubated with 30nM

MitoTracker Deep Red FM (Fisher Scientific, M22426) in Earle's Balanced Salts Solution (EBSS) without phenol red (Fisher Scientific, AAJ67559AP) during 30 minute acclimation. Neurons were imaged on Zeiss Axio Observer Z1 inverted microscope with LED illumination. Z-stacks (0.24μm steps) of MitoTracker Deep Red or MitoTimer signal were acquired every 60 and 120 seconds, respectively. Z-stacks were processed using Zeiss Zen Pro extended depth of focus wavelets method. Images were exported in TIFF format for post-processing. LED power, exposure time, and histograms were fixed for all MitoTimer experiments.

Image Processing/Segmentation

Image processing and analysis was performed in FIJI (213). Mitochondrial signal was processed using the enhance local contrast (CLAHE) algorithm and background signal was subtracted with a rolling ball radius of 10 pixels. For MitoTimer analysis, green and red images were both processed and merged at this step. Mitochondrial objects were segmented using the Trainable Weka segmentation plug-in (240). Segmented images were then converted to 8-bit binary and segmentation over-estimation was removed using the morphological filters plug-in (239). Original images (non-processed) and segmented images were then used for downstream analysis.

Automated Detection of Fission/Fusion Events

A custom .ijm script was used for the automated detection of mitochondrial fission and fusion events (https://github.com/sanderson-lab/MiDyS-agent-model). Fission events were identified by transposing mitochondrial ROIs from frame^{n-1} onto frame^{n} and counting the number of mitochondrial objects within the original ROI. If more than one object was found in the ROI of the original mitochondrial object, that mitochondria was labeled as a fission object. Fusion events were identified by overlaying mitochondrial ROIs from frame^{n} onto frame^{n-1} and counting the number of mitochondrial objects in that ROI. If more than one object was found in the ROI of the resultant mitochondrial object, those objects were labeled as fusion objects. Fusion and fission labeled object ROIs were stored and fusion and fission events were quantified as the number of fission/fusion events divided by the total number of mitochondrial objects in a frame. For the quantification of intrinsic variables of mitochondrial objects, size/shape parameters were measured from segmented images and fluorescence intensity (MitoTracker Deep Red or MitoTimer green

and red) were measured from ROIs overlays onto original (un-processed) channel images. Measurements were taken from all mitochondrial objects, fission-labeled objects, and fusion-labeled objects. Stable objects were then identified by removing fission and fusion-labeled objects from the list of all mitochondrial objects. Mitochondrial measurements were saved as .csv files for further analysis in GraphPad Prism.

Equation Fitting/Regression

All data analysis, equation fitting, and quantification was performed in GraphPad Prism 9. Frequency distributions of stable, fusion, and fission mitochondrial objects were generated of intrinsic variables from MTDR and MitoTimer recordings. Many biological variables have floor effects that limit measures from falling below zero. These parameters were $\log_{10}$ transformed to allow for easier visualization and modeling of distribution. Gaussian curves were fit to frequency distributions for visual reference and analysis of normality. MitoTimer ratio data presented as non-normal and sums of two gaussian curves were generated for reference.

Classification and predictive modeling of mitochondrial objects was performed using variables that could easily be translated to and quantified in the agent-based modeling software NetLogo. For both MitoTimer and MitoTracker Deep Red data, multiple logistic regression was performed between fission and stable objects, and fusion and stable objects for the generation of four total regression models. Regression models were generated with intercept value, major axis, minor axis, log(area), log(aspect ratio), and log(MTDR or MitoTimer ratio). ROC curves and predicted probability violin plots were created to assess model performance.

MiDyS Modeling in NetLogo

Modeling of mitochondrial dynamics was performed using NetLogo, an open source software for the creation and utilization of agent-based models (359). A 50x50 patch simulation environment was set up in NetLogo with each patch representing a 1x1μm area. Our NetLogo model, called MiDyS, was coded for two procedure sequences: setup and main (go). MiDyS can be accessed by our GitHub repository: https://github.com/sanderson-lab/MiDyS-agent-model .

During setup, individual agents (default termed turtles in NetLogo) represent discrete mitochondrial units with an individual size of 0.5μm. Agents are randomly distributed at setup

with a sum determined by the user on the interface panel. At creation, agents are assigned intrinsic variables ("turtles-own") including age, membrane potential, and mitotimer ratio. Membrane potential and mitotimer ratios were assigned during setup using a normal random distribution, matching the gaussian distribution equations fit to log(MTDR) and log(MitoTimer ratio) distributions from live cell recordings. Initial Networking Density, a user-defined variable, then determines the extent of mitochondrial fusion during setup. Agents run a probability test based on the initial networking density to determine if they will fuse with neighboring agents. If an agent fuses with another agent, a link is created between those two agents. After initial networking, objects are then numbered to encode connected mitochondrial objects. A mitochondrial object is the sum of all agents connected in a network of links. These objects model the fused network morphology of mitochondria in a basal state.

At the conclusion of setup and during the go procedure, each individual agent performs calculations to determine derived intrinsic variables and fission/fusion probabilities. Each agent in the simulation calculates area, major axis, minor axis, aspect ratio (AR), and two fusion and fission probabilities. Equations for area in MiDyS is below in units of μm:

$$\text{area} = (0.5 * (\text{sum of agents in object})) + (0.3 * (\text{sum of link lengths in object})$$

Major and minor are defined as the farthest and shortest distances in μm between agents within a mitochondrial object. AR is the major/minor ratio. Because individual agents are connected into mitochondrial objects, all agents within an object share size and shape measurements. However, individual agents hold distinct membrane potential and MitoTimer values even when connected in an object. This behavior intends to model the local differences and compartmentalization often observed across large mitochondrial objects *in vitro* (362). The variables area, major, minor, aspect ratio, membrane potential (ΔΨ) and MitoTimer ratio are utilized to calculate the probability that a mitochondrial agent will perform fission and/or fusion. Probabilistic equations were determined by multiple logistic regression of these variables from *in vitro* mitochondrial recordings. The framework for probabilistic equations for fission/fusion (p_f) are listed below:

$$p_f = \frac{e^{(b_0+(b_1)(\log(area))+(b_2)(major)+(b_3)(minor)+(b_4)(AR)+(b_5)(\Delta\Psi))}}{1 + e^{(b_0+(b_1)(\log(area))+(b_2)(major)+(b_3)(minor)+(b_4)(AR)+(b_5)(\Delta\Psi))}}$$

$$p_f = \frac{e^{(b_0+(b_1)(\log(area))+(b_2)(major)+(b_3)(minor)+(b_4)(AR)+(b_5)(mitotimer))}}{1 + e^{(b_0+(b_1)(\log(area))+(b_2)(major)+(b_3)(minor)+(b_4)(AR)+(b_5)(mitotimer))}}$$

No *in vitro* data was obtained that included simultaneous recordings of mitochondrial membrane potential and MitoTimer ratio, therefore two separate equations were generated and encoded in the agent-based model. Agents choose the higher resulting probability between the two equations to define their true fusion or fission probability.

During the go procedure, each agent may move or migrate within the simulation environment. Headings are randomized and each agent has a 50% probability of moving 0.5μm. Movement is restricted if link length reaches the maximum allowed value. If an agent has one or more links to other agents, a fission probability check is performed. If a random value 0-100 falls below the calculated fission probability for a given agent, that agent breaks the link with its link neighbor that has the highest fission probability. If an agent has an unlinked neighbor within 2.5μm of itself, a fusion check is performed. If a random value 0-100 falls below the fusion probability for a given agent, that agent will create a new link to the local agent with the highest fusion probability. Mitochondrial objects are re-numbered and measured after both fission and fusion procedures. Agents may be removed from the simulation via the mitophagy function. Unlinked agents have an equal 10% chance of being removed by mitophagy after fission and fusion procedures. Surviving agents then have intrinsic age, membrane potential, and mitotimer adjusted. Age is increased by one after each tick of time. Mitochondrial membrane potential is encoded as the log transformation of relative MTDR intensity and fluctuates by random iterations between ± 0.07 arbitrary units. MitoTimer drifts negative as a function of the absolute value of membrane potential:

$$\text{Mitotimer} = (r_{-0.05-0}) * \text{abs}(\Delta\Psi)$$

In which, $r_{-0.05-0}$ is a random value between (-0.05) and 0. This equation intends to model the oxidation of MitoTimer over time and the dependence of that oxidation on physiological membrane potential. Membrane potential is encoded in MiDyS as a log transformation of the relative intensity of MTDR signal. Therefore, the further membrane potential deviates from zero, the further it leaves the basal range of membrane potential. The emergence of new agents is

dependent on the biogenesis function. Biogenesis occurs at a rate of 5% for all agents in the simulation. Agents undergoing biogenesis (parents) create and link with a newborn agent. The newborn agent is assigned an age of zero, membrane potential according to normal distribution described above, and the mitotimer value of the parent + 0.14. In order to perform biogenesis, a parent agent must have a membrane potential between (-0.2) and 0.2, and have open space on neighboring patches.

At the conclusion of migration, fission, fusion, mitophagy, aging, and biogenesis, the main procedure is complete. The user interface panel window and variable plots are updated, along with a global descriptor of network dynamics. This global variable, termed the fission/fusion index (FFI), ranges from -1 (fully fragmented) to 1 (highly fused) and is calculated as follows:

$$\text{FFI} = 2 * \frac{\#\text{ of agents with } > 1 \text{ link}}{\#\text{ of total agents}} - 1$$

Manipulations to membrane potential and mitotimer oxidation can be tuned on the MiDyS user interface. These variables alter membrane potential and mitotimer by a percentage of a set increment. Changes in these intrinsic parameters can be visualized via the window (with view-options) and on plots to the right.

Quantification and Statistical Analyses

Quantitative and statistical analyses were performed in Prism 9 (GraphPad Software, Boston, MA). Non-linear curves were fitted using the indicated equations. Final output data from antioxidant simulations was compared using One-Way ANOVA with multiple comparisons against the I/R condition, corrected using Dunnett's method. $p < .05$ was considered statistically significant and is indicated by *.

5.5 Figures

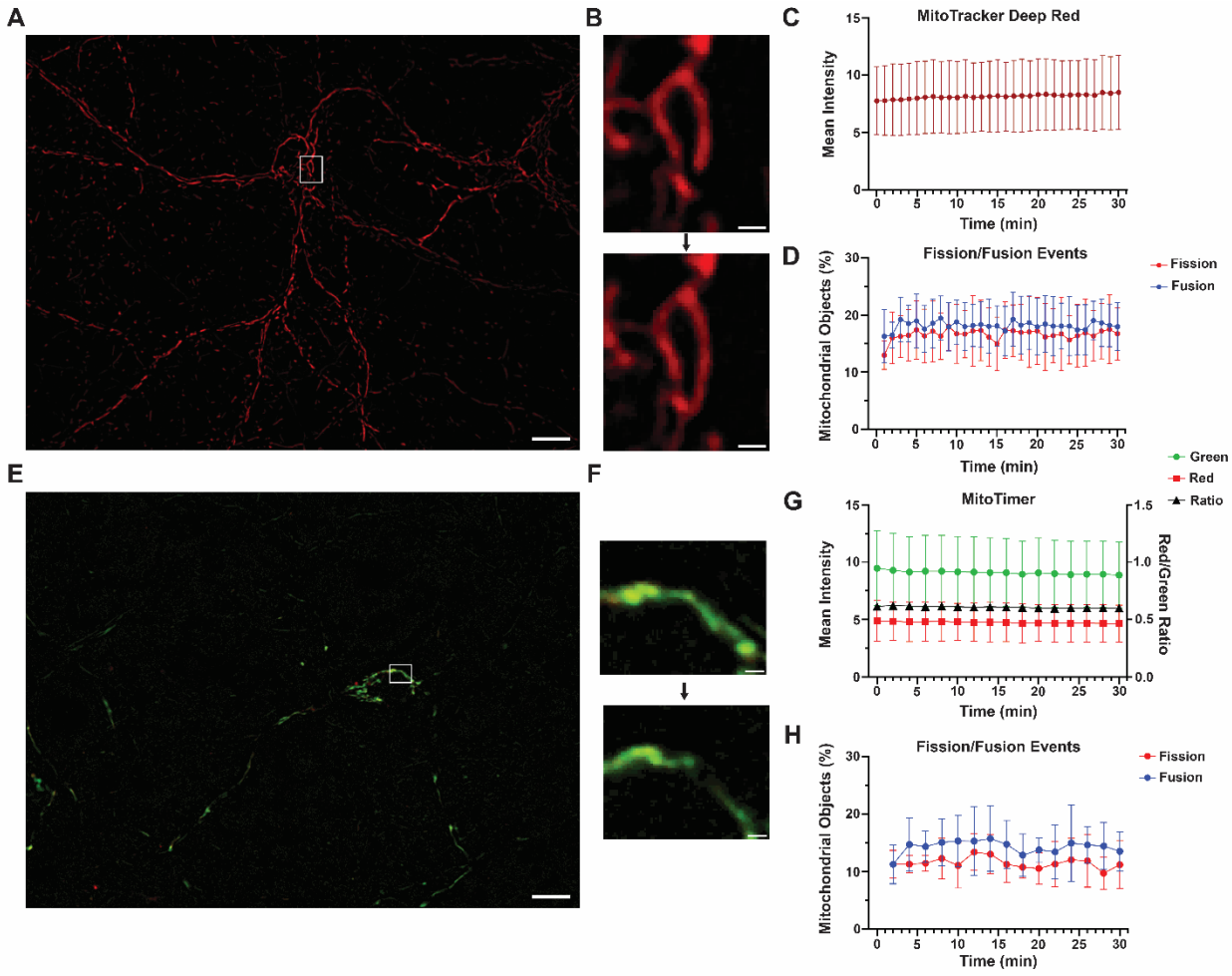

Figure 5-1. Neuronal recordings of mitochondrial dynamics

(A) Representative image of MitoTracker Deep Red-labeled neurons from live cell recordings. Scale bar = 10μm. **(**B) Representative frames 60 seconds apart of MitoTracker Deep Red-labeled mitochondria performing fusion. Scale bar = 1μm. (C) Quantification of MitoTracker Deep Red signal over time in neuron recordings. (D) Quantification of mitochondria undergoing fusion and fission events, as percentage of total mitochondrial objects, over time in MitoTracker Deep Red recordings. (E) Representative image of MitoTimer neuron from live cell recordings. Scale bar = 10μm. (F) Representative frames 120 seconds apart of MitoTimer expression mitochondria performing fission. Scale bar = 1μm. (G) Quantification of MitoTimer green signal, red signal (left y-axis), and red/green ratio (right y-axis) over time in MitoTimer neuron recordings. (H) Quantification of mitochondria undergoing fusion and fission events, as percentage of total mitochondrial objects, over time in MitoTimer recordings. n = 4-5 biological replicates

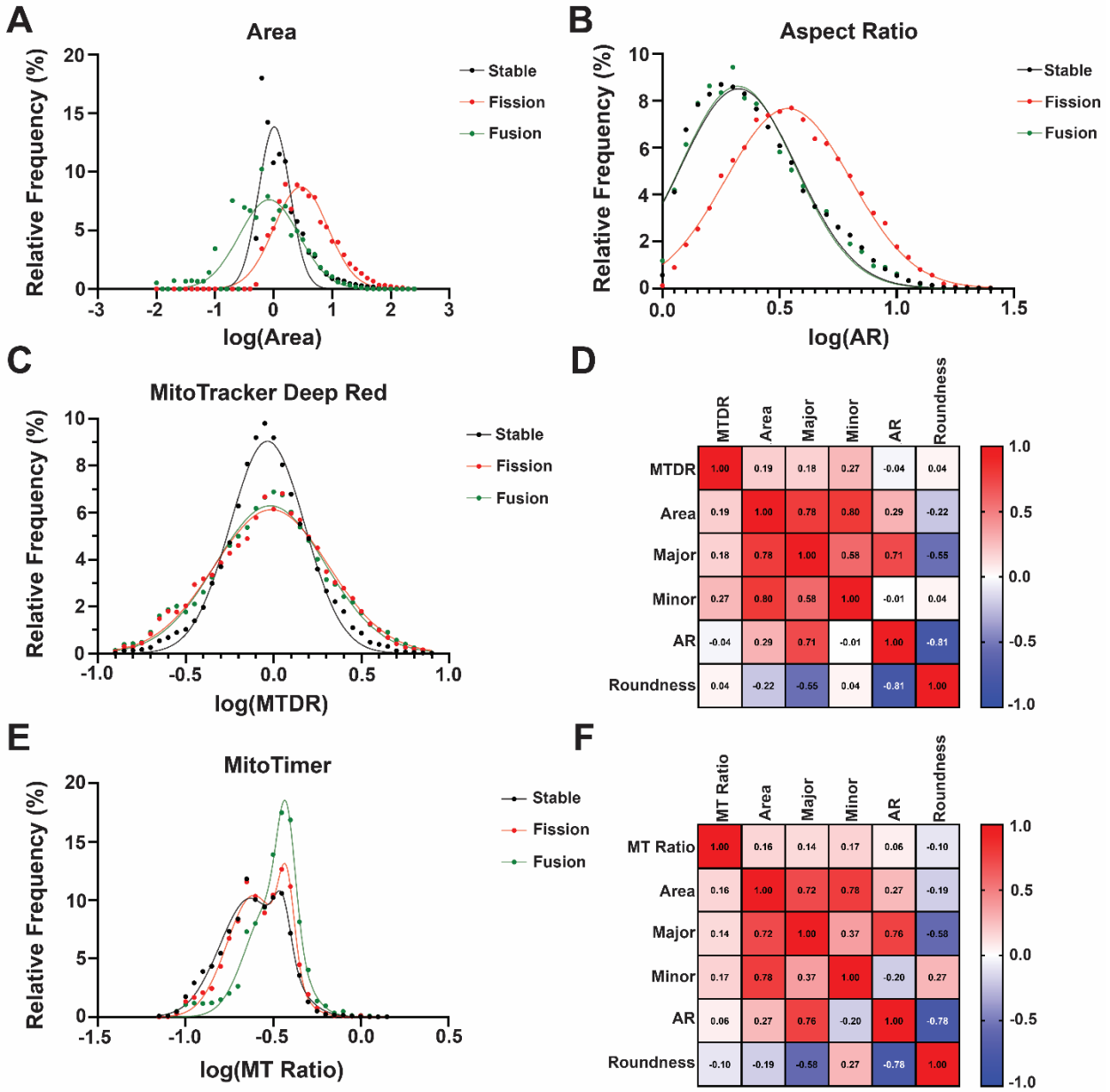

Figure 5-2. Dynamic mitochondria have unique intrinsic properties

(A) Histogram of log-transformed mitochondrial area (μm^2) from individual mitochondrial objects during MTDR recordings. Curves are fitted gaussian distributions. (B) Histogram of log-transformed aspect ratio (AR) from individual mitochondrial objects during MTDR recordings. Curves are fitted gaussian distributions. (C) Histogram of log-transformed relative MitoTracker Deep Red (MTDR) mean intensity from individual mitochondrial objects during MTDR recordings. Curves are fitted gaussian distributions. (D) Correlation matrix of intrinsic variables collected from individual mitochondrial objects during MTDR recordings. (E) Histogram of log-transformed MitoTimer red/green ratio from individual mitochondrial objects during MitoTimer recordings. Curves are sum of two gaussian distributions. (F) Correlation matrix of intrinsic variables collected from individual mitochondrial objects during MitoTimer recordings.

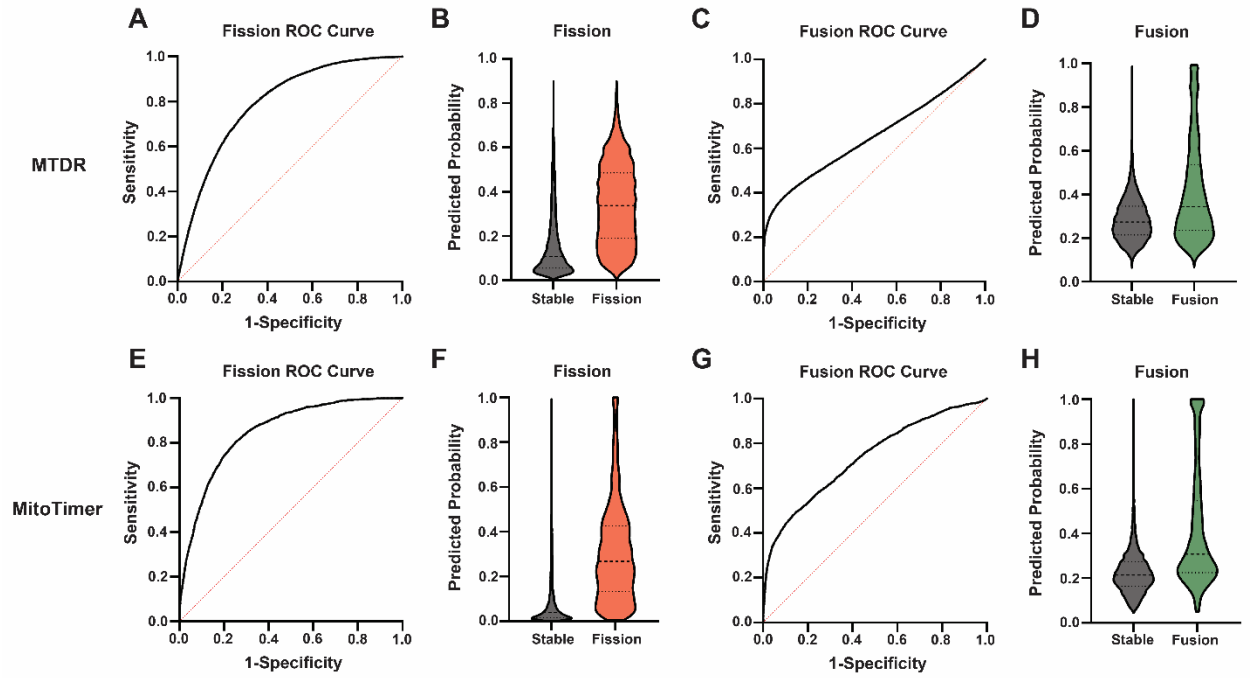

Figure 5-3. Intrinsic mitochondrial properties predict fission and fusion events

(A) ROC curve of multiple logistic regression classifying stable and fission mitochondria from MTDR recordings. (B) Violin plot of predicted probability for fission of MTDR-labeled mitochondria by multiple logistic regression. (C) ROC curve of multiple logistic regression classifying stable and fusion mitochondria from MTDR recordings. (D) Violin plot of predicted probability for fusion of MTDR-labeled mitochondria by multiple logistic regression. (E) ROC curve of multiple logistic regression classifying stable and fission mitochondria from MitoTimer recordings. (F) Violin plot of predicted probability for fission of MitoTimer mitochondria by multiple logistic regression. (G) ROC curve of multiple logistic regression classifying stable and fusion mitochondria from MitoTimer recordings. (H) Violin plot of predicted probability for fusion of MitoTimer mitochondria by multiple logistic regression.

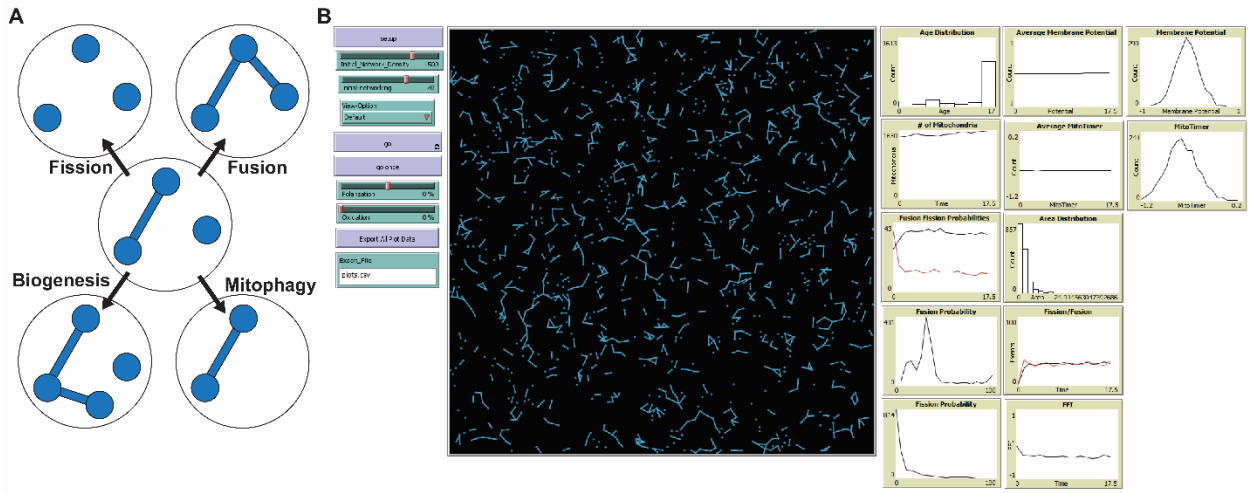

Figure 5-4. MiDyS: an agent-based model of mitochondrial dynamics

(A) Agents in MiDyS are circles that represent the smallest functional mitochondrial object. Fusion links can be made between agents to create larger mitochondrial objects. Agents can perform four actions with each tick (1min): fission (loss of link to other agent), fusion (creation of new link to other agent), biogenesis (growth of new connected agent), and mitophagy (loss of unlinked agent). (B) MiDyS model interface in NetLogo. Start/stop buttons, starting parameters, and export parameters are listed to the left of the central visualization panel. Mitochondrial dynamics can be visualized in the center window. To the right are live output plots of key network diagnostics and individual mitochondrial variables, including area, membrane potential, and fusion/fission probabilities.

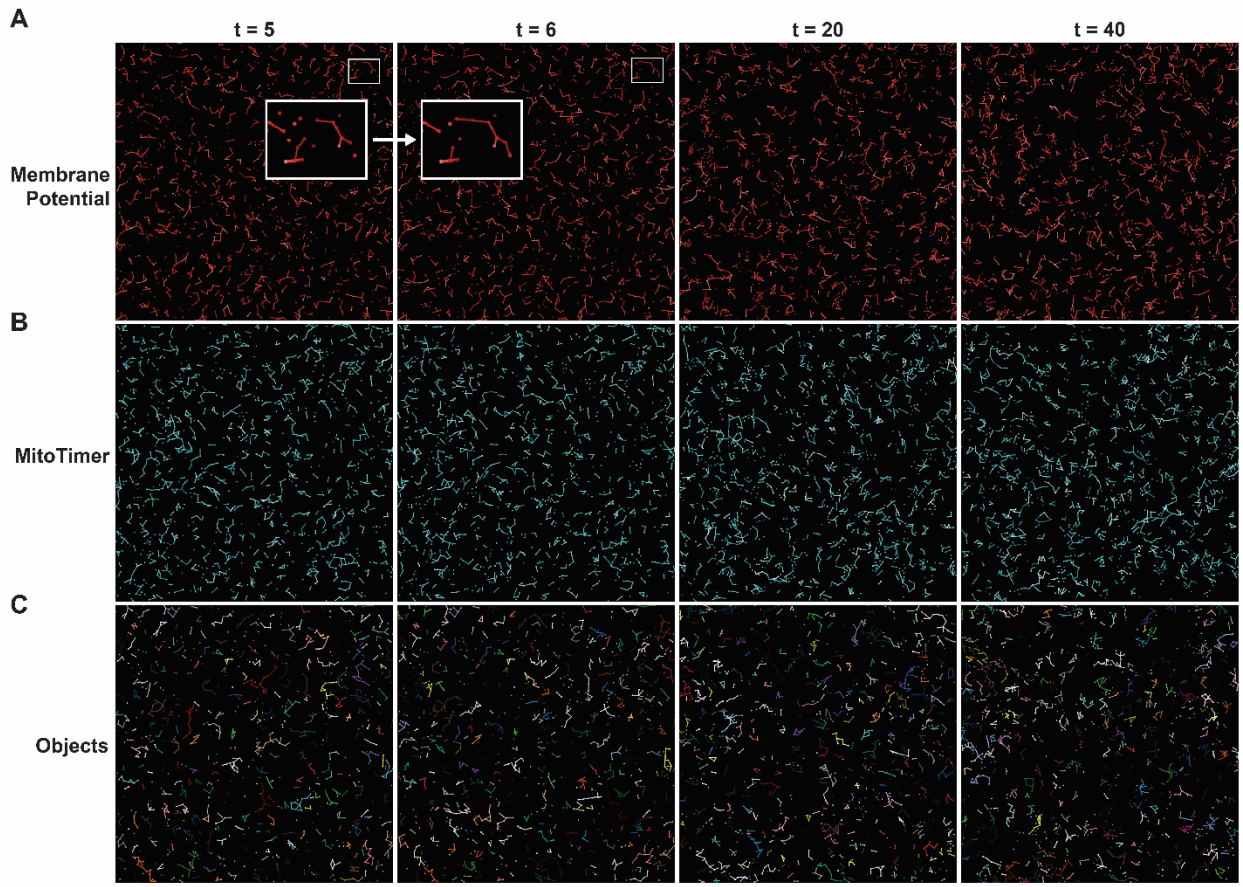

Figure 5-5. MiDyS allows for modeling and visualization of fission/fusion dynamics

(A) Representative images of MiDyS membrane potential visualization over simulated time. Insert: zoomed frames demonstrating fusion and fission. (B) Representative images of MiDyS MitoTimer visualization over simulated time. (C) Representative images of color-coded mitochondrial objects in MiDyS over time

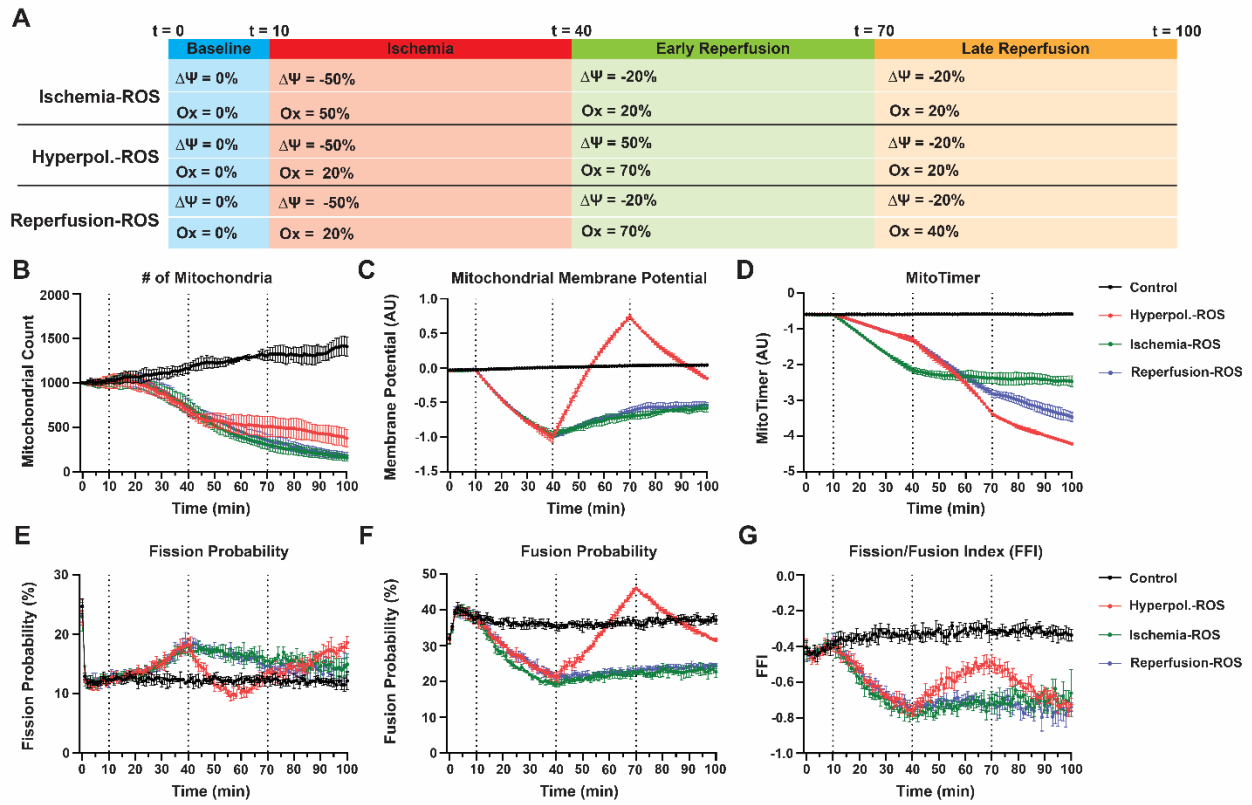

Figure 5-6. Simulated models of ischemia/reperfusion injury

(A) Timeline and table presenting the manipulations to mitochondrial membrane potential (ΔΨ) and oxidative stress (Ox) during the given phases of simulated I/R. (B) Quantification of mitochondrial count during I/R simulations. (C) Quantification of mean mitochondrial membrane potential during I/R simulations. (D) Quantification of mean MitoTimer during I/R simulations. (E) Quantification of mean fission probability during I/R simulations. (F) Quantification of mean fusion probability during I/R simulations. (G) Quantification of fission/fusion index (FFI) during I/R simulations. Dashed lines separate phases of I/R injury.

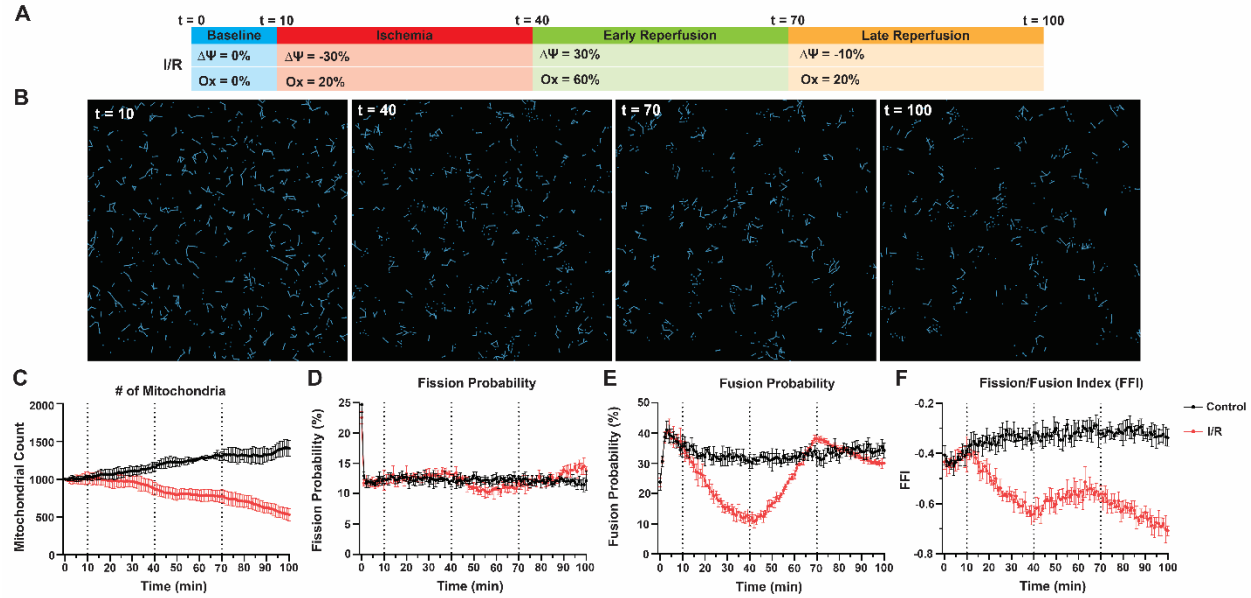

Figure 5-7. Simulated ischemia/reperfusion injury alters mitochondrial dynamics

(A) Timeline of simulated ischemia/reperfusion (I/R) injury paradigm in MiDyS with manipulation parameters. (B) Representative images of MiDyS at the conclusion of each phase of I/R simulation. (C) Quantification of mitochondrial count during I/R simulation. (D) Quantification of mean fission probability during I/R simulation. (E) Quantification of mean fusion probability during I/R simulation. (F) Quantification of fission/fusion index (FFI) during I/R simulation. Dashed lines separate phases of I/R injury.

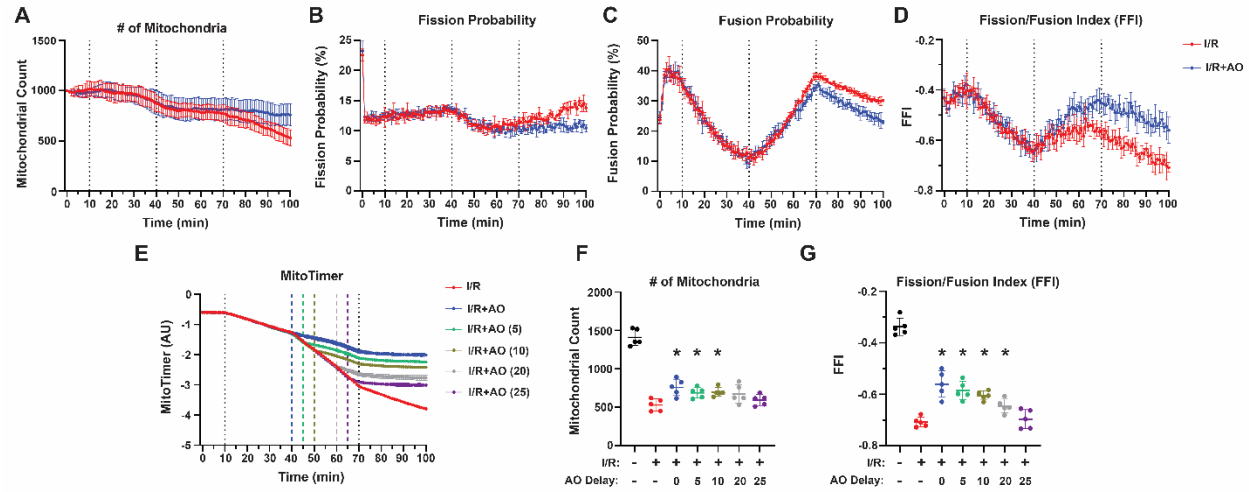

Figure 5-8. In silico experimentation predicts therapeutic window for antioxidant therapy

(A) Quantification of mitochondrial count during I/R simulation with antioxidant (AO) treatment at onset of reperfusion. (B) Quantification of mean fission probability during I/R+AO simulation. (C) Quantification of mean fusion probability during I/R+AO simulation. (D) Quantification of fission/fusion index (FFI) during I/R+AO simulation. (E) Quantification of mean MitoTimer during I/R with delayed AO treatment simulations. Minutes of delay is shown in parentheses for AO treatment. (F) Quantification of mitochondrial count at conclusion of I/R simulation with delayed AO treatment. * indicates $p < .05$ compared to I/R condition. (G) Quantification of fission/fusion index (FFI) at conclusion of I/R simulation with delayed AO treatment. * indicates $p < .05$ compared to I/R condition.

Chapter VI: Conclusions and Future Directions

6.1 Conclusions

This dissertation aimed to investigate the patterns and mechanisms of mitochondrial dynamics and proteostasis, and their interactions, during the therapeutic window of neuronal I/R injury. To this end, I developed a novel morphological analysis tool for the assessment of mitochondrial dynamics at the cell and tissue levels (Chapter II). This methodology was validated in neurons using genetic knockout of canonical dynamics proteins and pharmacological manipulation. I applied this novel methodology to study I/R injury in a primary neuron OGD/R paradigm. The morphology data demonstrates a multi-phasic pattern of mitochondrial dynamics during OGD/R, in which OGD induces mitochondrial fission until the onset of reoxygenation. Reconstructing fusion occurs during the early stages of reoxygenation until slowing at 2-4 hours reoxygenation. This pattern replicates previous findings of fusion loss and secondary fragmentation, but here with high temporal specificity at a single mitochondrion level. Additionally, we found that Drp1 is required for mitochondrial fission during OGD/R, and that the process of mitochondrial swelling is dependent on initial fragmentation by Drp1. Our results highlight the utility of machine learning-based mitochondrial classification and support a multi-phasic model of mitochondrial dynamics in neuronal I/R injury.

Mitochondrial quality control by means of mitophagy had been well studied in neurons, however, the turnover of intramitochondrial proteins, by either mitophagy or other mechanisms, has not been examined in I/R injury. We set out to study mitochondrial protein turnover via utilization of MitoTimer, a genetic reporter used to visualize protein aging and oxidation (Chapter III). We demonstrate a novel timeline of mitochondrial protein turnover that contains a peak in protein turnover at 2 hours of reoxygenation following OGD. We found no increases in mitochondrial protease levels during OGD/R to explain this finding. However, we found that activity of the mitochondrial matrix protease LonP1 was increased at the time of increased protein turnover. Further, inhibition of LonP1 ameliorated this proteostatic peak. It is likely that

intramitochondrial proteases like LonP1 work along side mitophagy to turnover mitochondrial proteins, as we also found inhibition of turnover in Parkin knockout neurons. Interestingly, genetic loss of key dynamics proteins Drp1 and Opa1 differentially alter mitochondrial protein turnover. These findings demonstrate a unique interaction between the systems of mitochondrial dynamics and quality control.

We observed both fusion inhibition and mitochondrial protein turnover activity between 2 and 4 hours of reperfusion. Additional work in our lab has demonstrated mitophagy initiation during this window as well (273). This timeframe appears to be a transitionary phase for the mitochondrial response to I/R injury. We were therefore interested in investigating how aspects of mitochondrial (dys)function may initiate the observed changes in dynamics and proteostasis. An interesting pathway connecting dynamics and proteostasis is the Opa1 cleavage pathway. Opa1, the crucial inner membrane fusion protein, requires regulated proteolytic processing by the protease Oma1 in order to function efficiently. We hypothesized that increased Oma1 activity during early reperfusion (corresponding to the protein turnover peak) would cleave too much Opa1, rendering fusion inoperable. Contrary to our hypothesis, we found the Opa1 cleavage pattern to respond to OGD and persist through reoxygenation without exacerbation (Chapter IV). To better understand this system, we methodically studied the activation criteria for Oma1-dependent Opa1 cleavage. We found that depolarization and hyperpolarization of the mitochondrial membrane potential to be sufficient for Oma1 activation. Both polarization phenomena can induce ROS production, therefore we asked whether or not ROS could be the unifying activation criteria. Intriguingly, only depolarization relied on ROS to activate Oma1. These results add complexity to the previously suggested models of Oma1 activation. We then investigated the contributions of Oma1 to the response of mitochondria to stress. We found that Oma1 knockout cells had higher fission levels than WT cells after drug-induced depolarization and hyperpolarization. However, Oma1 knockout cells were better equipped for fusion recovery after fragmentation, despite higher levels of initial fission. Our data presents Oma1 as a two-way player in the mitochondrial stress response. During the initial period of stress, Oma1 is needed to limit excessive fission. However, limiting Oma1 activity during recovery after stress increases the reconstruction of the mitochondrial network. Collectively, our Opa1/Oma1 studies present Oma1 as a potential limiting factor for fusion recovery after stress, and potentially in a multimodal injury of polarization and ROS like I/R.

Together, our data pointed to an intersection of intrinsic mitochondrial properties (e.g. mitochondrial membrane potential, proteostasis) and mitochondrial dynamics. We therefore synthesized our data, along with live cell imaging data, to generate an agent-based model of mitochondrial dynamics (Chapter V). Our **Mi**tochondrial **Dy**namics **S**imulation (**MiDyS**) integrates intrinsic variables of individual mitochondrial agents to define their stochastic fission and fusion behaviors. MiDyS accurately simulates physiological dynamics behavior of cultured neurons. To demonstrate the utility of MiDyS, we simulated I/R injury with and without therapeutic intervention. Our results present the utility of MiDyS to inform and improve experimental trials of therapeutic interventions of acute injury/pathophysiology.

6.2 Future Directions

Future experiments should focus on further examining the incomplete rescue of mitochondrial fusion during reoxygenation. The loss of fusion and secondary wave of fission observed in our studies and others represents a key therapeutic target and window. Interventions provided during early reoxygenation that promote mitochondrial fusion before it halts could be critical for preserving mitochondrial function and ultimate neuronal survival. We propose Oma1 as a lynchpin in the fusion response after stress. Future experiments should evaluate if transient Oma1 inhibition during reoxygenation is neuroprotective. The study of Oma1 is currently limited by the lack of effective pharmacological inhibitors.

Additional study is required to understand the role that LonP1 plays in the response to injury. It is currently unclear if LonP1-dependent mitochondrial protein turnover is pro- and anti-survival. Outcomes studies with LonP1 inhibition and knockout will be required to probe this question, although LonP1's role in clearing misfolded and oxidized proteins suggests it as a potential therapeutic target.

The construction of MiDyS is a promising application of predictive modeling for the study of mitochondrial biology. MiDyS, like all computational models, is limited by its encoded information and the data in which it is based. Inclusion of other critical variables for mitochondrial function (e.g. Ca^{2+}, ATP, pH) would greatly enhance the utility of MiDyS. Here we present MiDyS as a blueprint for how agent-based modeling can be used to perform *in silico* experiments for the improvement of future 'wet lab' research.

6.3 Final Remarks

Collectively, this thesis defines several patterns and interactions of mitochondrial homeostatic mechanisms. Changes in mitochondrial dynamics and quality control pathways are hallmarks of the mitochondrial response to stresses, including I/R injury. Here, we delineate the patterns of those responses and describe several mechanisms by which they interact with each other and critical aspects of mitochondrial function at the single mitochondria level. The tools and data produced here will greatly enhance our understanding and study of mitochondrial dysfunction in neuronal I/R injury.

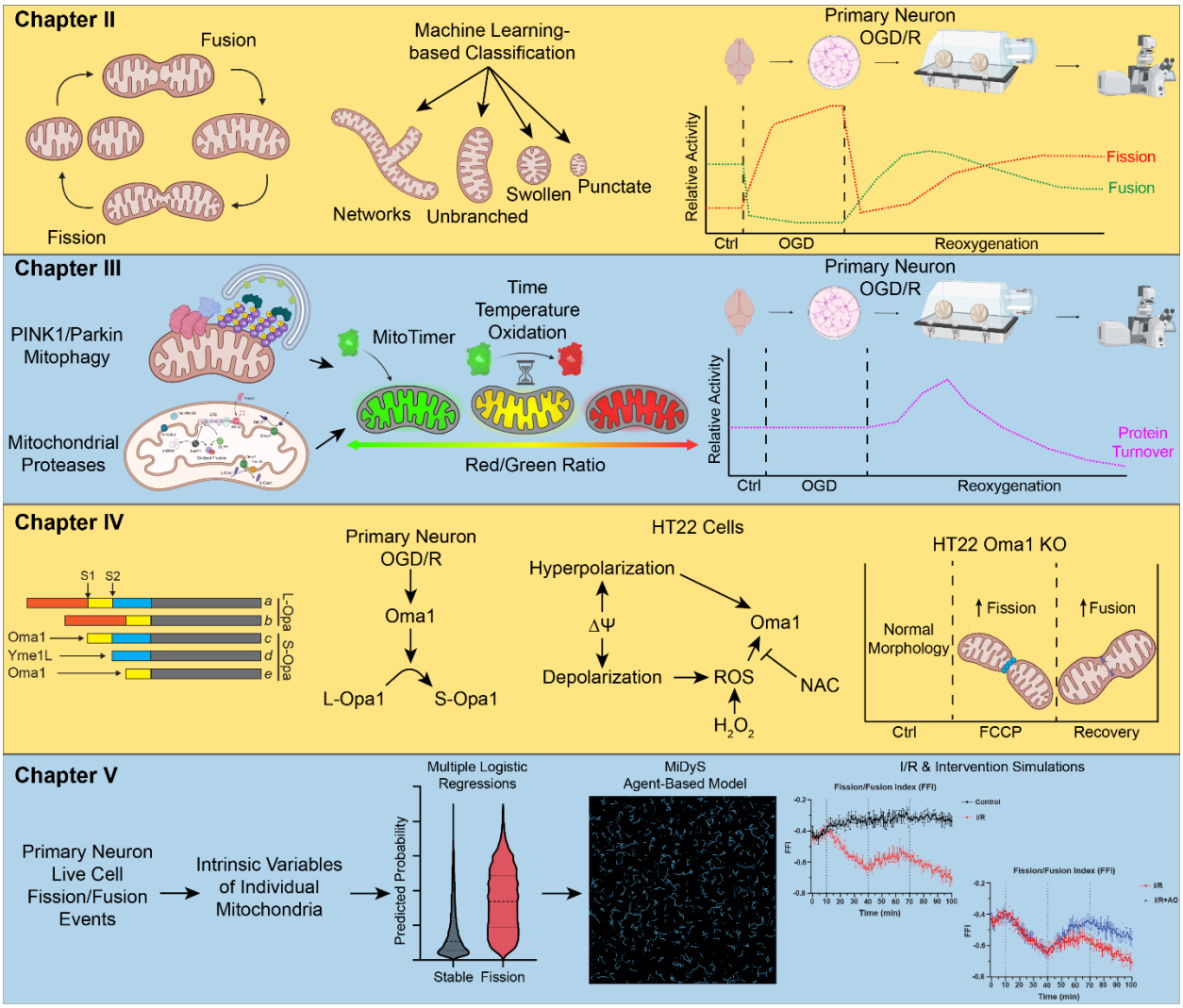

Figure 6-1. Graphical abstract and summary of dissertation.

Bibliography

1. Pu, L., Wang, L., Zhang, R., Zhao, T., Jiang, Y., and Hang, L. (2023). Projected global trends in ischemic stroke incidence, Deaths and disability-adjusted life years from 2020 to 2030. *Stroke.* 5495), 1330-1339.
2. Saini, V., Guada, L., and Yavagal, D.R. (2021). Global epidemiology of stroke and access to acute ischemic stroke interventions. *Neurology.* 97920), S6-S16.
3. Rajajee, V., Muehlschlegel, S., Wartenberg, K.E., Alexander, S.A., Busl, K.M., Chou, S.H.Y., Creutzfeldt, C.J., *et al.* (2023). Guidelines for neuroprognostication in comatose adult survivors of cardiac arrest. *Neurocrit Care.* 38(3), 533-563.
4. Fan, A.P., An, H., Moradi, F., Rosenberg, J., Ishii, Y., Nariai, T., Okazawa, H., *et al.* (2020). Quantification of brain oxygen extraction and metabolism with [15O]-gas PET: A technical review in the era of PET/MRI. *Neuroimage.* 220, 117136.
5. Mergenthaler, P., Lindauer, U., Dienel, G.A., Meisel, A. (2013). Sugar for the brain: the role of glucose in physiological and pathological brain function. *Trends Neurosci.* 36(10), 587-597.
6. Li, H., Guglielmetti, C., Sei, Y.J., Zilberter, M., Le Page, L.M., Shields, L., Yang, J., *et al.* (2023). Neurons require glucose uptake and glycolysis in vivo. *Cell Rep.* 42(4), 112335.
7. Catchlove, S.J., Macpherson, H., Hughes, M.E., Chen, Y., Parrish, T.B., Pipingas, A. (2018). An investigation of cerebral oxygen utilization, blood flow and cognition in healthy aging. *PLoS One.* 13(5), e0197055.
8. Nedergaard, M. (1988). Mechanisms of brain damage in focal cerebral ischemia. *Acta Neurol Scand.* 77(2), 81-101.
9. Constantakis, J.W., Reed-McBain, C.A., and Famakin, B. (2023). Astrocyte innate immune activation and injury amplification following experimental focal cerebral ischemia. *Neurochem Int.* 162, 105456.
10. del Zoppo, G.J., and Mabuchi, T. (2003). Cerebral microvessel responses to focal ischemia. *J Cereb Blood Flow Metab.* 23(8), 879-894.
11. Wang, Y., Zhang, J.H., Sheng, J., and Shao, A. (2019). Immunoreactive cells after cerebral ischemia. *Front Immunol.* 10, 2781.
12. Scumpia, A.J., Kafel, J., Hallas, B.H., Horowitz, J.M., and Torres, G. (2007). Endothelial heat shock response in cerebral ischemia. *Histol Histopathol.* 22(7), 815-823.
13. Powers, W.J., Rabinstein, A.A., Ackerson, T., Adeoye, O.M., Bambakidis, N.C., Becker, K., Biller, J., *et al.* (2019). Guidelines for the early management of patients with acute ischemic stroke: 2019 update to the 2018 guidelines for the early management of acute ischemic stroke: A guideline for healthcare professionals from the American Heart Association/American Stroke Association. *Stroke.* 50(12), e344-e418.

14. Lindbolm, R.P.F., Tovedal, T., Norlin, B., Hillered, L., Englund, E., and Thelin, S. (2021). Mechanical reperfusion following prolonged global cerebral ischemia attenuates brain injury. *J Cardiovasc Transl Res.* 14(2), 338-347.
15. Mazighi, M., Chaudry, S.A., Ribo, M., Khatri, P., Skoloudik, D., Mokin, M., Labreuche, J., *et al.* (2013). Impact of onset-to-reperfusion time on stroke mortality: a collaborative pooled analysis. *Circulation.* 127(19), 1980-1985.
16. Sekhon, M.S., Ainslie, P.N., and Griesdale, D.E. (2017). Clinical pathophysiology of hypoxic ischemic brain injury after cardiac arrest: a "two-hit" model. *Crit Care.* 21(1), 90.
17. Nunnari, J., and Suomalainen, A. (2012). Mitochondria: in sickness and in health. *Cell.* 148(6), 1145-1159.
18. van der Bliek, A.M., Sedensky, M.M., and Morgan, P.G. (2017). Cell biology of the mitochondrion. *Genetics.* 207(3), 843-871.
19. Folch-Llorente, I., Rueda, C.B., Pardo, B., Szabadkai, G., Duchen, M.R., and Satrustegui, J. (2015). The regulation of neuronal mitochondrial metabolism by calcium. *J Physiol.* 593(16), 3447-3462.
20. Rangaraju, V., Calloway, N., and Ryan, T.A. (2014). Activity-driven local ATP synthesis is required for synaptic function. *Cell.* 156(4), 825-835.
21. Magistretti, P.J., and Allaman, I. (2015). A cellular perspective on brain energy metabolism and functional imaging. *Neuron.* 86(4), 883-901.
22. Taanman, J.W. (1997). Human cytochrome c oxidase: structure, function, and deficiency. *J Bioenerg Biomembr.* 29(2), 151-163.
23. Kuzmiak-Glancy, S., Glancy, B., and Kay, M.W. (2022). Ischemic damage to every segment of the oxidative phosphorylation cascade elevates ETC driving force and ROS production in cardiac mitochondria. *Am j Physiol Heart Circ Physiol.* 323(3), H499-H512.
24. Vercellino, I., and Sazanov, L.A. (2022). The assembly, regulation and function of the mitochondrial respiratory chain. *Nat Rev Mol Cell Biol.* 23(2), 141-161.
25. Zorova, L.D., Popkov, V.A., Plotnikov, E.Y., Silachev, D.N. Pevzner, I.B., Jankauskas, S.S., Babenko, V.A., *et al.* (2018). Mitochondrial membrane potential. *Anal Biochem.* 552, 50-59.
26. Sack, M.N. (2006). Mitochondrial depolarization and the role of uncoupling proteins in ischemia tolerance. *Cardiovasc Res.* 72(2), 210219.
27. Levraut, J., Iwase, H., Shao, Z., Vanden Hoek, T.L., and Schumacker, P.T. (2003). Cell death during ischemia: relationship to mitochondrial depolarization and ROS generation. *Am J Physiol Heart Circ Physiol.* 284(2), H549-H558.
28. Abramov, A.Y., Scoziello, A., and Duchen, M.R. (2007). Three distinct mechanisms generate oxygen free radicals in neurons and contribute to cell death during anoxia and reoxygenation. *J Neurosci.* 27(5), 1129-1138.
29. Liu, R.R., and Murphy, T.H. (2009). Reversible cyclosporin A-sensitive mitochondrial depolarization occurs within minutes of stroke onset in mouse somatosensory cortex in vivo. *J Biol Chem.* 284(52), 36109-36117.
30. Puka-Sundvall, M., Gajkowska, B., Cholewinski, M., Blomgren, K., Lazarewicz, J.W., and Hagberg, H. (2000). Subcellular distribution of calcium and ultrastructural changes after cerebral hypoxia-ischemia in immature rats. *Brain Res Dev Brain Res.* 125(1-2), 31-41.

31. Frantseva, M.V., Carlen, P.L., and Velazquez, J.L.P. (2001). Dynamics of intracellular calcium and free radical production during ischemia in pyramidal neurons. *Free Radic Biol Med.* 31(10), 1216-1227.
32. McCormack, J.G., and Denton, R.M. (1993). The role of intramitochondrial Ca2+ in the regulation of oxidative phosphorylation in mammalian tissues. *Biochem Soc Trans.* 21(3), 793-799.
33. Huttemann, M., Lee, I., Pecinova, A., Pecina, P., Przyklenk, K., and Doan, J.W. (2008). Regulation of oxidative phosphorylation, the mitochondrial membrane potential, and their role in human disease. *J Bioenerg Biomembr.* 40(5), 445-456.
34. Sanderson, T.H., Reynolds, C.A., Kumar, R., Przyklenk, K., and Huttemann, M. (2013). Molecular mechanisms of ischemia-reperfusion injury in brain: Pivotal role of the mitochondrial membrane potential in reactive oxygen species generation. *Mol Neurobiol.* 47(1), 9-23.
35. Ludwig, B., Bender, E., Arnold, S., Huttemann, M., Lee, I., and Kadenbach, B. (2001). Cytochrome C oxidase and the regulation of oxidative phosphorylation. *Chembiochem.* 2(6), 392-403.
36. Helling, S., Huttemann, M., Ramzan, R., Kim, S.H., Lee, I., Muller, T., Langenfield, E., *et al.* (2012). Multiple phosphorylations of cytochrome c oxidase and their functions. *Proteomics.* 12(7), 950-959.
37. Korenic, A., Boltze, J., Deten, A., Peters, M., Andjus, P., and Radenovic, L. (2014). Astrocytic mitochondrial membrane hyperpolarization following extended oxygen and glucose deprivation. *PLoS One.* 9(2), e90697.
38. Liu, S.S. (1999). Cooperation of a "reactive oxygen cycle" with the Q cycle and the proton cycle in the respiratory chain--superoxide generating and cycling mechanisms in mitochondria. *J Bioenerg Biomembr.* 31(4), 367-376.
39. Iijima, T., Mishima, T., Akagawa, K., and Iwao, Y. (2006). Neuroprotective effect of propofol on necrosis and apoptosis following oxygen-glucose deprivation--relationship between mitochondrial membrane potential and mode of death. *Brain Res.* 1099(1), 25-32.
40. Zhdanov, A.V., Aviello, G., Knaus, U.G., and Papkovsky, D.B. (2017). Cellular ROS imaging with hydro-Cy3 dye is strongly influenced by mitochondrial membrane potential. *Biochim Biophys Acta Gen Subj.* 1861(2), 198-204.
41. Niizuma, K., Endo, H., and Chan, P.H. (2009). Oxidative stress and mitochondrial dysfunction as determinants of ischemic neuronal death and survival. *J Neurochem.* 109(S1), 133-138.
42. Anzell, A.R., Maizy, R., Przyklenk, and Sanderson, T.H. (2018). Mitochondrial quality control and disease: Insights into ischemia-reperfusion injury. *Mol Neurobiol.* 55(3), 2547-2564.
43. Chan, D.C. (2020). Mitochondrial dynamics and its involvement in disease. *Annu Rev Pathol.* 15, 235-259.
44. Kleele, T., Rey, T., Winter, J., Zaganelli, S., Mahecic, D., Lambert, H.P., Ruberto, F.P., *et al.* (2021). Distinct fission signatures predict mitochondrial degradation or biogenesis. *Nature.* 593(7859), 435-439.
45. Lewis, S.C., Uchiyama, L.F., and Nunnari, J. (2016). ER-mitochondria contacts couple mtDNA synthesis with mitochondrial division in human cells. *Science.* 353(6296), aaf5549.

46. van der Bliek, A.M., Shen, Q., and Kawajiri, S. (2013). Mechanisms of mitochondrial fission and fusion. *Cold Spring Harb Perspect Biol.* 5(6), a011072.
47. Giacomello, M., Pyakurel, A., Glytsou, C., and Scorrano, L. (2020). The cell biology of mitochondrial membrane dynamics. *Nat Rev Mol Cell Biol.* 21(4), 204-224.
48. Adebayo, M., Singh, S., Singh, A.P., and Dasgupta, S. (2021). Mitochondrial fusion and fission: The fine-tune balance for cellular homeostasis. *FASEB J.* 35(6), e21620.
49. Shi, W., Tan, C., Liu, C., and Chen, D. (2022). Mitochondrial fission mediated by Drp1-Fis1 pathway and neurodegenerative diseases. *Rev Neurosci.* 34(3), 275-294.
50. Pegadraju, H., Thomas, J.A., and Kumar, R. (2023). Mechanistic and therapeutic role of Drp1 in the pathogenesis of stroke. *Gene.* 855, 147130.
51. Cereghetti, G.M., Stangherlin, A., de Brito, O.M., Chang, C.R., Blackstone, C., Bernardi, P., and Scorrano, L. (2008). Dephosphorylation by calcineurin regulates translocation of Drp1 to mitochondria. *Proc Natl Acad Sci U S A.* 105(41), 15803-15808.
52. Cribbs, J.T., and Strack, S. (2007). Reversible phosphorylation of Drp1 by cyclic AMP-dependent protein kinase and calcineurin regulates mitochondrial fission and cell death. *EMBO Rep.* 8(10), 939-944.
53. Valera-Ablerni, M., Joffraud, M., Miro-Blanch, J., Capellades, J., Junza, A., Dayon, L., Galindo, A.N., *et al.* (2021). Crosstalk between Drp1 phosphorylation sites during mitochondrial remodeling and their impact on metabolic adaptation. *Cell Rep.* 36(8), 109565.
54. Loson, O.C., Song, Z., Chen, H., and Chan, D.C. (2013). Fis1, Mff, MiD49, and MiD51 mediate Drp1 recruitment in mitochondrial fission. *Mol Biol Cell.* 24(5), 659-667.
55. Yang, J., Chen, P., Cao, Y., Liu, S., Wang, W., Li, L., Li, J., *et al.* (2023). Chemical inhibition of mitochondrial fission via targeting the DRP1-receptor interaction. *Cell Chem Biol.* 30(3), 278-294.
56. Liu, A., Kage, F., and Higgs, H.N. (2021). Mff oligomerization is required for Drp1 activation and synergy with actin filaments during mitochondrial division. *Mol Biol Cell.* 32(20), ar5.
57. Kornfeld, O.S., Qvit, N., Haileselassie, B., Shamloo, M., Bernardi, P., and Mochly-Rosen, D. (2018). Interaction of mitochondrial fission factor with dynamin related protein 1 governs physiological mitochondrial function in vivo. *Sci Rep.* 8, 14034.
58. Rios, L., Pokhrel, S., Li, S., Heo, G., Haileselassie, B., and Mochly-Rosen, D. (2023). Targeting an allosteric site in dynamin-related protein 1 to inhibit Fis1-mediated mitochondrial dysfunction. *Nat Commun.* 14(1), 4356.
59. Adachi, Y., Itoh, K., Yamada, T., Cerveny, K.L., Suzuki, T.L., Macdonald, P., Frohman, M.A., *et al.* (2016). Coincident phosphatidic acid interaction restrains Drp1 in mitochondrial division. *Mol Cell.* 63(6), 1034-1043.
60. Ingerman, E., Perkins, E.M., Marino, M., Mears, J.A., McCaffery, J.M., Hinshaw, J.E., and Nunnari, J. (2005). Dnm1 forms spirals that are structurally tailored to fit mitochondria. *J Cell Biol.* 170(7), 1021-1027.
61. Kalia, R., Wang, R.Y., Yusuf, A., Thomas, P.V., Agard, D.A., Shaw, J.M., and Frost, A. (2018). Structural basis of mitochondrial receptor binding and constriction by DRP1. *Nature.* 558(7710), 401-405.
62. Friedman, J.R., Lackner, L.L., West, M., DiBenedetto, J.R., Nunnari, J., and Voletz, G.K. (20110. ER tubules mark sites of mitochondrial division. *Science.* 334(6054), 358-362.

63. Adachi, Y., Kato, T., Yamada, T., Murata, D., Arai, K., Stahelin, R.V., Chan, D.C., *et al.* (2020). Drp1 tubulates the ER in a GTPase-independent manner. *Mol Cell.* 80(4), 621-632.
64. Ji, W., Hatch, A.L., Merrill, R.A., Strack, S., and Higgs, H.N. (2015). Actin filaments target the oligomeric maturation of the dynamin GTPase Drp1 to mitochondrial fission sites. *Elife.* 4, e11553.
65. Kraus, F., Roy, K., Pucadyil, T.J., and Ryan, M.T. (2021). Function and regulation of the divisome for mitochondrial fission. *Nature.* 590(7844), 57-66.
66. Tan, A.R., Cai, A.Y., Deheshi, S., and Rintoul, G.L. (2011). Elevated intracellular calcium causes distinct mitochondrial remodelling and calcineurin-dependent fission in astrocytes. *Cell Calcium.* 49(2), 108-114.
67. Basit, F., van Oppen, L.M., Schockel, L., Bossenbroek, H.M., van Emst-de-Vries, S.E., Hermeling, J.C., Grefte, S., *et al.* (2017). Mitochondrial complex I inhibition triggers a mitophagy-dependent ROS increase leading to necroptosis and ferroptosis in melanoma cells. *Cell Death Dis.* 8(3), e2716.
68. Cid-Castro, C., Hernandez-Espinosa, D.R., and Moran, J. (2018). ROS as regulators of mitochondrial dynamics in neurons. *Cell Mol Neurobiol.* 38(5), 995-1007.
69. Jones, E., Gaytan, N., Garcia, I., Herrera, A., Ramos, M., Agarwala, D., Rana, M., *et al.* (2017). A threshold of transmembrane potential is required for mitochondrial dynamic balance mediated by DRP1 and OMA1. *Cell Mol Life Sci.* 74(7), 1347-1363.
70. Jezek, J., Cooper, K.F., and Strich, R. (2021). The impact of mitochondrial fission-stimulated ROS production on pro-apoptotic chemotherapy. *Biology (Basel).* 10(1), 33.
71. Wu, D., Hou, Y., Zhao, Z., Liang, N., Yuan, P., Yang, T., Xing, J., *et al.* (2022). Increased mitochondrial fission drives the reprogramming of fatty acid metabolism in hepatocellular carcinoma cells through suppression of Sirtuin 1. *Cancer Commun (Lond).* 42(1), 37-55.
72. Dong, W., Long, L., Deng, Q., Liu, D., Wang, J., Wang, F., and Chen, J. (2023). Mitochondrial fission drives neuronal metabolic burden to promote stress susceptibility in male mice. *Nat Metab.* 5(12), 2220-2236.
73. Roe, A.J., and Qi, X. (2018). Drp1 phosphorylation by MAPK1 causes mitochondrial dysfunction in cell culture model of Huntington's disease. *Biochem Biophys Res Commun.* 496(2), 706-711.
74. Quintana-Cabrera, R., Scorrano, L. (2023). Determinants and outcomes of mitochondrial dynamics. *Mol Cell.* 83(6), 857-876.
75. Gao, S., and Hu, J. (2021). Mitochondrial fusion: The machineries in and out. *Trends Cell Biol.* 31(1), 62-74.
76. Chandhok, G., Lazarou, M., and Neumann, B. (2018). Structure, function, and regulation of mitofusin-2 in health and disease. *Biol Rev Philos Soc.* 93(2), 933-949.
77. Ban, T., ishihara, T., Kohno, H., Saita, S., Ichimura, A., Maenaka, K., Oka, T., *et al.* (2017). Molecular basis of selective mitochondrial fusion by heterotypic action between OPA1 and cardiolipin. *Nat Cell Biol.* 19(7), 856-863.
78. Del Dotto, V., Fogazza, M., Carelli, V., Rugolo, M., and Zanna, C. (2018). Eight human OPA1 isoforms, long and short: What are they for? *Biochim Biophys Acta Bioenerg.* 1859(4), 263-269.

79. Wang, R., Mishra, P., Garbis, S.D., Moradian, A., Sweredoski, M.J., and Chan, D.C. (2021). Identification of new OPA1 cleavage site reveals that short isoforms regulate mitochondrial fusion. *Mol Biol Cell.* 32(2), 157-168.
80. Ge, Y., Shi, X., Boopathy, S., McDonald, J., Smith, A.W., and Chao, L.H. (2020). Two forms of Opa1 cooperate to complete fusion of the mitochondrial inner-membrane. *Elife.* 9, e50973.
81. Ishihara, N., Maeda, M., Ban, T., and Mihara, K. (2017). Cell-free mitochondrial fusion assay detected by specific protease reaction revealed Ca2+ as regulator of mitofusin-dependent mitochondrial fusion. *J Biochem.* 162(4), 287-294.
82. Busch, K.B., Kowald, A., and Spelbrink, J.N. (2014). Quality matters: how does mitochondrial network dynamics and quality control impact on mtDNA integrity? *Philos Trans R Soc Lond B Biol Sci.* 369(1646), 20130442.
83. Ferree, A.W., Trudeau, K., Zik, E., Benador, I.Y., Twig, G., Gottlieb, R.A., and Shirihai, O.S. (2013). MitoTimer probe reveals the impact of autophagy, fusion, and motility on subcellular distribution of young and old mitochondrial protein and on relative mitochondrial protein age. *Autophagy.* 9(11), 1887-1896.
84. Huang, J., Chen, L., Yao, Z., Sun, X., Tong, X., and Dong, S. (2023). The role of mitochondrial dynamics in cerebral ischemia-reperfusion injury. *Biomed Pharmacother.* 162, 114671.
85. Kumar, R., Bukowksi, M.J., Wider, J.M., Reynolds, C.A., Calo, L., Lepore, B., Tousignant, R., *et al.* (2016). Mitochondrial dynamics following global cerebral ischemia. *Mol Cell Neurosci.* 76, 68-75.
86. Nair, S., Leverin, A., Rocha-Ferreira, E., Sobotka, K.S., Thornton, C., Mallard, C., and Hagberg, H. (2022). Induction of mitochondrial fragmentation and mitophagy after neonatal hypoxia–ischemia. *Cells.* 11(7), 1193.
87. Wu, B., Luo, H., Zhou, X., Cheng, C., Lin, L., Liu, B., Liu, K., *et al.* (2017). Succinate-induced neuronal mitochondrial fission and hexokinase II malfunction in ischemic stroke: Therapeutical effects of kaempferol. *Biochim Biophys Acta Mol Basis Dis.* 1863(9), 2307-2318.
88. Li, X., Li, H., Xu, Z., Ma, C., Wang, T., You, W., Yu, Z., *et al.* (2022). Ischemia-induced cleavage of OPA1 at S1 site aggravates mitochondrial fragmentation and reperfusion injury in neurons. *Cell Death Dis.* 13(4), 321.
89. Kislin, M., Sword, J., Fomitcheva, I.V., Croom, D., Pryazhnikov, E., Lihavainen, E., Toptunov, D., *et al.* (2017). Reversible disruption of neuronal mitochondria by ischemic and traumatic injury revealed by quantitative two-photon imaging in the neocortex of anesthetized mice. *J Neurosci.* 37(2), 333-348.
90. Chouchani, E.T., Pell, V.R., Gaude, E., Aksentijevic, D., Sundier, S.Y., Robb, E.L., Logan, A., *et al.* (2014). Ischaemic accumulation of succinate controls reperfusion injury through mitochondrial ROS. *Nature.* 515(7527), 431-435.
91. Balog, J., Mehta, S.L., and Vemuganti, R. (2016). Mitochondrial fission and fusion in secondary brain damage after CNS insults. *J Cereb Blood Flow Metab.* 36(12), 2022-2033.
92. Lust, W.D., Taylor, C., Pundik, S., Selman, W.R., Ratcheson, R.A. (2002). Ischemic cell death: dynamics of delayed secondary energy failure during reperfusion following focal ischemia. *Metab Brain Dis.* 17(2), 113-121.

93. Liu, D., Ji, Q., Cheng, Y., Liu, M., Zhang, B., Mei, Q., Huan, M., and Zhou, S. (2022). Cyclosporine A loaded brain targeting nanoparticle to treat cerebral ischemia/reperfusion injury in mice. *J Nanobiotechnology.* 20(1), 256.
94. Wan, R., Fan, J., Song, H., Sun, W., and Yin, Y. (2022). Oxygen-glucose deprivation/reperfusion-induced Sirt3 reduction facilitated neuronal injuries in an apoptosis-dependent manner during prolonged reperfusion. *Neurochem Res.* 47(4), 1012-1024.
95. Flippo, K.H., Lin, Z., Dickey, A.S., Zhou, X., Dhanesha, N.A., Walters, G.C., Liu, Y., *et al.* (2020). Deletion of a neuronal Drp1 activator protects against cerebral ischemia. *J Neurosci.* 40(15), 3119-3129.
96. Grohm, J., Kim, S., Mamrak, U., Tobaben, S., Cassidy-Stone, A., Nunnari, J., Plesnila, N., *et al.* (2012). Inhibition of Drp1 provides neuroprotection in vitro and in vivo. *Cell Death Differ.* 19(9), 1446-1458.
97. Peng, C., Rao, W., Zhang, L., Wang, K., Hui, H., Wang, L., Su, N., *et al.* (2015). Mitofusin 2 ameliorates hypoxia-induced apoptosis via mitochondrial function and signaling pathways. *Int J Biochem Cell Biol.* 69, 29-40.
98. Peng, C., Rao, W., Zhang, L., Gao, F., Hui, H., Wang, K., Dai, S., *et al.* (2018). Mitofusin 2 exerts a protective role in ischemia reperfusion injury through increasing autophagy. *Cell Physiol Biochem.* 46(6), 2311-2324.
99. Sun, Y., Xue, W., Song, Z., Huang, K., and Zheng, L. (2016). Restoration of Opa1-long isoform inhibits retinal injury-induced neurodegeneration. *J Mol Med (Berl).* 94(3), 335-346.
100. Morgenstern, M., Stiller, S.B., Lubbert, P., Peikert, C.D., Dannenmaier, S, Drepper, F., Weill, U., *et al.* (2017). Definition of a high-confidence mitochondrial proteome at quantitative scale. *Cell Rep.* 19(13), 2836-2852.
101. Song, J., Herrmann, J.M., and Becker, T. (2021). Quality control of the mitochondrial proteome. *Nat Rev Mol Cell Biol.* 22(1), 54-70.
102. Pickles, S., Vigie, P., and Youle, R.J. (2018). The art of mitochondrial maintenance. *Curr Biol.* 28(4), R170-R185.
103. Deshwal, S., Fiedler, K.U., and Langer, T. (2020). Mitochondrial proteases: Multifaceted regulators of mitochondrial plasticity. *Annu Rev Biochem.* 89, 501-528.
104. Khalil, B., and Lievens, J-C. (2017). Mitochondrial quality control in amyotrophic lateral sclerosis: towards a common pathway? *Neural Regen Res.* 12(7), 1052-1061.
105. Eldeeb, M.A., Thomas, R.A., Ragheb, M.A., Fallahi, A., and Fon, E.A. (2022). Mitochondrial quality control in health and in Parkinson's disease. *Physiol Rev.* 102(4), 1721-1755.
106. Wu, Y., Hu, Q., Cheng, H., Yu, J., Gao, L., and Gao, G. (2023). USP30 impairs mitochondrial quality control and aggravates oxidative damage after traumatic brain injury. *Biochem Biophys Res Commun.* 671, 58-66.
107. Ashrafi, G., and Schwarz, T.L. (2013). The pathways of mitophagy for quality control and clearance of mitochondria. *Cell Death Differ.* 20(1), 31-42.
108. Sugiura, A., McLelland, G-L., Fon, E.A., and McBride, H.M. (2014). A new pathway for mitochondrial quality control: mitochondrial-derived vesicles. *EMBO J.* 33(19), 2142-2156.

109. Li, J., Yang, D., Li, Z., Zhao, M., Wang, D., Sun, Z., Wen, P. *et al.* (2023). PINK1/Parkin-mediated mitophagy in neurodegenerative diseases. *Ageing Res Rev.* 84, 101817.
110. Jin, S.M., Lazarou, M., Wang, C., Kane, L.A., Narendra, D.P., and Youle, R.J. (2010). Mitochondrial membrane potential regulates PINK1 import and proteolytic destabilization by PARL. *J Cell Biol.* 191(5), 933-942.
111. Matsuda, N., Sato, S., Shiba, K., Okatsu, K., Saisho, K., Gautier, C.A., Sou, Y., *et al.* (2010). PINK1 stabilized by mitochondrial depolarization recruits Parkin to damaged mitochondria and activates latent Parkin for mitophagy. *J Cell Biol.* 189(2), 211-221.
112. Narendra, D.P., Jin, S.M., Tanaka, A., Suen, D-F., Gautier, C.A., Shen, J., Cookson, M.R., *et al.* (2010). PINK1 Is selectively stabilized on impaired mitochondria to activate Parkin. *PLoS Biol.* 8(1), e1000298.
113. Okatsu, K., Koyano, F., Kimura, M., Kosako, H., Saeki, Y., Tanaka, K., and Matsuda, N. (2015). Phosphorylated ubiquitin chain is the genuine Parkin receptor. *J Cell Biol.* 209(1), 111-128.
114. Vives-Bauza, C., Zhou, C., Huang, Y., Cui, M., de Vries, R.L.A., Kim, J., May, J. *et al.* (2010). PINK1-dependent recruitment of Parkin to mitochondria in mitophagy. *Proc Natl Acad Sci U S A.* 107(1), 378-383.
115. Lazarou, M., Sliter, D.A., Kane, L.A., Sarraf, S.A., Wang, C., Burman, J.L., Sideris, D.P., *et al.* (2015). The ubiquitin kinase PINK1 recruits autophagy receptors to induce mitophagy. *Nature.* 524(7565), 309-314.
116. Kane, L.A., Lazarou, M., Fogel, A.I., Li, Y., Yamano, K., Sarraf, S.A., Bannerjee, S., *et al.* (2014). PINK1 phosphorylates ubiquitin to activate Parkin E3 ubiquitin ligase activity. *J Cell Biol.* 205(2), 143-153.
117. Kazlauskaite, A., Kondapalli, C., Gourlay, R., Campbell, D.G., Ritorto, M.S., Hofmann, K., *et al.* (2014). Parkin is activated by PINK1-dependent phosphorylation of ubiquitin at Ser65. *Biochem J.* 460(1), 127-139.
118. Koyano, F., Okatsu, K., Kosako, H., Tamura, Y., Go, E., Kimura, M., Kimura, Y., *et al.* (2014). Ubiquitin is phosphorylated by PINK1 to activate parkin. *Nature.* 510(7503), 162-166.
119. Geisler, S., Homstrom, K.M., Skujat, D., Fiesel, F.C., Rothfuss, O.C., Kahle, P.J., and Springer, W. (2010). PINK1/Parkin-mediated mitophagy is dependent on VDAC1 and p62/SQSTM1. *Nat Cell Biol.* 12(2), 119-131.
120. Vranas, M., Lu, Y., Rasool, S., Corteau, N., Krett, J.D., Sauve, V., Gehring, K., *et al.* (2022). Selective localization of Mfn2 near PINK1 enables its preferential ubiquitination by Parkin on mitochondria. *Open Biol.* 12(10, 210255.
121. Chan, N.C., Salazar, A.M., Pham, A.H., Sweredoski, M.J., Kolawa, N.J., Graham, R.L.J., Hess, S., *et al.* (2011). Broad activation of the ubiquitin–proteasome system by Parkin is critical for mitophagy. *Hum Mol Genet.* 20(9), 1726-1737.
122. Ordureau, A., Sarraf, S.A., Duda, D.M., Heo, J-M., Jedrychowski, M.P., Sviderskiy, V.O., Olszewski, J.L., *et al.* (2014). Quantitative proteomics reveal a feedforward mechanism for mitochondrial PARKIN translocation and ubiquitin chain synthesis. *Mol Cell.* 56(3), 360-375.
123. Yoshi, S.R., Kishi, C., Ishihara, N., and Mizushima, N. (2011). Parkin mediates proteasome-dependent protein degradation and rupture of the outer mitochondrial membrane. *J Biol Chem.* 286(22), 19630-19640.

124. Tanaka, A., Cleland, M.M., Xu, S., Narendra, D.P., Suen, D-F., Karbowski, M., and Youle, R.J. (2010). Proteasome and p97 mediate mitophagy and degradation of mitofusins induced by Parkin. *J Cell Biol.* 191(7), 1367-1380.
125. Nguyen, T.N., Padman, B.S., and Lazarou, M. (2016). Deciphering the molecular signals of PINK1/Parkin mitophagy. *Trends Cell Biol.* 26(10), 733-744.
126. Richard, T.J.C., Herzog, L.K., Vornberger, J., Rahmanto, A.S., Sangfelt, O., Salomons, F.A., and Dantuma, N.P. (2020). K63-linked ubiquitylation induces global sequestration of mitochondria. *Sci Rep.* 10(1), 22334.
127. Kataura, T., Otten, E.G., Rabanal-Ruiz, Y., Adriaenssens, E., Urselli, F., Scialo, F., Fan, L., *et al.* (2023). NDP52 acts as a redox sensor in PINK1/Parkin-mediated mitophagy. *EMBO J.* 42(5), 111372.
128. Nguyen, T.N., Sawa-Makarska, J., Khuu, G., Lam, W.K., Adriaenssens, E., Fracchiolla, D., Shoebridge, S., *et al.* (2023). Unconventional initiation of PINK1/Parkin mitophagy by Optineurin. *Mol Cell.* 83(10), 1693-1709.
129. Heo, J-M., Ordureau, A., Paulo, J.A., Rinehart, J., and Harper, J.W. (2015). The PINK1-PARKIN mitochondrial ubiquitylation pathway drives a program of OPTN/NDP52 recruitment and TBK1 activation to promote Mitophagy. *Mol Cell.* 60(1), 7-20.
130. Matsumoto, G., Shimogori, T., Hattori, N., and Nukina, N. (2015). TBK1 controls autophagosomal engulfment of polyubiquitinated mitochondria through p62/SQSTM1 phosphorylation. *Hum Mol Genet.* 24(15), 4429-4442.
131. Pickrell, A.M., and Youle, R.J. (2015). The roles of PINK1, parkin, and mitochondrial fidelity in Parkinson's disease. *Neuron.* 85(2), 257-273.
132. Vincow, E.S., Thomas, R.E., Merrihew, G.E., Shulman, N.J., Bammler, T.K., MacDonald, J.W., MacCoss, M.J., *et al.* (2019). Autophagy accounts for approximately one-third of mitochondrial protein turnover and is protein selective. *Autophagy.* 15(9), 1592-1605.
133. Stauch, K.L., Totusek, S., Trease, A.J., Estrella, L.D., Emanuel, K., Fangmeier, A., and Fox, H.S. (2023). Longitudinal in vivo metabolic labeling reveals tissue-specific mitochondrial proteome turnover rates and proteins selectively altered by parkin deficiency. *Sci Rep.* 13(1), 11414.
134. Goldsmith, J., Ordureau, A., Harper, J.W., and Holzbaur, E.L.F. (20220. Brain-derived autophagosome profiling reveals the engulfment of nucleoid-enriched mitochondrial fragments by basal autophagy in neurons. *Neuron.* 110(6), 967-976.
135. Lautenschlager, J., Wagner-Valladolid, S., Stephens, A.D., Fernandez-Villegas, A., Hockings, C., Mishra, A., Manton, J.D., *et al.* (2020). Intramitochondrial proteostasis is directly coupled to α-synuclein and amyloid β1-42 pathologies. *J Biol Chem.* 295(30), 10138-10152.
136. Maity, S., and Chakrabarti, O. (2021). Mitochondrial protein import as a quality control sensor. *Biol Cell.* 113(9), 375-400.
137. Wiedemann, N., and Pfanner, N. (2017). Mitochondrial machineries for protein import and assembly. *Annu Rev Biochem.* 86, 685-714.
138. Lysyk, L., Brassard, R., Touret, N., and Lemieux, M.J. (2020). PARL protease: A glimpse at intramembrane proteolysis in the inner mitochondrial membrane. *J Mol Biol.* 432(18), 5052-5062.

139. Alavai, M.V. (2021). OMA1-An integral membrane protease? *Biochim Biophys Acta Proteins Proteom.* 1869(2), 140558.
140. Peker, E., Weiss, K., Song, J., Zarges, C., Gerlich, S., Boehm, V., Trifunovic, A., *et al.* (2023). A two-step mitochondrial import pathway couples the disulfide relay with matrix complex I biogenesis. *J Cell Biol.* 222(7), e202210019.
141. Gibellini, L., De Gaetano, A., Mandrioli, M., Van Tongeren, E., Bortolotti, C.A., Cossarizza, A., and Pinti, M. (2020). The biology of Lonp1: More than a mitochondrial protease. *Int Rev Cell Mol Biol.* 354, 1-61.
142. Shin, C., Meng, S., Garbis, S.D., Moradian, A., Taylor, R.W., Sweredoski, M.J., Lomenick, B., *et al.* (2021). LONP1 and mtHSP70 cooperate to promote mitochondrial protein folding. *Nat Commun.* 12(1), 265.
143. Pryde, K.R., Taanman, J.W., and Schapira, A.H. (2016). A LON-ClpP proteolytic axis degrades complex I to extinguish ROS production in depolarized mitochondria. *Cell Rep.* 17(10), 2522-2531.
144. Bota, D.A., and Davies, K.J.A. (2002). Lon protease preferentially degrades oxidized mitochondrial aconitase by an ATP-stimulated mechanism. *Nat Cell Biol.* 4(9), 674-680.
145. Guo, X., Aviles, G., Liu, Y., Tian, R., Unger, B.A., Lin, Y-H.T., Wiita, A.P., *et al.* (2020). Mitochondrial stress is relayed to the cytosol by an OMA1-DELE1-HRI pathway. *Nature.* 579(7799), 427-432.
146. Rivera-Mejias, P., Narbona-Perez, A.J., Hasberg, L., Kroczek, L., Bahat, A., Lawo, S., Folz-Donahue, K., *et al.* (2023). The mitochondrial protease OMA1 acts as a metabolic safeguard upon nuclear DNA damage. *Cell Rep.* 42(4), 112332.
147. Zanini, G., Selleri, V., Malerba, M., Solodka, K., Sinigaglia, G., Nasi, M., Mattioli, A.V., *et al.* (2023). The role of Lonp1 on mitochondrial functions during cardiovascular and muscular diseases. *Antioxidants (Basel).* 12(3), 598.
148. Srinivasula, S.M., Gupta, S., Datta, P., Zhang, Z., Hegde, R., Cheong, N., Fernandes-Alnemri, T., *et al.* (2003). Inhibitor of apoptosis proteins are substrates for the mitochondrial serine protease Omi/HtrA2. *J Biol Chem.* 278(34), 31469-31472.
149. Hegde, R., Srinivasula, S.M., Zhang, Z., Wassell, R., Mukattash, R., Cilenti, L., *et al.* (2002). Identification of Omi/HtrA2 as a mitochondrial apoptotic serine protease that disrupts inhibitor of apoptosis protein-caspase interaction. *J Biol Chem.* 277(1), 432-438.
150. Suzuki, Y., Takahashi-Niki, K., Akagi, T., Hashikawa, T., and Takahashi, R. (2004). Mitochondrial protease Omi/HtrA2 enhances caspase activation through multiple pathways. *Cell Death Differ.* 11(2), 208-216.
151. Wojtyniak, P., Boratynska-Jasinska, A., Serwach, K., Ruszczynska-Biegala, J., Zablocka, B., Jaworski, J., and Kawalec, M. (2022). Mitofusin 2 integrates mitochondrial network remodelling, mitophagy, and renewal of respiratory chain proteins in neurons after oxygen and glucose deprivation. *Mol Neurobiol.* 59(10), 6502-6518.
152. Wider, J.M., Gruley, E., Morse, P.T., Wan, J., Lee, I., Anzell, A.R., Fogo, G.M., *et al.* (2023). Modulation of mitochondrial function with near-infrared light reduces brain injury in a translational model of cardiac arrest. *Crit Care.* 27(1), 491.
153. Zhang, X., Yan, H., Yuan, Y., Gao, J., Shen, Z., Cheng, Y., Shen, Y., *et al.* (2013). Cerebral ischemia-reperfusion-induced autophagy protects against neuronal injury by mitochondrial clearance. *Autophagy.* 9(9), 1321-1333.

154. Zuo, W., Zhang, S., Xia, C-Y., Guo, X-F., He, W-B., and Chen, N-H. (2014). Mitochondria autophagy is induced after hypoxic/ischemic stress in a Drp1 dependent manner: the role of inhibition of Drp1 in ischemic brain damage. *Neuropharmacology.* 86, 103-115.
155. Lan, R., Wu, J-T., Wu, T., Ma, Y-Z., Wang, B-Q., Zheng, H-Z., Li, Y-N., *et al.* (2018). Mitophagy is activated in brain damage induced by cerebral ischemia and reperfusion via the PINK1/Parkin/p62 signalling pathway. *Brain Res Bull.* 142, 63-77.
156. Zhang, X., Wei, M., Fan, J., Yan, W., Zha, X., Song, H., Wan, R., *et al.* (2021). Ischemia-induced upregulation of autophagy preludes dysfunctional lysosomal storage and associated synaptic impairments in neurons. *Autophagy.* 17(6), 1519-1542.
157. Wen, Y., Gu, Y., Tang, X., and Hu, Z. (2020). PINK1 overexpression protects against cerebral ischemia through Parkin regulation. *Environ Toxicol.* 35(2), 188-193.
158. Tang, J., Hu, Z., Tan, J., Yang, S., and Zeng, L. (2016). Parkin protects against oxygen-glucose deprivation/reperfusion insult by promoting Drp1 degradation. *Oxid Med Cell Longev.* 2016, 8474303.
159. Wen, H., Zuo, Y., Li, L., Zhan, L., Xue, J., Sun, W., and Xu, E. (2023). Hypoxic postconditioning restores mitophagy against transient global cerebral ischemia via Parkin-induced posttranslational modification of TBK1. *Neurobiol Dis.* 179, 106043.
160. Mao, Z., Tian, L., Liu, J., Wu, Q., Wang, N., Wang, G., Wang, Y., *et al.* (2022). Ligustilide ameliorates hippocampal neuronal injury after cerebral ischemia reperfusion through activating PINK1/Parkin-dependent mitophagy. *Phytomedicine.* 101, 154111.
161. Cai, Y., Yang, E., Yao, X., Zhang, X., Wang, Q., Wang, Y., Liu, J., *et al.* (2021). FUNDC1-dependent mitophagy induced by tPA protects neurons against cerebral ischemia-reperfusion injury. *Redox Biol.* 38, 101792.
162. Guo, Y., Jiang, H., Wang, M., Ma, Y., Zhang, J., and Jing, L. (2023). Metformin alleviates cerebral ischemia/reperfusion injury aggravated by hyperglycemia via regulating AMPK/ULK1/PINK1/Parkin pathway-mediated mitophagy and apoptosis. *Chem Biol Interact.* 384, 110723.
163. Li, Z., and Xing, J. (2023). Contribution and therapeutic value of mitophagy in cerebral ischemia-reperfusion injury after cardiac arrest. *Biomed Pharmacother.* 167, 115492.
164. Shi, R-Y., Zhu, S-H., Li, V., Gibson, S.B., Xu, X-S., and Kong J-M. (2014). BNIP3 interacting with LC3 triggers excessive mitophagy in delayed neuronal death in stroke. *CNS Neurosci Ther.* 20(12), 1045-1055.
165. Feng, J., Chen, X., Guan, B., Li, C., Qiu, J., and Shen, J. (2018). Inhibition of peroxynitrite-induced mitophagy activation attenuates cerebral ischemia-reperfusion injury. *Mol Neurobiol.* 55(8), 6369-6386.
166. Yu, S., Zheng, S., Leng, J., Wang, S., Zhao, T., and Liu, J. (2016). Inhibition of mitochondrial calcium uniporter protects neurocytes from ischemia/reperfusion injury via the inhibition of excessive mitophagy. *Neurosci Lett.* 628, 24-29.
167. Zheng, Y., Zhang, X., Wu, X., Jiang, L., Ahsan, A., Ma, S., Xiao, Z., *et al.* (2019). Somatic autophagy of axonal mitochondria in ischemic neurons. *J Cell Biol.* 218(6), 1891-1907.
168. Gala, M.G-F., and Vogtle, F-N. (2021). Mitochondrial proteases in human diseases. *FEBS Lett.* 595(8), 1205-1222.

169. Hori, O., Ichinoda, F., Tamatani, T., Yamaguchi, A., Sato, N., Ozawa, K., Kitao, Y., *et al.* (2002). Transmission of cell stress from endoplasmic reticulum to mitochondria: enhanced expression of Lon protease. *J Cell Biol.* 157(7), 1151-1160.
170. You, H., Jin, Y., Kang, J., Mao, Y., Su, J., Sun, L., Wang, L., *et al.* (2020). Mitochondrial serine protease Omi/HtrA2 accentuates brain ischemia/reperfusion injury in rats and oxidative stress injury in vitro by modulating mitochondrial stress proteins CHOP and ClpP and physically interacting with mitochondrial fusion protein OPA1. *Bioengineered.* 11(1), 1058-1070.
171. Althaus, J., Siegelin, M.D., Dehghani, F., Cilenti, L., Zervos, A.S., and Rami, A. (2007). The serine protease Omi/HtrA2 is involved in XIAP cleavage and in neuronal cell death following focal cerebral ischemia/reperfusion. *Neurochem Int.* 50(1), 172-180.
172. Yoshioka, H., Katsu, M., Sakata, H., Okami, N., Wakai, T., Kinouchi, H., and Chan, P.H. (2013). The role of PARL and HtrA2 in striatal neuronal injury after transient global cerebral ischemia. *J Cereb Blood Flow Metab.* 33(11), 1658-1665.
173. Li, X., Li, H., Xu, Z., Ma, C., Wang, T., You, W., Yu, Z., *et al.* (2022). The role of PARL and HtrA2 in striatal neuronal injury after transient global cerebral ischemia. *Cell Death Dis.* 13(4), 321.
174. Baburamani, A.A., Hurling, C., Stolp, H., Sobotka, K., Gressens, P., Hagberg, H., and Thornton, C. (2015). Mitochondrial Optic Atrophy (OPA) 1 processing is altered in response to neonatal hypoxic-ischemic brain injury. *Int J Mol Sci.* 16(9), 22509-22526.
175. Sepuri, N.B.V., Angireddy, R., Srinivasan, S., Guha, M., Spear, J., Lu, B., Anandatheerthavarada, HK., *et al.* (2017). Mitochondrial LON protease-dependent degradation of cytochrome c oxidase subunits under hypoxia and myocardial ischemia. *Biochim Biophys Acta Bioenerg.* 1858(7), 519-528.
176. Kaufman, D.M., and Crowder, C.M. (2015). Mitochondrial proteostatic collapse leads to hypoxic injury. *Curr Biol.* 25(16), 2171-2176.
177. MacVicar, T., Ohba, Y., Nolte, H., Mayer, FC., Tatsuta, T., Sprenger, H., Lindner, B., *et al.* (2019). Lipid signalling drives proteolytic rewiring of mitochondria by YME1L. *Nature.* 575(7782), 361-365.
178. Yan, J., Sun, C., Shin, S., Van Gilst, M., and Crowder, C.M. (2021). Effect of the mitochondrial unfolded protein response on hypoxic death and mitochondrial protein aggregation. *Cell Death Dis.* 12(7), 711.
179. Twig, G., and Shirihai, O.S. (2011). The interplay between mitochondrial dynamics and mitophagy. *Antioxid Redox Signal.* 14(10), 1939-1951.
180. Shirihai, O.S., Song, M., and Dorn III, G.W. (2015). How mitochondrial dynamism orchestrates mitophagy. *Circ Res.* 116(11), 1835-1849.
181. Frank, M., Duvezin-Caubet, S., Koob, S., Occhinpinti, A., Jagasia, R., Petcherski, A., Ruonala, M.O., *et al.* (2012). Mitophagy is triggered by mild oxidative stress in a mitochondrial fission dependent manner. *Biochim Biophys Acta.* 1823(12), 2297-2310.
182. Chen, N., Guo, Z., Luo, Z., Zheng, F., Shao, W., Yu, G., Cai, P., *et al.* (2021). Drp1-mediated mitochondrial fission contributes to mitophagy in paraquat-induced neuronal cell damage. *Environ Pollut.* 272, 116413.
183. Gomes, L.C., and Scorrano, L. (2008). High levels of Fis1, a pro-fission mitochondrial protein, trigger autophagy. *Biochim Biophys Acta.* 1777(7-8), 860-866.

184. Twig, G., Elorza A., Molina, A.J.A., Mohamed, H., Wikstrom, J.D., Walzer, G., Stiles, L., *et al.* (2008). Fission and selective fusion govern mitochondrial segregation and elimination by autophagy. *EMBO J.* 27(2), 433-446.
185. Dagda, R.K., Cherra 3rd, S.J., Kulich, S.M., Tandon, A., Park, D., and Chu, C.T. (2009). Loss of PINK1 function promotes mitophagy through effects on oxidative stress and mitochondrial fission. *J Biol Chem.* 284(20), 13843-13855.
186. Kageyama, Y., Hoshijima, M., Seo, K., Bedja, D., Sysa-Shah, P., Andrabi, S.A., Chen, W., *et al.* (2014). Parkin-independent mitophagy requires Drp1 and maintains the integrity of mammalian heart and brain. *EMBO J.* 33(23), 2798-2813.
187. Burman, J.L., Pickles, S., Wang, C., Sekine, S., Vargas, J.N.S., Zhang, Z., Youle, A.M., *et al.* (2017). Mitochondrial fission facilitates the selective mitophagy of protein aggregates. *J Cell Biol.* 216(10), 3231-3247.
188. Konig, T., Nolte, H., Aaltonen, M.J., Tatsuta, T., Krols, M., Stroh, T., Langer, T., *et al.* (2021). MIROs and DRP1 drive mitochondrial-derived vesicle biogenesis and promote quality control. *Nat Cell Biol.* 23(12), 1271-1286.
189. Lee, T-T., Chen, P-L., Su, M.P., Li, J-C., Chang, Y-W., Liu, R-W., Juan H-F., *et al.* (2021). Loss of Fis1 impairs proteostasis during skeletal muscle aging in Drosophila. *Aging Cell.* 20(6), e13379.
190. McLelland, G-L., Goiran, T., Yi, W., Dorval, G., Chen, C.X., Lauinger, N.D., Krahn, A.I., *et al.* (2018). Mfn2 ubiquitination by PINK1/parkin gates the p97-dependent release of ER from mitochondria to drive mitophagy. *Elife.* 7, e32866.
191. Hailey, D.W., Kim, P.K., Satpute-Krishnan, P., Rambold, A.S., Mitra, K., Sougrat, R., and Lippincott-Schwartz, J. (2010). Mitochondria supply membranes for autophagosome biogenesis during starvation. *Cell.* 141(4), 656-667.
192. Park, K-S., Wiederkehr, A., Kirkpatrick, C., Mattengerger, Y., Martinou, J-C., Marchetti, P., Demaruex, N., *et al.* (2008). Selective actions of mitochondrial fission/fusion genes on metabolism-secretion coupling in insulin-releasing cells. *J Biol Chem.* 283(48), 33347-33356.
193. Kulek, A.R., Anzell, A., Wider, J.M., Sanderson, T.H., and Przyklenk, K. (2020). Mitochondrial quality control: role in cardiac models of lethal ischemia-reperfusion injury. *Cells*. 9, 214.
194. Calo, L., Dong, Y., Kumar, R., Przyklenk, K., and Sanderson, T.H. (2013). Mitochondrial dynamics: an emerging paradigm in ischemia-reperfusion injury. *Curr Pharm Des.* 19, 6848–6857.
195. Hoppins, S., Lackner, L., and Nunnari, J. (2007). The machines that divide and fuse mitochondria. *Annu Rev Biochem* 76, 751–780.
196. Twig, G., Hyde, B., and Shirihai, O.S. (2008). Mitochondrial fusion, fission and autophagy as a quality control axis: the bioenergetic view. *Biochim Biophys Acta.* 1777, 1092–1097.
197. Malena, A., Loro, E., Di Re, M., Holt, I.J., and Vergani, L. (2009). Inhibition of mitochondrial fission favours mutant over wild-type mitochondrial DNA. *Hum Mol Genet.* 18, 3407–3416.
198. Suen, D.F., Narendra, D.P., Tanaka, A., Manfredi, G., and Youle, R.J. (2010). Parkin overexpression selects against a deleterious mtDNA mutation in heteroplasmic cybrid cells. *Proc Natl Acad Sci U S A.* 107, 11835–11840.

199. Partikian, A., Olveczky, B., Swaminathan, R., Li, Y., and Verkman, A.S. (1998). Rapid diffusion of green fluorescent protein in the mitochondrial matrix. *J Cell Biol.* 140, 821–829.
200. Ono, T., Isobe, K., Nakada, K., and Hayashi, J.I. (2001). Human cells are protected from mitochondrial dysfunction by complementation of DNA products in fused mitochondria. *Nat Genet*. 28, 272–275.
201. Busch, K.B., Bereiter-Hahn, J., Wittig, I., Schagger, H., and Jendrach, M. (2006). Mitochondrial dynamics generate equal distribution but patchwork localization of respiratory complex I. *Mol Membr Biol*. 23, 509–520.
202. Horbay, R., and Bilyy, R. (2016). Mitochondrial dynamics during cell cycling. *Apoptosis.* 21, 1327–1335.
203. Frank, S., Gaume, B., Bergmann-Leitner, E.S., Leitner, W.W., Robert, E.G., Catez, F., Smith, C.L., *et al.* (2001). The role of dynamin-related protein 1, a mediator of mitochondrial fission, in apoptosis. *Dev Cell*. 1, 515–525.
204. Margineantu, D.H., and Hockenbery, D.M. (2016). Mitochondrial functions in stem cells. *Curr Opin Genet Dev*. 38, 110–117.
205. Wai, T., and Langer, T. (2016). Mitochondrial dynamics and metabolic regulation. *Trends Endocrinol Metab*. 27, 105–117.
206. Youle, R.J., and van der Bliek, A.M. (2012). Mitochondrial fission, fusion, and stress. *Science.* 337, 1062–1065.
207. Prieto, J., Leon, M., Ponsoda, X., Sendra, R., Bort, R., Ferrer-Lorente, R., Raya, A., *et al.* (2016) .Early ERK1/2 activation promotes DRP1-dependent mitochondrial fission necessary for cell reprogramming. *Nat Commun*. 7, 11124.
208. Molina, A.J., Wikstrom, J.D., Stiles, L., Las, G., Mohamed, H., Elorza, A., Walzer, G., *et al.* (2009). Mitochondrial networking protects beta-cells from nutrient-induced apoptosis. *Diabetes*. 58, 2303–2315.
209. Zahedi, A., On, V., Phandthong, R., Chaili, A., Remark, G., Bhanu, B., and Talbot, P. (2018). Deep analysis of mitochondria and cell health using machine learning. *Sci Rep*. 8, 16354.
210. Reis, Y., Bernardo-Faura, M., Richter, D., Wolf, T., Brors, B., Hamacher-Brady, A., Elis, R., *et al.* (2012). Multi-parametric analysis and modeling of relationships between mitochondrial morphology and apoptosis. *PLoS One*. 7, e28694.
211. Giedt, R.J., Feruglio, P.F., Pathania, D., Yang, K.S., Kilcoyne, A., Viengoni, C., Mitchison, T.J., *et al.* (2016). Computational imaging reveals mitochondrial morphology as a biomarker of cancer phenotype and drug response. *Sci Rep*. 6, 32985.
212. Leonard, A.P., Cameron, R.B., Speiser, J.L., Wolf, B.J., Peterson, Y.K., Schnellmann, R.G., *et al.* (2015). Quantitative analysis of mitochondrial morphology and membrane potential in living cells using high-content imaging, machine learning, and morphological binning. *Biochim Biophys Acta*. 1853, 348–360.
213. Schindelin, J., Arganda-Carreras, I., Frise, E., Kaynig, V., Longair, M., Pietzsch, T., Preibisch, S., Rueden, C., *et al.* (2012). Fiji: an open-source platform for biological-image analysis. *Nat Methods*. 9, 676–682.
214. Kuhn, M. (2008). Building predictive models in R using the caret package. *J Stat Softw*. 28, 1–26.

215. R Core Team. R: A Language and Environment for Statistical Computing. R Foundation for Statistical Computing, Vienna, Austria (accessed 27 Jan 2020, 2019). https://www.R-project.org/.
216. Lee, H., and Yoon, Y. (2018). Mitochondrial membrane dynamics-functional positioning of OPA1. *Antioxidants (Basel)*. 7, 186.
217. MacVicar, T., and Langer, T. (2016). OPA1 processing in cell death and disease—the long and short of it. *J Cell Sci*. 129, 2297–2306.
218. Duvezin-Caubet, S., Jagasia, R., Wagener, J., Hofmann, S., Trifunovic, A., Hansson, A., Chomyn, A., *et al.* (2006). Proteolytic processing of OPA1 links mitochondrial dysfunction to alterations in mitochondrial morphology. *J Biol Chem*. 281, 37972–37979.
219. Piquereau, J., Caffin, F., Novotova, M., Prola, A., Garnier, A., Mateo, P., Fortin, D., Huynh, L.H., *et al.* (2012). Down-regulation of OPA1 alters mouse mitochondrial morphology, PTP function, and cardiac adaptation to pressure overload. *Cardiovasc Res*. 94, 408–417.
220. Ishihara, N., Fujita, Y., Oka, T., and Mihara, K. (2006). Regulation of mitochondrial morphology through proteolytic cleavage of OPA1. *EMBO J*. 25, 2966–2977.
221. Cho, B., Choi, S.Y., Cho, H.M., Kim, H.J., and Sun, W. (2013). Physiological and pathological significance of dynamin-related protein 1 (drp1)-dependent mitochondrial fission in the nervous system. *Exp Neurobiol*. 22, 149–157.
222. Reddy, P.H., Reddy, T.P., Manczak, M., Calkins, M.J., Shirendeb, U., and Mao, P. (2011). Dynamin-related protein 1 and mitochondrial fragmentation in neurodegenerative diseases. *Brain Res Rev*. 67, 103–118.
223. Rambold, A.S., Kostelecky, B., Elia, N., and Lippincott-Schwartz, J. (2011). Tubular network formation protects mitochondria from autophagosomal degradation during nutrient starvation. *Proc Natl Acad Sci U S A*. 108, 10190–10195.
224. Mishra, J., Davani, A.J., Natarajan, G.K., Kwok, W-M., Stowe, D.F., and Camara, A.K.S. (2019). Cyclosporin A increases mitochondrial buffering of calcium: an additional mechanism in delaying mitochondrial permeability transition pore opening. *Cells*. 8, 1052.
225. Kwong, J.Q., and Molkentin, J.D. (2015). Physiological and pathological roles of the mitochondrial permeability transition pore in the heart. *Cell Metab*. 21, 206–214.
226. Park, J.Y., Jang, S.Y., Shin, Y.K., Koh, H., Suh, D.J., Shinji, T., Araki, T., *et al.* (2013). Mitochondrial swelling and microtubule depolymerization are associated with energy depletion in axon degeneration. *Neuroscience*. 238, 258–269.
227. Minamikawa, T., Williams, D.A., Bowser, D.N., and Nagley, P. (1999). Mitochondrial permeability transition and swelling can occur reversibly without inducing cell death in intact human cells. *Exp Cell Res*. 246, 26–37.
228. Kobayashi, T., Kuroda, S., Tada, M., Houkin, K., Iwasaki, Y., and Abe, H. (2003). Calcium-induced mitochondrial swelling and cytochrome c release in the brain: its biochemical characteristics and implication in ischemic neuronal injury. *Brain Res*. 960, 62–70.
229. Li, J., Ma, X., Yu, W., Lou, Z., Mu, D., Wang, Y., Shen, B., and Qi, S. (2012). Reperfusion promotes mitochondrial dysfunction following focal cerebral ischemia in rats. *PLoS One*. 7, e46498.

230. Lemasters, J.J., Theruvath, T.P., Zhong, Z., and Nieminen, A.L. (2009). Mitochondrial calcium and the permeability transition in cell death. *Biochim Biophys Acta*. 1787, 1395–1401.
231. Liu, X., Xu, S., Wang, P., and Wang, W. (2015). Transient mitochondrial permeability transition mediates excitotoxicity in glutamate-sensitive NSC34D motor neuron-like cells. *Exp Neurol*. 271, 122–130.
232. Brustovetsky, T., Li, V., and Brustovetsky, N. (2009). Stimulation of glutamate receptors in cultured hippocampal neurons causes Ca2+-dependent mitochondrial contraction. *Cell Calcium*. 46, 18–29.
233. Zazueta, C., Sosa-Torres, M.E., Correa, F., and Garza-Ortiz, A. (1999). Inhibitory properties of ruthenium amine complexes on mitochondrial calcium uptake. *J Bioenerg Biomembr*. 31, 551–557.
234. Zhao, L., Li, S., Wang, S., Yu, N., and Liu, J. (2015). The effect of mitochondrial calcium uniporter on mitochondrial fission in hippocampus cells ischemia/reperfusion injury. *Biochem Biophys Res Commun*. 461, 537–542.
235. Crompton, M., Ellinger, H., and Costi, A. (1988). Inhibition by cyclosporin A of a Ca2+-dependent pore in heart mitochondria activated by inorganic phosphate and oxidative stress. *Biochem J.* 255, 357–360.
236. Broekemeier, K.M., Dempsey, M.E., and Pfeiffer, D.R. (1989). Cyclosporin A is a potent inhibitor of the inner membrane permeability transition in liver mitochondria. *J Biol Chem*. 264, 7826–7830.
237. Halestrap, A.P., Connern, C.P., Griffiths, E.J., and Kerr, P.M. (1997). Cyclosporin A binding to mitochondrial cyclophilin inhibits the permeability transition pore and protects hearts from ischaemia/reperfusion injury. *Mol Cell Biochem*. 174, 167–172.
238. Kowaltowski, A.J., Menezes-Filho, S.L., Assali, E.A., Goncalves, I.G., Cabral-Costa, J.V., Abreu, P., Miller, N., *et al.* (2019). Mitochondrial morphology regulates organellar Ca^{2+} uptake and changes cellular Ca^{2+} homeostasis. *FASEB J*. 33, 13176–13188.
239. Legland, D., Arganda-Carreras, I., and Andrey, P. (2016). MorphoLibJ: integrated library and plugins for mathematical morphology with ImageJ. *Bioinformatics*. 32, 3532–3534.
240. Arganda-Carreras, I., Kaynig, V., Rueden, C., Eliceiri, K.W., Schindelin, J., Cardona, A., and Seung, H.S. (2017). Trainable Weka segmentation: a machine learning tool for microscopy pixel classification. *Bioinformatics*. 33, 2424–2426.
241. Kan, A. (2017). Machine learning applications in cell image analysis. *Immunol Cell Biol*. 95, 525–530.
242. Wakabayashi, J., Zhang, Z., Wakabayashi, N., Tamura, Y., Fukaya, M., Kensler, T.W., Iijima, M., *et al.* (2009). The dynamin-related GTPase Drp1 is required for embryonic and brain development in mice. *J Cell Biol*. 186, 805–816.
243. Cogliati, S., Frezza, C., Soriano, M.E., Varanita, T., Quintana-Carbrera, R., Corrado, M., Cipolat, S., *et al.* (2013). Mitochondrial cristae shape determines respiratory chain supercomplexes assembly and respiratory efficiency. *Cell.* 155(1), 160-171.
244. Reza, A.M. (2004). Realization of the contrast limited adaptive histogram equalization (CLAHE) for real-time image enhancement. *J VLSI Sig Proc Syst.* 38, 35–44.

245. Sanabria, C. & Lee, P. J. In Handbook of Superconducting Materials (ed. Cardwell, D. A.) (Taylor and Francis, 2003).
246. Ollion, J., Cochennec, J., Loll, F., Escudé, C., and Boudier, T. (2013). TANGO: a generic tool for high-throughput 3D image analysis for studying nuclear organization. *Bioinformatics*. 29, 1840–1841.
247. Willems, P.H.G.M., Rossignol, R., Dietern, C.E.J., Murphy. M.P., and Koopman, W.J.H. (2015). Redox homeostasis and mitochondrial dynamics. *Cell Metab.* 22(2), 207-218.
248. Bomba-Warczak, E., Edassery, S.L., Hark, T.J., and Savas, J.N. (2021). Long-lived mitochondrial cristae proteins in mouse heart and brain *J Cell Biol*. 220(9), e202005193.
249. Krishna, S., Drigo, R.A.E., Capitanio, J.S., Ramachandra, R., Ellisman, M., Hetzer, M.W. (2021). Identification of long-lived proteins in the mitochondria reveals increased stability of the electron transport chain. *Dev Cell.* 56(21), 2952-2965.
250. Cadenas, E., and Davies, K.J. (2000). Mitochondrial free radical generation, oxidative stress, and aging. *Free Radic Biol Med*. 29(3-4), 222-230.
251. Liu, S., Liu, S., and Jiang, H. (2022). Multifaceted roles of mitochondrial stress responses under ETC dysfunction - repair, destruction and pathogenesis. *FEBS J*. 289(22), 6994-7013.
252. Perkins, G.D., Callway, C.W., Haywood, K., Neumar, R.W., Lilja, G., Rowland, M.J., Sawyer, K.N., *et al.* (2021). Brain injury after cardiac arrest. *Lancet.* 398(10307), 1269-1278.
253. Kalogeris, T., Baines, C.P., Krenz, M., and Korthuis, R.J. (2012). Cell biology of ischemia/reperfusion injury. *Int Rev Cell Mol Biol.* 298, 229-317.
254. Hüttemann, M., Helling, S., Sanderson, T.H., Sinkler, C., Samavati, L., Mahapatra, G., Varughese, A., *et al.* (2012). Regulation of mitochondrial respiration and apoptosis through cell signaling: cytochrome c oxidase and cytochrome c in ischemia/reperfusion injury and inflammation. *Biochim Biophys Acta.* 1817(4), 598-609.
255. Guerra-Castellano, A., Diaz-Quintana, A., Perez-Mejias, G., Elena-Real, C.A., Gonzalez-Arzola, K., Garcia-Maurina, S.M., De la Rosa, M., *et al.* (2018). Oxidative stress is tightly regulated by cytochrome c phosphorylation and respirasome factors in mitochondria. *Proc Natl Acad Sci U S A.* 115(31), 7955-7960.
256. Kalpage, H.A., Wan, J., Morse, P.T., Zurek, M.P., Turner, A.A., Khobeir, A., Yazdi, N., *et al.* (2020). Cytochrome c phosphorylation: Control of mitochondrial electron transport chain flux and apoptosis. *Int J Biochem Cell Biol.* 121, 105704.
257. Prabu, S.K., Anandatheerthavarada, H.K., Raza, H., Srinivasan, S., Spear, J.F., and Avadhani, N.G. (2006). Protein kinase A-mediated phosphorylation modulates cytochrome c oxidase function and augments hypoxia and myocardial ischemia-related injury. *J Biol Chem.* 281(4), 2061-70.
258. Chouchani, E.T., Pell, V.R., James, A.M., Work, L.M., Sae-Parsy, K., Frezza, C., Krieg, T., *et al.* (2016). A unifying mechanism for mitochondrial superoxide production during ischemia-reperfusion injury. *Cell Metab.* 23(2), 254-263.
259. Kim, M., Stepanova, A., Niatsetskaya, Z., Sosunov, S., Arndt, S., Murphy, M.P., Galkin, A., *et al.* (2018). Attenuation of oxidative damage by targeting mitochondrial complex I in neonatal hypoxic-ischemic brain injury. *Free Radic Biol Med.* 124, 517-524.

260. Zhang, G., Wang, X., Li, C., Li, Q., An, Y.A., Luo, X., Deng, Y., *et al.* (2021). Integrated stress response couples mitochondrial protein translation with oxidative stress control. *Circulation.* 144(18), 1500-1515.
261. Wang, H., Liu, C., Zhao, Y., and Gao, G. (2020). Mitochondria regulation in ferroptosis. *Eur J Cell Biol.* 99(1), 151058.
262. Wang, P., Cui, Y., Ren, Q., Yan, B., Zhao, Y., Yu, P., Gao, G., *et al.* (2021). Mitochondrial ferritin attenuates cerebral ischaemia/reperfusion injury by inhibiting ferroptosis. *Cell Death Dis*. 12(5), 447.
263. Bulteau, A., Szweda, L.I., and Friguet, B. (2006). Mitochondrial protein oxidation and degradation in response to oxidative stress and aging. *Exp Gerontol.* 41(7), 653-7.
264. Paradies, G., Petrosillo, G., Paradies, V., and Ruggiero, F.M. (2009). Role of cardiolipin peroxidation and Ca2+ in mitochondrial dysfunction and disease. *Cell Calcium.* 45(6), 643-50.
265. Yang, J., Mukda, S., and Chen, S. (2018). Diverse roles of mitochondria in ischemic stroke. *Redox Biol*. 16, 263-275.
266. Kaur, M., and Sharma, S. (2022). Mitochondrial repair as potential pharmacological target in cerebral ischemia. *Mitochondrion.* 63, 23-31.
267. Hernandez, G., Thornton, C., Stotland, A., Lui, D., Sin, J., Ramil, J., Magee, N., *et al.* (2013). MitoTimer: a novel tool for monitoring mitochondrial turnover. *Autophagy.* 9(11), 1852-1861.
268. Wilson, R.J., Drake, J.C., Cui, D., Zhang, M., Perry, H.M., Kashatus, J.A., Kusminski, C.M., *et al.* (2019). Conditional MitoTimer reporter mice for assessment of mitochondrial structure, oxidative stress, and mitophagy. *Mitochondrion.* 44, 20-26.
269. Xie, Y., Zhang, Y., Sun, A., Peng, Y., Hou, W., Xiang, C., Zhang, G., *et al.* (2022). The coupling of mitoproteolysis and oxidative phosphorylation enables tracking of an active mitochondrial state through MitoTimer fluorescence. *Redox Biol*. 56, 102447.
270. Lee, J., Pandey, A.K., Venkatesh, S., Thilagavathi, J., Honda, T., Singh, K., and Suzuki, C.K. (2022). Inhibition of mitochondrial LonP1 protease by allosteric blockade of ATP binding and hydrolysis via CDDO and its derivatives. *J Biol Chem.* 298(3), 101719.
271. Yang, Q., Liu, P., Anderson, N.S., Shpilka, T., Du, Y., Naresh, N.U., Li, R., *et al.* (2022). LONP-1 and ATFS-1 sustain deleterious heteroplasmy by promoting mtDNA replication in dysfunctional mitochondria. *Nat Cell Biol.* 24(2), 181-193.
272. Wang, S., Tan, J., Miao, Y., and Zhang, Q. (2022). Mitochondrial dynamics, mitophagy, and mitochondria-endoplasmic reticulum contact sites crosstalk under hypoxia. *Front Cell Dev Biol.* 10, 848214.
273. Anzell, A.R., Fogo, G.M., Gurm, Z., Raghunayakula, S., Wider, J.M., Maheras, K.J., Emaus, K.J., *et al.* (2021). Mitochondrial fission and mitophagy are independent mechanisms regulating ischemia/reperfusion injury in primary neurons. *Cell Death Dis.* 12(5), 475.
274. Li, Q., Zhang, T., Wang, J., Zhang, Z., Zhai, Y., Yang, G., and Sun, X. (2014). Rapamycin attenuates mitochondrial dysfunction via activation of mitophagy in experimental ischemic stroke. *Biochem Biophys Res Commun.* 444(2), 182-188.

275. Sheng, R., Zhang, L., Han, R., Liu, X., Gao, B., and Qin, Z. (2010). Autophagy activation is associated with neuroprotection in a rat model of focal cerebral ischemic preconditioning. *Autophagy.* 6(4), 482-494.
276. Naresh, N.U., and Haynes, C.M. (2019). Signaling and regulation of the mitochondrial unfolded protein response. *Cold Spring Harb Perspect Biol.* 11(6), a033944.
277. Xiaowei, X., Qian, X., and Dingzhou, Z. (2023). Sirtuin-3 activates the mitochondrial unfolded protein response and reduces cerebral ischemia/reperfusion injury. *Int J Biol Sci.* 19(13), 4327-4339.
278. Pena, S., Sherman, T., Brookes, P.S., and Nehrke, K. (2016). The mitochondrial unfolded protein response protects against anoxia in Caenorhabditis elegans. *PLoS One.* 11(7), e0159989.
279. Zhou, Z., Fan, Y., Zong, R., and Tan, K. (2022). The mitochondrial unfolded protein response: A multitasking giant in the fight against human diseases. *Ageing Res Rev.* 81, 101702.
280. Terskikh, A., Fradkov, A., Ermakova, G., Zaraisky, A., Tan, P., Kajava, A.V., Zhao, X., *et al.* (2000). "Fluorescent timer": protein that changes color with time. *Science.* 290(5496), 1585-1589.
281. Tanaka, K. (2020). The PINK1-Parkin axis: An overview. *Neurosci Res.* 159, 9-15.
282. Quinn, P.M.J., Moreira, P.I., Ambrosio, A.F., and Alves, C.H. (2020). PINK1/PARKIN signalling in neurodegeneration and neuroinflammation. *Acta Neuropathol Commun.* 8(1), 189.
283. Watzlawik, J.O., Fiesel, F.C., Fiorino, G., Bustillos, B.A., Baninameh, Z., Markham, B.N., Hou, X., *et al.* (2023). Basal activity of PINK1 and PRKN in cell models and rodent brain. *Autophagy.* 1-12.
284. Quiros, P.M., Espanol, Y., Acin-Perez, R., Rodriguez, F., Barcena, C., Watanabe, K., Calvo, E., *et al.* (2014). ATP-dependent Lon protease controls tumor bioenergetics by reprogramming mitochondrial activity. *Cell Rep.* 8(2), 542-546.
285. Matsushima, Y., Goto, Y., and Kaguni, L.S. (2010). Mitochondrial Lon protease regulates mitochondrial DNA copy number and transcription by selective degradation of mitochondrial transcription factor A (TFAM). *Proc Natl Acad Sci U S A.* 107(43), 18410-18415.
286. Ngo, J.K., Pomatto, L.C.D., Bota, D.A., Koop, A.L., and Davies, K.J.A. (2011). Impairment of lon-induced protection against the accumulation of oxidized proteins in senescent wi-38 fibroblasts. *J Gerontol A Biol Sci Med Sci.* 66(11), 1178-1185.
287. Smakowska, E., Czarna, M., and Janska, H. (2014). Mitochondrial ATP-dependent proteases in protection against accumulation of carbonylated proteins. *Mitochondrion.* 19(B), 245-251.
288. Kuo, C., Chiu, Y., Lee, A.Y., and Hwang, T. (2015). Mitochondrial Lon protease controls ROS-dependent apoptosis in cardiomyocyte under hypoxia. *Mitochondrion.* 23: 7-16.
289. Venkatesh, S., Li, M., Saito, T., Tong, M., Rashed, E., Mareedu, S., Zhai, P., *et al.* (2019). Mitochondrial LonP1 protects cardiomyocytes from ischemia/reperfusion injury in vivo. *J Mol Cell Cardiol.* 128, 38-50.

290. Sun, C., Van Gilst, M., and Crowder, M.C. (2023). Hypoxia-induced mitochondrial stress granules. *Cell Death Dis.* 14(7), 448.
291. Sekine, Y., Houston, R., Eckl, E., Fessler, E., Narendra, D.P., Jae, L.T., and Sekine, S. (2023). A mitochondrial iron-responsive pathway regulated by DELE1. *Mol Cell.* 83(12), 2059-2076.
292. Rendon, O.Z., and Shoubridge, E.A. (2018). LONP1 is required for maturation of a subset of mitochondrial proteins, and its loss elicits an integrated stress response. *Mol Cell Biol.* 38(2), e00412-e00417.
293. Hong, X., Isern, J., Campanario, S., Perdiguero, E., Ramirez-Pardo, I., Segales, J., Hernansanz-Agustin, P., *et al.* (2022) Mitochondrial dynamics maintain muscle stem cell regenerative competence throughout adult life by regulating metabolism and mitophagy. *Cell Stem Cell.* 29(9), 1298-1314.
294. Song, M., Franco, A., Fleischer, J.A., Zhang, L., Dorn II, G.W. (2017). Abrogating mitochondrial dynamics in mouse hearts accelerates mitochondrial senescence. *Cell Metab.* 26(6), 872-883.
295. Vongsfak, J., Pratchayasaskul, W., Apaijai, N., Vaniyapong, T., Chattipakorn, N., and Chattipakorn, S.C. (2021). The alterations in mitochondrial dynamics following cerebral ischemia/reperfusion injury. *Antioxidants (Basel).* 10(9), 1384.
296. Longo, F., Benedetti, S., Zambon, A.A., Sora, M.G.N., Di Resta, C., De Ritis, D., Quattrini, A., *et al.* (2020) Impaired turnover of hyperfused mitochondria in severe axonal neuropathy due to a novel DRP1 mutation. *Hum Mol Genet.* 29(2), 177-188.
297. Liou, Y., Personnaz, J., Jacobi, D., Knudsen, N.H., Chalom, M.M., Starost, K.A., Nnah, I.C., *et al.* (2022) Hepatic Fis1 regulates mitochondrial integrated stress response and improves metabolic homeostasis. *JCI Insight.* 7(4), e150041.
298. Rana, A., Oliveira, M.P., Khamoui, A.V., Aparicio, R., Rera, M., Rossiter, H.B., and Walker, D.W. (2017). Promoting Drp1-mediated mitochondrial fission in midlife prolongs healthy lifespan of Drosophila melanogaster. *Nat Commun.* 8(1), 448.
299. Gumeni, S., Evangelakou, Z., Tsakiri, E.N., Scorrano, L., and Trougakos, I.P. (2019). Functional wiring of proteostatic and mitostatic modules ensures transient organismal survival during imbalanced mitochondrial dynamics. *Redox Biol.* 24, 101219.
300. Frezza, C., Cipolat, S., de Brito, O.M., Micaroni, M., Beznoussenko, G.V., Rudka, T., *et al*. (2006). OPA1 controls apoptotic cristae remodeling independently from mitochondrial fusion. *Cell*. 126(1), 177-189.
301. Pernas, L., and Scorrano, L. (2016). Mito-Morphosis: Mitochondrial fusion, fission, and cristae remodeling as key mediators of cellular function. *Annu Rev Physiol*. 78, 505-531.
302. Cartes-Saavedra, B., Macuada, J., Lagos, D., Arancibia, D., Andres, M.E., Yu-Wai-Man, P., *et al*. (2022). OPA1 modulates mitochondrial Ca2+ uptake through ER-mitochondria coupling. *Front Cell Dev Biol.* 9, 774108.
303. Herkenne, S., Ek, O., Zamberlan, M., Pellattiero, A., Chergova, M., Chivite, I., *et al*. (2020). Developmental and tumor angiogenesis requires the mitochondria-shaping protein Opa1. *Cell Metab*. 31(5), 987-1003.
304. Baker, N., Wade, S., Triolo, M., Girgis, J., Chwastek, D., Larrigan, S., *et al*. (2022). The mitochondrial protein OPA1 regulates the quiescent state of adult muscle stem cells. *Cell Stem Cell.* 299(9), 1315-1332.

305. Buck, M.D., O'Sullivan, D., Geltink, R.I.K., Curtis, J.D., Chang, C., Sanin, D.E., *et al*. (2016). Mitochondrial dynamics controls T cell fate through metabolic programming. *Cell*. 166(1), 63-76.
306. Wai, T., Garcia-Prieto, J., Baker, M.J., Merkwirth, C., Benit, P., Rustin, P., *et al*. (2015). Imbalanced OPA1 processing and mitochondrial fragmentation cause heart failure in mice. *Science*. 350(6265), aad0116.
307. Del Dotto, Mishra, P., Vidoni, S., Fogazza, M., Maresca, A., Caporali, L., *et al*. (2017). OPA1 isoforms in the hierarchical organization of mitochondrial functions. *Cell Rep*. 19(12), 2557-2571.
308. Anand, R., Wai, T., Baker, M.J., Kladt, N., Schauss, A.C., Rugarli, E., *et al*. (2014). The i-AAA protease YME1L and OMA1 cleave OPA1 to balance mitochondrial fusion and fission. *J Cell Biol*. 204(6), 919-929.
309. Zhang, K., Li, H., and Song, Z. (2014). Membrane depolarization activates the mitochondrial protease OMA1 by stimulating self-cleavage. *EMBO Rep*. 15(5), 576-585.
310. Head, B., Griparic, L., Amiri, M., Gandre-Babbe, S., and van der Bliek, A.M. (2009). Inducible proteolytic inactivation of OPA1 mediated by the OMA1 protease in mammalian cells. *J Cell Biol*. 187(7), 959-966.
311. Rainbolt, T.K., Lebeau, J., Puchades, C., and Wiseman, R.L. (2016). Reciprocal Degradation of YME1L and OMA1 adapts mitochondrial proteolytic activity during stress. *Cell Rep*. 14(9), 2041-2049.
312. Sekine, S., Wang, C., Sideris, D.P., Bunker, E., Zhang, Z., and Youle, R.J. (2019). Reciprocal roles of Tom7 and OMA1 during mitochondrial import and activation of PINK1. *Mol Cell*. 73(5), 1028-1043.
313. Ahola, S., Mejias, P.R., Hermans, S., Chandragiri, S., Giavalisco, P., Nolte, H., *et al*. (2022). OMA1-mediated integrated stress response protects against ferroptosis in mitochondrial cardiomyopathy. *Cell Metab*. 34(11), 1875-1891.
314. Baker, M.J., Lampe, P.A., Stojanovski, D., Korwitz, A., Anand, R., Tatsuta, T., *et al*. (20140. Stress-induced OMA1 activation and autocatalytic turnover regulate OPA1-dependent mitochondrial dynamics. *EMBO J*. 33(6), 578-593.
315. Garcia, I., Innis-Whitehouse, W., Lopez, A., Keniry, M., and Gilkerson, R. (2018). Oxidative insults disrupt OPA1-mediated mitochondrial dynamics in cultured mammalian cells. *Redox Rep*. 23(1), 160-167.
316. Jiang, X., Jiang, H., Shen, Z., and Wang, X. (2014). Activation of mitochondrial protease OMA1 by Bax and Bak promotes cytochrome c release during apoptosis. *Proc Natl Acad Sci U S A*. 111(41), 14782-14787.
317. Sanderson, T.H., Raghunayakula, S., and Kumar, R. (2015). Neuronal hypoxia disrupts mitochondrial fusion. *Neuroscience*. 301, 71-78.
318. Nan, J., Nan, C., Ye, J., Qian, L., Geng, Y., Xing, D., *et al*. (2019). EGCG protects cardiomyocytes against hypoxia-reperfusion injury through inhibition of OMA1 activation. *J Cell Sci*. 132(2), jcs220871.
319. Horwitz, E.R., Higgins, T.M., and Harvey, B.J. (1996). Histamine-induced cytosolic calcium increase in porcine articular chondrocytes. *Biochim Biophys Acta*. 1313(2), 95-100.
320. Liao, Y., Hao, Y., Chen, H., He, Q., Yuan, Z., and Cheng, J. (2015). Mitochondrial calcium uniporter protein MCU is involved in oxidative stress-induced cell death. *Protein Cell*. 6(6), 434-442.

321. Jouaville, L.S., Pinton, P., Bastianutto, C., Rutter, G.A., Rizzuto, R. (1999). Regulation of mitochondrial ATP synthesis by calcium: Evidence for a long-term metabolic priming. *Proc Natl Acad Sci U S A.* 96(24), 13807-13812.
322. Gerencser, A.A., Chinopoulos, C., Birket, M.J., Jastroch, M., Vitelli, C., Nicholls, D.G., *et al.* (2012). Quantitative measurement of mitochondrial membrane potential in cultured cells: calcium-induced de- and hyperpolarization of neuronal mitochondria. *J Physiol*. 590(12), 2845-2871.
323. Tondera, D., Grandemange, S., Jourdain, A., Karbowski, M., Mattenberger, Y., Herzig, S., *et al.* (2009). SLP-2 is required for stress-induced mitochondrial hyperfusion. *EMBO J*. 28(11), 1589-1600.
324. Reichert, S.A., Kim-Han, J.S., and Dugan, L.L. (2001). The mitochondrial permeability transition pore and nitric oxide synthase mediate early mitochondrial depolarization in astrocytes during oxygen-glucose deprivation. *J Neurosci.* 21(17), 6608-6616.
325. Solhjoo, S., Liu, T., Sidor, A., Lee, D.I., O'Rourke, B., and Steenbergen, C. (2023). Oxidative stress in the mitochondrial matrix underlies ischemia/reperfusion-induced mitochondrial instability. *J Biol Chem*. 299(1), 102780.
326. Lai, Y., Lin, P., Chen, M., Zhang, Y., Chen, J., Zheng, M., *et al*. (2020). Restoration of L-OPA1 alleviates acute ischemic stroke injury in rats via inhibiting neuronal apoptosis and preserving mitochondrial function. *Redox Biol*. 34, 101503.
327. Wappler, E.A., Institoris, A., Dutta, S., Katakam, P.V.G., and Busija, D.W. (2013). Mitochondrial dynamics associated with oxygen-glucose deprivation in rat primary neuronal cultures. *PLoS One*. 8(5), e63206.
328. Wu, Z., Zuo, M., Zeng, L., Cui, K., Liu, B., Yan, C., *et al*. (2021). OMA1 reprograms metabolism under hypoxia to promote colorectal cancer development. *EMBO Rep*. 22(1), e50827.
329. Sanderson, T.H., Raghunayakula, S., and Kumar, R. (2015). Release of mitochondrial Opa1 following oxidative stress in HT22 cells. *Mol Cell Neurosci*. 64, 116-122.
330. Bohovych, I., Dietz, J.V., Swenson, S., Zahayko, N., and Khalimonchuk, O. (2019). Redox regulation of the mitochondrial quality control protease Oma1. *Antioxid Redox Signal.* 31(6), 429-443.
331. Bohovych, I., Donaldson, G., Christianson, S., Zahayko, N., and Khalimonchuk, O. (2014). Stress-triggered activation of the metalloprotease Oma1 involves its C-terminal region and is important for mitochondrial stress protection in yeast. *J Biol Chem*. 289(19), 13259-13272.
332. Acin-Perez, R., Lechuga-Vieco, A.V., Del Mar Munoz, M., Nieto-Arellano, R., Torroja, C., Sanchez-Cabo, F., *et al.* (2018). Ablation of the stress protease OMA1 protects against heart failure in mice. *Sci Transl Med*. 10(434), eaan4935.
333. Korwitz, A., Merkwirth, C., Richter-Dennerlein, R., Troder, S.E., Sprenger, H., Quiros, P.M., *et al*. (2016). Loss of OMA1 delays neurodegeneration by preventing stress-induced OPA1 processing in mitochondria. *J Cell Biol*. 212(2), 157-166.
334. Franchino, C.A., Brughera, M., Baderna, V., De Ritis, D., Rocco, A., Seneca, S., *et al.* (2023). Sustained OMA1-mediated integrated stress response is beneficial for spastic ataxia type 5. *Brain*. awad340, https://doi.org/10.1093/brain/awad340

335. Shammas, M.K., Huang, X., Wu, B.P., Fessler, E., Song, I.Y., Randolph, N.P., *et al*. (2022). OMA1 mediates local and global stress responses against protein misfolding in CHCHD10 mitochondrial myopathy. *J Clin Invest.* 132(14), e157504.
336. Miller, R., Ewy, W., Corrigan, B.W., Ouellet, D., Hermann, D., Kowalski, K.G., Lockwood, P., *et al.* (2005). How modeling and simulation have enhanced decision making in new drug development. *J Pharmacokinet Pharmacodyn*. 32(2), 185-197.
337. Gal, J., Milano, G., Ferrero, J-M., Saada-Bouzid, E., Viotti, J., Chabaud, S., Gougis, P., *et al.* (2018). Optimizing drug development in oncology by clinical trial simulation: Why and how? *Brief Bioinform.* 19(6), 1203-1217.
338. Luraghi, G., Cahalane, R.M.E., van de Ven, E., Overschie, S.C.M., Gijsen, F.J.H., and Akyildiz, A.C. (2021). In vitro and in silico modeling of endovascular stroke treatments for acute ischemic stroke. *J Biomech*. 127, 110693.
339. Cortassa, S., and Aon, M.A. (2012). Computational modeling of mitochondrial function. *Methods Mol Biol*. 810, 311-326.
340. Cortassa, S., Sollott, S.J., and Aon, M.A. (2018). Computational modeling of mitochondrial function from a systems biology perspective. *Methods Mol Biol*. 1782, 249-265.
341. Tewai, S.G., Dash, R.K., Beard, D.A., and Bazil, J.N. (2012). A biophysical model of the mitochondrial ATP-Mg/P(i) carrier. *Biophys J*. 103(7), 1616-1625.
342. Kleessen, S., Aruajo, W.L., Fernie, A.R., and Nikoloski, Z. (2012). Model-based confirmation of alternative substrates of mitochondrial electron transport chain. *J Biol Chem*. 287(14), 11122-11131.
343. Senneff, S., and Lowery, M.M. (2022). Computational model of the effect of mitochondrial dysfunction on excitation-contraction coupling in skeletal muscle. *Bull Math Biol*. 84(11), 123.
344. Kowald, A. and Klipp, E. (2014). Mathematical models of mitochondrial aging and dynamics. *Prog Mol Biol Transl Sci*. 127, 63-92.
345. Zamponi, N., Zamponi, E., Cannas, S.A., Billoni, O.V., Helguera, P.R., and Chialvo, D.R. (2018). Mitochondrial network complexity emerges from fission/fusion dynamics. *Sci Rep*. 8(1), 363.
346. Hoffmann, T.E., Barnett, K.J., Wallis, L., Hanneman, W.H. (2017). A multimethod computational simulation approach for investigating mitochondrial dynamics and dysfunction in degenerative aging. *Aging Cell*. 16(6), 1244-1255.
347. Sukhorukov, V.M., Dikov, D., Reichert, A.S.,and Meyer-Hermann, M. (2012). Emergence of the mitochondrial reticulum from fission and fusion dynamics. *PLoS Comput Biol*. 8(10), e1002745.
348. Mouli, P.K., Twig, G., and Shirhai, O.S. (2009). Frequency and selectivity of mitochondrial fusion are key to its quality maintenance function. *Biophys J*. 96(9), 3509-3518.
349. Soheilypour, M., and Mofrad, M.R.K. (2018). Agent-based modeling in molecular systems biology. *Bioessays*. 40(7), e1800020.
350. Figge, M.T.,. Reichert, A.S., Meyer-Hermann, M., and Osiewacz, H.D. (2012). Deceleration of fusion–fission cycles improves mitochondrial quality control during aging. *PLoS Comput Biol*. 8(6), e1002576.

351. Dalmasso, G., Zapata, P.A.M., Brady, N.R., and Hamacher-Brady, A. (2017). Agent-based modeling of mitochondria links sub-cellular dynamics to cellular homeostasis and heterogeneity. *PLoS One*. 12(1), e0168198.
352. Zorova, L.D., Popkov, V.A., Plotnikov, E.Y., Silachev, D.N., Pevzner, I.B., Jankauskas, S.S., Babenko, V.A., *et al.* (2018). Mitochondrial membrane potential. *Anal Biochem*. 552, 50-59.
353. Teodoro, J.S., Palmeira, C.M., and Rolo, A.P. (2018). Mitochondrial membrane potential (ΔΨ) fluctuations associated with the metabolic states of mitochondria. *Methods Mol Biol*. 1782, 10-119.
354. Xiao, B.,Deng, X., and Tan, E. (2016). Flow cytometry-based assessment of mitophagy using MitoTracker. *Front Cell Neurosci*. 10, 76.
355. Greene, A.W., Grenier, K., Aguileta, M.A., Muise, S., Farazifard, R., Haque, M.E., McBride, H.M., *et al.* (2012). Mitochondrial processing peptidase regulates PINK1 processing, import and Parkin recruitment. *EMBO Rep*. 13(4), 378-385.
356. Muster, B., Kohl, W., Wittig, I., Strecker, V., Joos, F., Haase, W., Bereiter-Hahn, J., *et al.* (2010). Respiratory chain complexes in dynamic mitochondria display a patchy distribution in life cells. *PLoS One*. 5(7), e11910.
357. Ali, S., and McStay, G.P. (2018). Regulation of mitochondrial dynamics by proteolytic processing and protein turnover. *Antioxidants (Basel)*. 7(1), 15.
358. Dewachter, I., Reverse, D., Caluwaerts, N., Ris, L., Kuiperi, C., Van den Haute, C., Spittaels, K., *et al.* (2002). Neuronal deficiency of presenilin 1 inhibits amyloid plaque formation and corrects hippocampal long-term potentiation but not a cognitive defect of amyloid precursor protein [V717I] transgenic mice. *J Neurosci*. 22(9), 3445-3453.
359. Wilensky, U. NetLogo. http://ccl.northwestern.edu/netlogo/. Center for Connected Learning and Computer-Based Modeling, Northwestern University, Evanston, IL (1999)
360. Kurz, F.T., Aon, M.A., Schlemmer, H-P., Jende, J.M.E., O'Rourke, B., and Armoundas, A.A. (2023). Fractal dynamics of individual mitochondrial oscillators measure local inter-mitochondrial coupling. *Biophys J*. 122(8), 1459-1469.
361. Kuznetsov, A.V., Javadov, S., Saks, V., Margreiter, R., and Grimm, M. (2017). Synchronism in mitochondrial ROS flashes, membrane depolarization and calcium sparks in human carcinoma cells. *Biochim Biophys Acta Bioenerg*. 1858(6), 418-431.
362. Wolf, D.M., Segawa, M., Kondadi, A.K., Anand, R., Bailey, S.T., Reichert, A.S., van der Bliek, A.M., *et al.* (2019). Individual cristae within the same mitochondrion display different membrane potentials and are functionally independent. *EMBO J*. 38(22), e101056.
363. Sato, T.K., Kawano, S., and Endo, T. (2019). Role of the membrane potential in mitochondrial protein unfolding and import. *Sci Rep*. 9(1), 7637.
364. Chen, S-D., Yang, D-I., Lin, T-K., Shaw, F-Z., Liou, C-W., and Chuang, Y-C. (2011). Roles of oxidative stress, apoptosis, PGC-1α and mitochondrial biogenesis in cerebral ischemia. *Int J Mol Sci*. 12(10), 7199-7215.
365. Iijima, T., Mishima, T., Tohyama, M., Akagawa, K., and Iwao, Y. (2003). Mitochondrial membrane potential and intracellular ATP content after transient experimental ischemia in the cultured hippocampal neuron. *Neurochem Int*. 43(3), 263-269.

366. Brookes, P.S., Yoon, Y., Robotham, J.L., Anders, M.W., and Sheu, S. (2004). Calcium, ATP, and ROS: a mitochondrial love-hate triangle. *Am J Physiol Cell Physiol*. 287(4), C817-C833.
367. Chatterjee, S., Browning, E.A., Hong, N., DeBolt, K., Sorokina, E.M., Liu, W., Birnbaum, M.J., *et al.* (2012). Membrane depolarization is the trigger for PI3K/Akt activation and leads to the generation of ROS. *Am J Physiol Heart Circ Physiol*. 302(1), H105-H114.
368. Starkov, A.A., and Fiskum, G. (2003). Regulation of brain mitochondrial H2O2 production by membrane potential and NAD(P)H redox state. *J Neurochem*. 86(5), 1101-1107.
369. Margaill, I., Plotkine, M., and Lerouet, D. (2005). Antioxidant strategies in the treatment of stroke. *Free Radic Biol Med*. 39(4), 429-443.
370. Ibrahim, A.A., Mageed, S.S.A., Safar, M.M., El-Yamany, M.F., and Oraby, M.A. (2023). MitoQ alleviates hippocampal damage after cerebral ischemia: The potential role of SIRT6 in regulating mitochondrial dysfunction and neuroinflammation. *Life Sci.* 328, 121895.
371. Hobbs, C.E., Murphy, M.P., Smith, R.A.J., and Oorschot, D.E. (2008). Neonatal rat hypoxia-ischemia: Effect of the anti-oxidant mitoquinol, and S-PBN. *Pediatr Int*. 50(4), 481-488.
372. Komakula, S., Bhatia, R., Sahib, A., Upadhyay, A., S, L.J., Garg, A., Y. V.V., *et al.* (2024). Safety and efficacy of N-acetylcysteine (NAC) as an adjunct to standard treatment in patients with acute ischemic stroke: a randomized controlled pilot trial (NACTLYS). *Sci Rep*. 14(1), 1103.
373. Mao, R., Zong, N., Hu, Y., Chen, Y., and Xu, Y. (2022). Neuronal death mechanisms and therapeutic strategy in ischemic stroke. *Neurosci Bull*. 38(10), 1229-1247.
374. Sohrabji, F., Selvamani, A., and Balden, R. (2013). Revisiting the timing hypothesis: biomarkers that define the therapeutic window of estrogen for stroke. *Horm Behav*. 63(2), 222-230.
375. Waller, J., Kaur, P., Tucker, A., Amer, R., Bae, S., Kogler, A., and Umair, M. (2021). The benefit of intravenous thrombolysis prior to mechanical thrombectomy within the therapeutic window for acute ischemic stroke. *Clin Imaging*. 79, 3-7.
376. Lu, S., Zhang, J., Wu, R., Cao, Y., Xu, X., Li, G., Liu, S., *et al.* (2022). Use of machine learning algorithms to predict the outcomes of mechanical thrombectomy in acute ischemic stroke patients with an extended therapeutic time window. *J Comput Assist Tomogr*. 46(5), 775-780.
377. Chang, X., Niu, S., Shang, M., Li, J., Guo, M., Zhang, W., Sun, Z., *et al.* (2023). ROS-Drp1-mediated mitochondria fission contributes to hippocampal HT22 cell apoptosis induced by silver nanoparticles. *Redox Biol*. 63, 102739.
378. Cid-Castro, C., andMoran, J. (2021). Differential ROS-mediated phosphorylation of Drp1 in mitochondrial fragmentation induced by distinct cell death conditions in cerebellar granule neurons. *Oxid Med Cell Longev*. 2021, 8832863.
379. Iqbal, S., andHood, D.A. (2014). Oxidative stress-induced mitochondrial fragmentation and movement in skeletal muscle myoblasts. *Am J Physiol Cell Physiol*. 306, C1176-C1183.

380. Krzystek, T.J., Banerjee, R., Thurston, L., Huang, J., Swinter, K., Rahman, S.N., Falzone, T.L., *et al.* (2021). Differential mitochondrial roles for α-synuclein in DRP1-dependent fission and PINK1/Parkin-mediated oxidation. *Cell Death Dis*. 12, 796.
381. Katajisto, P., Dohla, J., Chaffer, C.L., Pentinmikko, N., Marjanovic, N., Iqbal, S., Zoncu, R., *et al.* (2015). Asymmetric apportioning of aged mitochondria between daughter cells is required for stemness. *Science*. 348(6232), 340-343.
382. Joshi, D.C., and Bakowska, J.C. (2021). Determination of mitochondrial membrane potential and reactive oxygen species in live rat cortical neurons. *J Vis. Exp*. 51, 2704.
383. Cereghetti, G.M., Costa, V., and Scorrano, L. (2010). Inhibition of Drp1-dependent mitochondrial fragmentation and apoptosis by a polypeptide antagonist of calcineurin. *Cell Death Differ*. 17(11), 1785-1794.
384. De Vos, K.J., Allan, V.J., Grierson, A.J., and Sheetz, M.P. (2005). Mitochondrial function and actin regulate dynamin-related protein 1-dependent mitochondrial fission. *Curr Biol*. 15(7), 678-683.
385. Vanden Hoek, T.L., Li, C., Shao, Z., Schumacker, P.T., and Becker, L.B. (1997). Significant levels of oxidants are generated by isolated cardiomyocytes during ischemia prior to reperfusion. *J Mol Cell Cardiol*. 29(9), 2571-2583.
386. Peters, O., Back, T., Lindauer, U., Busch, C., Megow, D., Dreier, J., and Dirnagl, U. (1998). Increased formation of reactive oxygen species after permanent and reversible middle cerebral artery occlusion in the rat. *J Cereb Blood Flow Metab*. 18(2), 196-205.